The Dissertation Committee for Eric Ivan Petersen Certifies that this is the approved version of the following Dissertation:

The Ice Content and Internal Structure of Candidate Debris-Covered Glaciers on Mars and Earth: Insights from Radar Sounding

Committee:

John W. Holt, Supervisor

Joseph S. Levy, Co-Supervisor

Ginny Catania

Cyril Grima

David Mohrig

The Ice Content and Internal Structure of Candidate Debris-Covered Glaciers on Mars and Earth: Insights from Radar Sounding

by

Eric Ivan Petersen

Dissertation

Presented to the Faculty of the Graduate School of

The University of Texas at Austin

in Partial Fulfillment

of the Requirements

for the Degree of

Doctor of Philosophy

The University of Texas at Austin

August 2018

Acknowledgements

This dissertation work was made possible by the NASA Earth and Space Science Fellowship (NESSF) awarded to the Author. Fieldwork at Galena Creek Rock Glacier was made possible by a Jackson School Seed Grant awarded to Cassie Stuurman. I would like to thank Stefano Nerozzi, Dan Lalich, and Cassie Stuurman for technical help, productive and amusing office conversations, and for being excellent fieldwork partners. I thank Philip Petersen and Janice Peltier, my father and mother, for instilling in me the dedication to see this dissertation through. I thank Rebecca Tarvin for her support and Manchego for being my late night writing buddy. I thank Ben Cardenas for his field assistance and friendship. I would like to thank the Planetary Geophysics Field Classes of 2013 and 2015, including Dan Aylward, Jim Pharr, Parvathy Prem, William Hoey, YeJin Lim, Logan Schmidt, Jackie Rambo, Kian Maharaj, Tina Andry, Lizzy McKinnon, and others aforementioned. This class was my first experience with the Mars Research Group as well as field geology; it set me on the road to the completion of this PhD and helped produce some of the data used in my research. I would like to thank Jeff Paine for the loan of his TerraTEM system for several rock glacier field excursions. The SHARAD instrument was provided to NASA's MRO mission by the Italian Space Agency (ASI), and its operations are led by the DIET Department, University of Rome ''La Sapienza'' under an ASI contract.

Abstract

The Ice Content and Internal Structure of Candidate Debris-Covered Glaciers on Mars and Earth: Insights from Radar Sounding

Eric Ivan Petersen, PhD

The University of Texas at Austin, 2018

Supervisor: John W. Holt

Co-Supervisor: Joseph S. Levy

Martian lobate debris aprons are enigmatic mid-latitude landforms known to contain a significant fraction of water ice preserved at depth beneath a surface debris layer. They are thought to be important records of climate history and potential water resources for manned missions to Mars. However, their internal structure remains poorly constrained and regional variability in their ice purity is unknown. In this dissertation we report on a regional orbital radar sounding survey of lobate debris aprons in Deuteronilus Mensae – the region of highest concentration of lobate debris aprons on Mars – to constrain trends in lobate debris apron composition and possible internal structure. We also present a geophysical survey of Galena Creek Rock Glacier to constrain its internal structure as an analog to Martian lobate debris aprons.

We found that the majority of radar observations imaged a basal reflector, from which we determined that the apron body is composed of material with dielectric properties consistent with relatively pure water ice and that there is no evidence for region-wide variability. Combining our compositional results with apron volumes constrained by Levy et al. (2014) sets the regional ice budget at 0.9-1.0 x 10^5 km^3, the equivalent of roughly 4x the combined volume of water in the Great Lakes. We additionally showed that non-detection of basal reflectors in 13% of the observations may be attributed to high apron thickness and surface roughness-induced signal loss.

In our analog work on Galena Creek Rock Glacier, we imaged its internal structure consisting of a network of englacial debris layers. This internal structure is indicative of intermittent debris and ice accumulation, with debris fall potentially playing a role in enhancing and facilitating ice accumulation. Similar englacial debris layers may exist in Martian lobate debris aprons, but are not imaged by the available orbital radar dataset due to their dip and thickness.

Table of Contents

List of Tables

List of Figures

Chapter 1: Introduction

The "Candidate Debris Covered Glaciers" that this dissertation explores are landforms on Mars and Earth termed lobate debris aprons and rock glaciers, respectively. Both Martian lobate debris aprons and terrestrial rock glaciers were initially thought to be composed primarily of rocky debris, with interstitial ice on the order of tens of percent by volume filling pore space and facilitating flow (Capps, 1910; Squyres, 1978). The primary source for ice in these features was thought to be periglacial, from ground ice sapping (Lucchitta, 1984) or refreezing of snow melt and rainwater (Wahrhaftig & Cox, 1959). At the present day it is widely accepted that many lobate debris aprons (Holt et al., 2008; Plaut et al., 2009) and rock glaciers (Potter Jr et al., 1998) are composed in bulk of water ice sourced from atmospheric accumulation during periods of glaciation, preserved by an ablation-reducing surface debris layer (Östrem, 1959).

These true debris-covered glaciers are of interest for two reasons. They may preserve detailed climate history in their internal structure (Mackay et al., 2014; Mackay & Marchant, 2017), and they can provide large reservoirs of fresh water both for alpine watersheds (Rangecroft et al., 2015) and for potential manned missions to Mars (Gallegos & Newsom, 2015; Head et al., 2015; Plaut, 2015).

Water ice is not currently stable at the near-subsurface in the Martian mid-latitudes where lobate debris aprons are found (Mellon & Jakosky, 1993). At higher orbital spin-axis obliquity, however, ice is not only stable (Mellon & Jakosky, 1995) but has been predicted by general circulation modeling to have migrated to the mid-latitudes (Forget et al., 2006; Madeleine et al., 2009). Mars' orbital parameters are chaotic, however, and it is difficult to provide a solution for them past ~ 20 Ma (Laskar et al., 2004; Laskar et al., 2002). Lobate debris aprons are thought to be hundreds of millions of years old (Mangold, 2003), and thus may record climate history and infer orbital parameters on such timescales. Many questions remain however about the properties of lobate debris aprons and what they tell us about the processes that formed them.

One open question about Martian lobate debris aprons is the total volume of water ice that they contain. While several lobate debris aprons have been confirmed by radar sounding to be composed in bulk of >80% purity water ice (Holt et al., 2008; Plaut et al., 2009), it is not yet known if that is representative of all lobate debris aprons. Levy et al. (2014) mapped the total global volume of lobate debris aprons, constraining their water ice content to between 1.25×10^5 km^3 (assuming 30% ice content) and 3.74×10^5 km^3 (assuming 90% ice content), producing an uncertainty of a factor of 3.

If there is any variability in the ice content of lobate debris aprons, it is also important to understand the regional distribution of that variability. Ice poor aprons may represent a region which in the past experienced less ice accumulation and more dust or debris accumulation—an important constraint for climate modelers seeking to unravel the planet's dust and water ice cycles over orbital timescales. It is also important to potential manned missions that they land in a location with a proven water source.

It is also an open question whether these features were deposited in a single glaciation (accumulation event) or whether they are the result of a series of glacial events. If they were produced in a series of glacial events it is likely that this is preserved in their internal structure. An analog example is the Mullins debris-covered glacier, which has been shown to contain englacial debris layers that may represent local periods of low accumulation driven by orbital obliquity cycles (Mackay et al., 2014; Mackay & Marchant, 2017). Such a climate record is the holy grail of the study of lobate debris aprons, providing valuable information for climate modelers and geologists. It is thus imperative to constrain the internal structure of lobate debris aprons as well as analog features such as rock glaciers.

The purpose of this dissertation is to advance our understanding of lobate debris aprons by assessing compositional variability on the regional scale and constraining their internal structure. To achieve this goal, we present a regional survey of lobate debris aprons and inform that work with analog geophysical work on Galena Creek Rock Glacier. Specifically, we seek to answer the following questions: (1) is there any variability in the internal composition of martian lobate debris aprons, (2) are we able to observe any internal structure in martian aprons, (3) can we observe at any location the base of the surface debris layer for martian aprons, (4) are there any martian aprons for which radar can't image the interior, and if so, why not, (5) what is the internal structure of Galena Creek Rock Glacier, (6) what produced the internal structure at Galena Creek Rock Glacier, and (7) how does the internal structure of Galena Creek Rock Glacier inform us about lobate debris aprons.

The keystone dataset in these studies is ground-penetrating radar (GPR) at various frequencies. Orbital radar sounding data is provided for the Martian targets by the Shallow Radar sounder (SHARAD) onboard Mars Reconnaissance Orbiter (MRO), which orbits Mars in a polar orbit at an average height above the surface of ~300 km. SHARAD is a chirped radar sounder operating at a center frequency of 20 MHz with a 10 MHz bandwidth, resulting in a free-space resolution of ~15 m (Seu et al., 2007). We used the ground-based single-frequency PulseEKKO Pro GPR system for our terrestrial study, with radio frequencies of 100 MHz and 50 MHz corresponding to 3 m and 6 m wavelengths in free space, respectively. These radars are very different beasts and as such we are not using the ground-based GPR system as a direct equipment analog for SHARAD, but only as a similar method to image the interior of analog landforms.

This dissertation is split into two parts: the first describing an orbital radar sounding survey of lobate debris aprons using SHARAD data and the second describing a ground-based geophysical survey of Galena Creek Rock Glacier. The first part is split into two chapters, the first describing the analysis of lobate debris aprons for which the interior is imaged by SHARAD and the second describing the analysis of lobate debris aprons for which the interior is not imaged by SHARAD.

Chapter 2: Literature Review of Candidate Debris-Covered Glaciers

A cursory glance of the scientific literature for lobate debris aprons and rock glaciers shows that they have taken parallel paths, and for good reason: rock glaciers are often referred to as analogs for lobate debris aprons (Lucchitta, 1984; Squyres, 1978). We argue there are two key facts from the rock glacier literature that must be applied to our understanding of lobate debris aprons. First, there is significant variability in the composition of terrestrial rock glaciers; i.e. there are ice-cored rock glaciers which are essentially debris-covered glaciers (Potter, 1972) as well as rock glaciers that are composed primarily of debris with interstitial ice (Bucki et al., 2004; Degenhardt, 2003). Second, the internal structure of rock glaciers (the distribution of ice and debris) can be quite complicated and may reveal accumulation and flow history (Brown, 1925; Bucki et al., 2004; Florentine et al., 2014; Monnier & Kinnard, 2015). In this chapter we first present a literature review of rock glaciers and lobate debris aprons.

TERRESTRIAL ROCK GLACIERS

Although they were known to the Coloradan miners in the 1800s as "rock streams," rock glaciers were first given their current name and described scientifically by Capps (1910). Capps (1910) reported on observations of these enigmatic features in the Wrangell Mountains near McCarthy, Alaska, where he defined rock glaciers as features composed of angular talus inhabiting mountain valleys and exhibiting evidence for viscous flow similar to traditional clean ice glaciers. These geomorphic indicators of recent and active viscous flow include slope-parallel lineations along the length of the feature, slope-transverse ridges and furrows near the toe of the feature where compression may have occurred, troughs at the edges between the rock glacier and valley wall, a steep toe at the lower edge of the feature often at the angle of repose, and a surface bereft of vegetation with patches of lichen at variable stages of development. Capps (1910) made an additional observation of a specific rock glacier in McCarthy Creek that provided robust evidence in favor of recent flow: the rock glacier toe burying a stream which was unable to erode into the rock glacier toe at the same rate of its advancement. The talus present on rock glacier surfaces is composed of the same bedrock material found in the headwalls of the cirque. Capps (1910) noted that while many rock glaciers extend to the parent cirque without any ice exposed at the surface there were a few that gradated into clean ice glaciers up-valley. He also described interstitial ice found in the debris at depths of 1-2 feet in the upper sections of some rock glaciers. Although Capps (1910) was somewhat agnostic about the source of ice, he concluded that its distribution in the rock glaciers is interstitial and that it facilitated active viscous motion similar to that observed in clean ice glaciers.

Another early and sensational observation of rock glaciers was the opportunistic observation of the internal structure of a rock glacier in the Hurricane Basin, Colorado facilitated by a horizontal tunnel built by mining crews (Brown, 1925). This study observed a horizontal stratigraphy, starting at the rock glacier edge, of a "few" feet of angular debris followed by three hundred feet of ice-cemented debris and finally one hundred feet of clean ice before the tunnel hit bedrock. This study espoused the idea that the ice core found against bedrock represents glacial ice buried by a landslide to which preserved the ice and created "rock-stream" morphology.

One of the keystone studies that is almost ubiquitously cited by rock glacier papers is work published by Wahrhaftig & Cox (1959) on 200 rock glaciers in the Alaska Range. They morphologically distinguished between wide lobate rock glaciers at the base of cliffs, long tongue-shaped rock glaciers flowing down valleys, and spatulate rock glaciers resembling tongue-shaped rock glaciers with the addition of a spreading front. They also distinguished between active rock glaciers exhibiting sharp steep fronts at the angle of repose with little vegetation or lichen formed on them and inactive rock glaciers with gentle slopes and variable vegetation development. Similar to Capps (1910) they observed the rock glaciers to be composed of talus with interstitial ice at depth. They observed surface flow velocities of 1.6 – 2.4 ft/yr and viscosities similar to or up to 3 orders of magnitude higher than typical glacier ice viscosity. These observations led them to conclude that the velocity is produced as result of the bulk deformation of the rock glacier, similar to viscous creep of a clean glacier. They observed that rock glaciers in the range are typically found in an altitudinal range centered on the lower limit of clean glaciers, and that they are less sensitive to aspect. Wahrhaftig & Cox (1959) concluded that rock glaciers form in periglacial environments where headwall cliffs provide the source of debris in which water from snowmelt and rain is refrozen to accumulate interstitial ice.

The prevailing view that rock glaciers are formed exclusively of talus with interstitial ice was challenged most famously by an exhaustive study of Galena Creek Rock Glacier (Potter, 1972). This study used exposure observations and seismic profiling to show that the glacier in the upper two-thirds of the valley is cored by 88-90% purity sedimentary ice under a surface debris layer 1-1.5 m thick. Ice fabric analyses were also consistent with glacier ice. Based on observations of snowfield depth and debris fall, Potter (1972) hypothesized that the ice core is formed by accumulation of wind-blown snow in a narrow accumulation zone at the base of cirque headwalls. The ice is then preserved by debris fall coming to rest on the snow surface at the end of the accumulation zone, leaving little debris to be entrained in the glacier ice.

Potter's findings were then challenged in a reply by Barsch (1987), who used a handful of seismic observations on the lower section of Galena Creek along with other geomorphic observations to argue that the rock glacier was no different from any other in the literature and that there was no evidence to show that it contains a glacial ice core.

Potter Jr et al. (1998) rebuked that there was no evidence that Barsch had worked anywhere near the upper section of Galena Creek Rock Glacier and that he had ignored key evidence in favor of the glacigenic model. Potter set about revisiting his work on Galena Creek Rock Glacier, culminating in a 1998 rock glacier summit to address community-wide questions about rock glacier origins. (Ackert, Jr., 1998; Clark et al., 1998; Potter Jr et al., 1998; Steig, Clark, et al., 1998; Steig, Fitzpatrick, et al., 1998).

This resulted in new long-term measurements of Galena Creek Rock Glacier's surface velocity (Potter Jr et al., 1998), an ice core revealing 9.5 m of glacial ice from beneath the debris layer in the middle section of the glacier (Clark et al., 1996), a geomorphic model for how multiple episodes of glaciation produce the lobes and moraines observed (Ackert, Jr., 1998), and new ideas about the climate history that rock glaciers might record (Steig, Clark, et al., 1998).

Overall, the summit reaffirmed the overwhelming evidence in favor of the glacigenic origin of ice in ice-cored rock glaciers, while allowing that periglacial processes may still play some role (Clark et al., 1998).

MARTIAN LOBATE DEBRIS APRONS

Lobate debris aprons are a distinct class of Martian landform first identified in Viking orbiter images by Squyres (1978). Lobate debris aprons are, as the name suggests, aprons of what appear to be lithic debris found at the base of scarps, mesas, and valley walls. They extend up to 10s of km beyond their parent headwall and their surfaces exhibit morphologies including lobate margins and lineations that Squyres attributed to viscous flow and compression. Their thickness is typically on the order of several hundred meters. By analogy with the contemporary understanding of terrestrial rock glaciers, Squyres attributed this viscous flow to the creep of interstitial ice (~30% by volume) contained within the aprons.

Subsequent work found that the global distribution of lobate debris aprons is concentrated on latitudinal bands about 25° wide centered on 40° N and 45° S, suggesting a strong dependence on climatic regime and bolstering the hypothesis that atmospherically-derived water ice is involved (Squyres, 1979). They additionally tend to be found in highest abundance in areas of dramatic topographic relief such as the dichotomy boundary between the Noachian southern highlands and Amazonian northern lowlands, highlighting the importance of mass wasting in their formation. The regions of highest concentration of lobate debris aprons are Deuteronilus Mensae, Protonilus Mensae, Nylosyrtis Mensae, Tempe Terra, and Phlegra Montes in the Northern Hemisphere, and Eastern Hellas and Argyre Basin in the Southern Hemisphere (Levy et al., 2014; Squyres, 1979). Similar features are also found with concentric lineations in craters (concentric crater fill) and downslope lineations in valleys (lineated valley fill).

Deutoronilus Mensae contains by far the highest concentration of lobate debris aprons (Levy et al., 2014; Squyres, 1979). The name in Latin translates roughly as the "Deuteron Tables," similar to that of the neighboring region Protonilus Mensae, or the "Proton Tables." It is situated on the northern hemisphere along the dichotomy boundary between the ancient southern highlands and Amazonian-aged northern lowlands (Tanaka et al., 2014). The area is characterized by mesas (the tables so-named) and massifs that dot the smooth low-lying plains just north of the dichotomy boundary, as well as canyon structures such as Mamers Valles that disect the highlands and open into the lowlands.

Because of its chaotic, blocky appearance, the topography of Deuteronilus Mensae and other regions (including Protonilus Mensae and Nylosyrtis Mensae) has been described as “Fretted Terrain” (Sharp, 1973) and its origin the subject of some scientific scrutiny.

At least one study has drawn connections between the fretted terrain and lobate debris aprons, hypothesizing that ground ice contained beneath caprock in the mesas was permitted to ooze out at the edges, causing mesa erosion and viscous flow in debris aprons (Lucchitta, 1984). Lucchitta (1984) also compared the viscous flow morphology of lobate debris aprons to medial moraines and flowlines on Antarctic glaciers, but found the possiblity of high ice purity to be low based on her model of ice emplacement. This ground ice genesis for debris aprons stands in contrast to Squyres's model of atmospheric frost deposition into debris aprons. Other studies have attributed the formation of fretted terrain more generically to the removal of any subsurface material, including the possibility of magma (Sharp, 1973).

Since these initial studies, the literature concerning lobate debris aprons generally accrued increasing evidence in favor of ice contents significantly higher than the minimum interstitial ice of ~30% by volume suggested by Squyres (1978). Subsequent studies of their rheology (Colaprete & Jakosky, 1998; Fastook & Head, 2008; Karlsson et al., 2015; Li et al., 2005; Parsons et al., 2011), morphology (Head et al., 2006; Kress & Head, 2008), and relationship to Martian climate history (Forget et al., 2006; Madeleine et al., 2009) have suggested a higher component (as much as 80% or more) sourced from atmospheric accumulation during periods of mid-latitude glaciation. This charge was initially led by rheological work based on gross morphology/topography.

The rheology of ice-debris mixtures is not well-understood, but the general understanding is that as debris is mixed into ice in low concentrations its viscosity remains the same or softens slightly but when the debris concentration exceeds ~50% by volume the debris grains begin interacting and the mixture becomes more rigid (Moore, 2014). The most famous example of this is the observation of englacial silt bands exposed by tunnels carved into the Greenland Ice Sheet; bands with < 50% debris oozed out of the ice walls while band with > 50% debris remained rigid (Swinzow, 1962). The flow of clean ice is described well by The Glen-Nye flow law (Nye, 1957), more often referred to as Glen's flow law. Glen's flow law describes how the strain rate ε (deformation and subsequent motion of the ice) is related to stress τ (gravitational forces, glacier geometry) as follows:

$$\varepsilon = A\tau^{n} \tag{1}$$

Where the value A is strongly dependent on temperature and the exponent is somewhat dependent on stress but is typically n = 3 for terrestrial glacial conditions. Experiments by Goldsby & Kohlstedt (2001) corroborated by the analysis of Parsons et al. (2011) later showed that n = 2 is more appropriate for the temperature and stress regimes experienced by ice in Martian lobate debris aprons.

Colaprete & Jakosky (1998) were the first to employ a time-marching flow model to lobate debris aprons using Glen's flow law. They prescribed a modified exponent n = 3 - d, where d is the debris concentration, to capture increased rigidity with increased debris. They found that debris concentrations greater than 30% required flow timescales under martian conditions of greater than 10 million years. They discounted these results as unlikely based on the assumption that timescales of orbital and climate change on the order of millions of years (Mellon & Jakosky, 1995) precludes their persistence for such a duration.

Colaprete & Jakosky were soon shown to be wrong in their assumption about the age of lobate debris aprons. Mangold (2003) used crater counting techniques to show that the surfaces of lobate debris aprons have been active for the past tens of millions of years and hypothesized that the debris aprons themselves are some hundreds of millions of years old.

More detailed geomorphic studies of lobate debris aprons were able to uncover evidence of multiple subsequent periods of formation, resulting in overlapping lobes of material (e.g. Head et al., 2006; Levy et al., 2007). Head et al. (2006) looked in detail at the morphology of an extensive valley-filled apron system in the northern midlatitudes. They found many smaller lobes originating in cirques with steep headwalls and sharp aretes typical of glacial erosion. These smaller lobes were observed at times joining with, and at times overlapping, the main valley trunk of the system. Where lobes entered the main trunk, deflection of flow lineations was used to map relative flow velocities and it was found that velocity increased down valley, also consistent with glacial flow.

Other geomorphic studies of viscous flow features hinted at higher water ice content. Kress and Head (2008) identified unique ring-mold impact crater morphologies on lobate debris apron and lineated valley fill surfaces as being indicative of massive water ice content in the subsurface. By looking at the size distribution of bowl crater and ring-mold crater morphologies, they suggested a simple model of an ice rich substrate covered by a debris layer of 10 m thickness. Mangold (2003) interpreted the pitted, irregular surface of aprons and valley fill as evidence for heterogeneous sublimation of surface ice dependent upon fractures and ice-pocket/debris matrix structure.

Studies of lobate debris apron topography compared to simple plastic and viscous flow models suggested that ice concentrations of greater than 40% by volume were needed to produce the convex topography seen (Li et al., 2005).

Despite evidence for water ice in lobate debris aprons, present climatic conditions at the mid-latitude regions where they are found are highly nonconducive to deposition and stability of water ice in the near-subsurface (Mellon and Jakosky, 1995). Presumably, there was some point in recent geological history when the climate was conducive to water ice accumulation and stability in the mid-latitudes.

The climate variable which makes this possible is Mars' chaotically varying spin-axis obliquity, which has been modeled as reaching higher than 45° in the past 10 million years (Touma and Wisdom, 1993). This is much more extreme than the present-day value of 25° (similar to Earth's) and leads to greater insolation at the poles as well as revised global weather patterns. Forget et al. (2006) used a General Circulation Model (GCM) to model the Martian climate at a high obliquity of 45°, using the polar ice caps as a water ice reservoir. They observed water ice precipitation to the point of ice sheet production in the southern mid-latitudes corresponding to the regions of high lobate debris apron concentration, as well as the production of ice sheets in the Tharsis Montes equatorial region. Interestingly, the only model which was able to produce the same results for the northern mid- latitude regions was a GCM which assumed a moderate obliquity of 35°, a water ice reservoir in the Tharsis Montes (analogous to the one produced in the previous experiment), and an elevated atmospheric dust content (Madeleine et al., 2009). These results suggest a structured cycling of water ice distribution at latitude as a function of chaotic obliquity variations and further suggest that the northern mid latitude viscous flow features postdate the southern mid latitude features. In addition, the heightened dust content accelerates accumulation and produces a changed ice rheology as a function of dust content. The ice accumulation involved was on the order of ~10-20 mm/year, leading to the accumulation of a 500-1000 m thick regional icesheet over the course of

~50,000 years (Madeleine et al., 2009). These values are consistent with lobate debris aprons forming over a single high obliquity cycle (Laskar et al., 2002).

Fastook et al. (2011) used the accumulation predicted by Madeleine et al. (2009)'s GCM as input to an integrated mass balance flow model for ice sheets in modeling a lineated valley fill system in the north mid latitudes. After the ice sheet was built up, he turned off the accumulation term and allowed the ice to deflate until the ice sheet topography roughly matched that seen at present day. The relative flow velocities then observed were seen to match with the qualitative observations made by Head et al. (2006) for the same valley fill complex. This study showed the promise of integrating climate studies and physical modeling with geomorphic observations in further constraining lobate debris apron properties and history. However, it is limited in that it doesn't take into account the effect of dust content on the rheology of the ice, nor the production of a debris cover via rock fall and/or lag deposit. Parsons et al. (2011) took into account the effect of dust content on rheology in his 2D flow model while not incorporating mass balance. Future studies may integrate all of these parameters.

As surface water ice is unstable in the Martian mid-latitudes at the present day (Mellon & Jakosky, 1993), it is the presence of the surface debris layer that facilitates the preservation of lobate debris apron ice by insulating it against seasonal atmospheric temperature swings (Evatt et al., 2015; Helbert, 2005; Östrem, 1959). The physical properties and origin of the debris layer are thus important parameters in understanding the history of Martian glaciation and climate. They are also of great interest to the prospect of human exploration of Mars (Gallegos & Newsom, 2015; Head et al., 2015; Levy & Holt, 2015; Mangold et al., 2015; Plaut, 2015), the thickness and composition of the surface debris layer being a significant engineering consideration for the feasibility of ice recovery from lobate debris aprons (Beaty et al., 2016).

The surface debris layer has been hypothesized to form (1) as the result of accumulation of talus weathered from the headwalls above lobate debris aprons (Levy et al., 2016), (2) as the result of a sublimation lag produced as the surface lowers and endemic dust and debris content builds up (Head et al., 2006), and/or (3) as the result of aeolian mantling of dust, sediment, and younger ice (Mangold, 2003). These hypothesized mechanisms imply large differences in debris layer grain size distribution, from cobbles and large boulders (headwall erosion) to dust and fines (aeolian mantle).

Many previous studies have looked to surface morphology to address debris layer properties (Kress & Head, 2008; Mangold, 2003). Surface morphologies commonly observed on lobate debris aprons include raised flow-parallel lineations, sublimation pits-and-buttes referred to as “brain terrain,” and thermal contraction crack polygons (Levy et al., 2010; Levy et al., 2009; Mangold, 2003). “Brain terrain” is hypothesized to form by differential ablation of ice under a discontinuous debris layer; debris collected in ice cracks seeded by thermal contraction and/or glacial flow produces the observed hillocks of debris in a process of topographic inversion as the ice table lowers (Levy et al., 2009).

Despite the topographic and geomorphic evidence, little direct evidence was available to confirm the existence of ice in viscous flow features. Results from the Gamma Ray Neutron Spectrometer aboard Mars Odyssey revealed a distinct lack of hydrogen in the regions of interest–indicating that lobate debris aprons are desiccated of water ice in the near subsurface (Boynton et al., 2002; Feldman et al., 2004). It was not until the advent of orbital radar sounding that we were able to probe into the depths of aprons.

The Shallow Radar Instrument (SHARAD) on board Mars Reconnaissance Orbiter (MRO) (Seu et al., 2007) provides a geophysical method of constraining the bulk composition of these features and has been used to probe the interiors of targeted lobate debris apron in both the southern (Holt et al., 2008) and northern (Plaut et al., 2009) hemispheres of Mars. SHARAD data exhibits subsurface reflectors at depth which were found to coincide with the expected base of the lobate debris apron when a dielectric constant of 3 - 3.2, consistent with high purity (>80%) water ice, is used to correct the time delay radar data to depth. This observation, along with the lack of any internal reflections, scattering, or significant degree of attenuation, led the authors to interpret these lobate debris aprons as debris-covered glaciers. Furthermore, the lack of a candidate reflector for the interface between the surface debris layer and ice core placed an upper bound on the surface debris layer thickness at 10 m (effective SHARAD resolution), while neutron spectrometer data placed a lower bound on the thickness at 0.5 m (Boynton et al., 2002; Feldman et al., 2004).

Holt et al. (2008) and Plaut et al. (2009) completed their work on a small number of lobate debris aprons, describing the analysis of five SHARAD tracks in total. No study has yet been published describing a systematic SHARAD survey to assess regional compositional and/or structural variability across many lobate debris aprons. This is, in part, the focus of this dissertation.

A RADAR SURVEY OF MARTIAN LOBATE DEBRIS APRONS

Chapter 3: All Lobate Debris Aprons Penetrated by SHARAD are Debris-covered Glaciers: Evidence From an Orbital Radar Sounding Survey

This Chapter was submitted as a paper in July 2018 to Geophysical Research Letters.

ABSTRACT

Lobate debris aprons are Martian landforms with a strong morphologic resemblance to rock glaciers and debris-covered glaciers. While the Shallow Radar (SHARAD) sounder has confirmed that a handful of lobate debris aprons are composed of >80% water ice, viscous flow morphology can also be produced by as little as 30% ice. To distinguish between these endmembers, we conducted the first comprehensive regional SHARAD survey of lobate debris aprons, in Deuteronilus Mensae. We found that the majority of aprons are penetrated by SHARAD and determine that they are composed of a material with $\varepsilon' = 3$ and $\tan\delta \approx 0.002 < 0.005$. This work provides evidence that lobate debris aprons across the entire region are consistently composed of >80% water ice, constraining the regional sequestered ice budget to a minimum of 0.9-1.0 x 10^5 km^3 or roughly 4x the combined volume of the Great Lakes.

INTRODUCTION

Lobate debris aprons are Martian landforms thought to contain some quantity of ice due to their viscous flow morphology analogous to terrestrial rock glaciers (Lucchitta, 1984; Squyres, 1978). Rock glaciers can be composed of a pure glacier ice core (e.g. Potter, 1972) or a layered ice-rock mixture with 30-80% ice buried beneath a surface lithic debris layer (e.g. Clark et al., 1998; Degenhardt, 2003; Haeberli et al., 2006).

The global distribution of lobate debris aprons is concentrated in the latitudinal bands ~30°- 60° North and South (Squyres, 1979). Water ice is not currently stable at the surface in these latitudes (Mellon & Jakosky, 1993), and lobate debris aprons are thought to have formed some hundreds of millions of years ago during periods of high orbital obliquity when ice was stable (Fassett et al., 2014; Forget et al., 2006; Mangold, 2003; Mellon & Jakosky, 1995). They are records of Amazonian climate history for modelers seeking to unravel Mars' ice and dust cycles (Madeleine et al., 2009). They are also targets of potential manned missions to Mars investigating the feasibility of utilizing water ice reservoirs in the mid-latitudes (Beaty et al., 2016).

The Shallow Radar Instrument (SHARAD) onboard Mars Reconnaissance Orbiter (MRO) (Seu et al., 2007) provides a geophysical method of constraining bulk composition, which has been demonstrated for targeted lobate debris aprons (Holt et al., 2008; Plaut et al., 2009). SHARAD data exhibits subsurface reflectors at depth which were found to coincide with the expected base of the lobate debris apron when a dielectric constant of 3 - 3.2, consistent with high purity (> 80%) water ice, is used to correct the time delay radar data to depth. This observation, along with the lack of scattering and low attenuation, led the authors to interpret these lobate debris aprons as debris-covered glaciers. Furthermore, the lack of a candidate reflector for the interface between the surface debris layer and interior placed an upper bound on the surface debris layer thickness at ~10 m (effective SHARAD resolution), while neutron spectrometer data placed a lower bound on the thickness at 0.5 m (Boynton et al., 2002; Feldman et al., 2004).

Holt et al., 2008 and Plaut et al., 2009 completed their work on a small number of lobate debris aprons, describing analysis of five SHARAD tracks in total. To date, a number of questions remain unanswered about lobate debris aprons. Is there any regional variability in the interior composition/ice purity of lobate debris aprons? What is the resultant total water ice volume they contain? Do any contain a stratigraphic record that potentially records climate cycles? We address these questions by presenting a comprehensive SHARAD survey in the northern dichotomy boundary regions of Deuteronilus Mensae and Protonilus Mensae.

STUDY REGION

Deuteronilus and Protonilus Mensae are neighboring regions in the northern hemisphere along the dichotomy boundary between the ancient southern highlands and Amazonian-aged northern lowlands (Tanaka et al., 2014) (Figure 1a). The area is characterized by mesas and massifs dotting the smooth low-lying plains just north of the dichotomy boundary. Lobate debris aprons reside at the base of mesa scarps and within valleys and canyons in the southern highlands (Squyres, 1978).

METHODS

SHARAD is a chirped radar sounder with a center frequency of 20 MHz and a bandwidth of 10 MHz, resulting in a theoretical vertical resolution in water ice of 8.4 m (Seu et al., 2007). SHARAD's horizontal resolution is 0.3 - 1 km along-track and 3 - 6 km cross-track. Because SHARAD is an orbital radar sounder there is the possibility of reflections from planar surfaces many kilometers from the spacecraft's nadir ground position. Synthetic aperture processing of the data reduces this effect along-track, but off-nadir surface reflections in the cross-track direction often masquerade as subsurface signals. To discern these echoes, also known as deterministic clutter, We used simulations of SHARAD surface echoes based on Mars Orbital Laser Altimeter (MOLA) topography (Smith et al., 2001) to identify surface clutter when interpreting SHARAD data (Choudhary et al., 2016).

We analyzed 507 radar observations (refered to as radargrams) located in Deuteronilus and Protonilus Mensae to determine the regional distribution and reflection power of surface and subsurface reflections from aprons (Figure 1b). The publicly available US SHARAD Planetary Data System (PDS) data product was used. For each radargram a clutter simulation (or cluttergram) was produced (Choudhary et al., 2016) and radar reflections mapped as follows (examples of radargrams, cluttergrams, and mapped reflectors are shown in Figures 2-3):

LDA Surface Reflections: radar reflections from the surface of lobate debris aprons (LDA). Morphologic mapping by Levy et al., 2014 was used in conjunction with the nadir surface reflection predicted by cluttergrams to aid in radar picking.

LDA Subsurface Reflections: radar reflections beneath apron surfaces not predicted by clutter simulation.

LDA Subsurface Non-Detections: aprons identified by morphology (Levy et al., 2014) that exhibit neither candidate subsurface reflections nor deterministic clutter.

If an imaged subsurface reflection is from the basal contact between the lobate debris apron and underlying bedrock, then the dielectric constant can be determined by depth-correcting the radar travel time to the expected thickness of the apron. We calculated the dielectric constant ε' for each SHARAD trace with a mapped LDA subsurface reflection as follows:

$$\varepsilon' = \left(\frac{tc}{2(z_{srf} - z_{base})}\right)^2 \quad (2)$$

where t is the two-way travel time measured between surface and subsurface reflections, c is the speed of light in vacuum, z_{srf} is the surface elevation of the apron, and z_{base} is the elevation of the apron base.

We derived z_{srf} from the SHARAD surface return registered to MOLA data and set z_{base} to be congruent with the nearest plains elevation observed in SHARAD beyond the toe of the apron. This approximates to first order the flat plains extending beneath the apron body, however we also acknowledge that there will be topographic variability due to e.g. small-scale hills, depressions, and talus slopes found near scarp walls that will produce noise in our results.

The loss tangent tanδ indicates radar attenuation in a given material and can be a good indicator of ice purity (e.g. Campbell & Morgan, 2018; Grima et al., 2009). We calculated tanδ following (Grima et al., 2009) from measured surface (*Ps*) and basal (*Pb*) reflection power, two-way travel time t, SHARAD center frequency f (20 MHz), and assumed surface dielectric constant ε'_{srf}:

$$P_t = P_s\left[\left(\frac{\sqrt{\varepsilon_{srf}'}+1}{\sqrt{\varepsilon_{srf}'}-1}\right)^2 - 1\right] \quad (3)$$

$$tan\delta = \frac{10log_{10}\left({}^{P_t}/_{P_b}\right)}{0.091ftc} \quad (4)$$

$$\alpha = 91f\sqrt{\varepsilon'}tan\delta \quad (5)$$

The power transmitted through the surface *Pt* is calculated from the measured surface reflection power *Ps* using fresnel coefficients. Note that ε'_{srf} is that of the surface

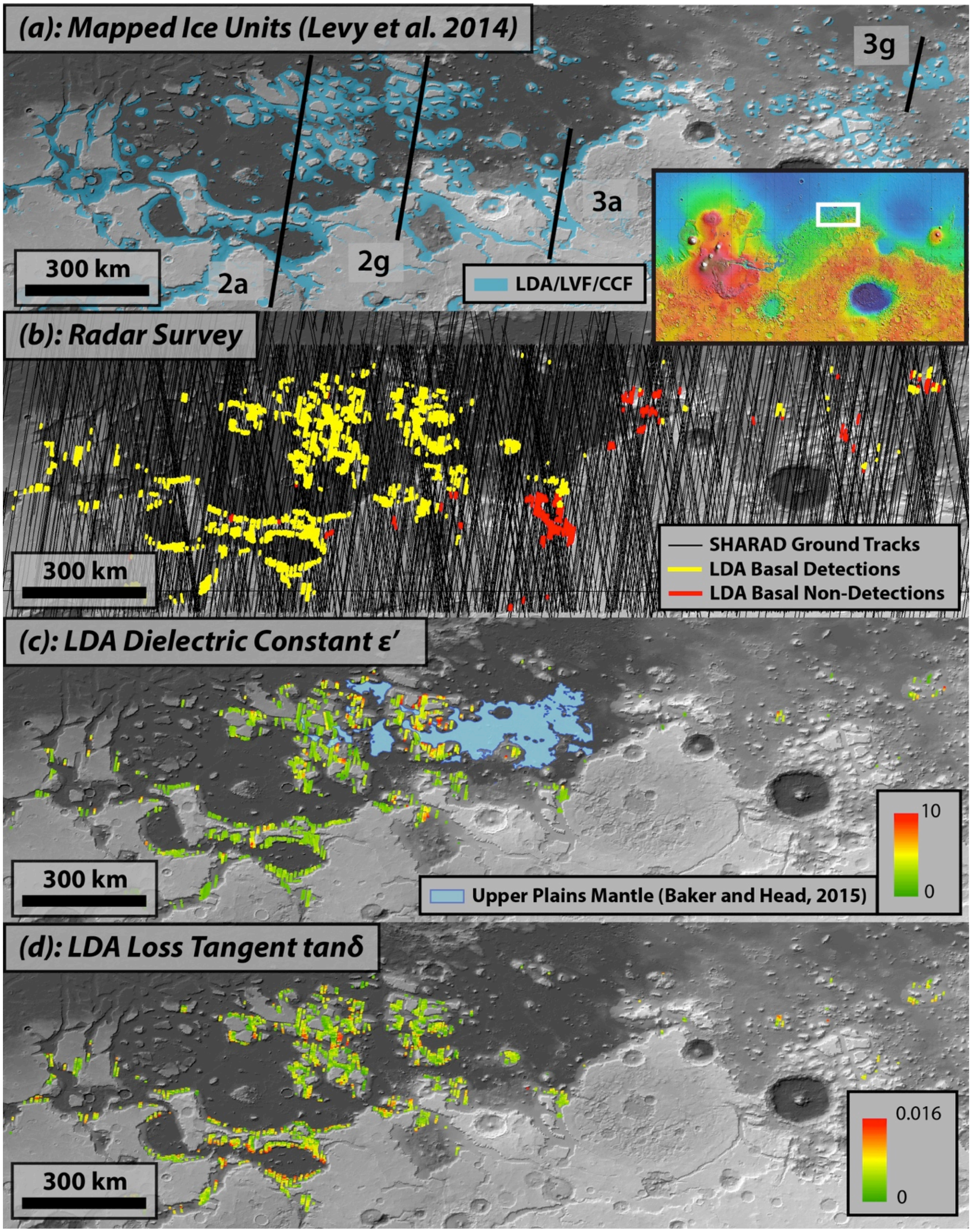

Figure 1: (Caption on following Page)

Figure 1: (Previous page) MOLA-derived map of Deuteronilus/Protonilus Mensae. (a) Extent of lobate debris aprons as mapped by Levy et al. (2014). (b) SHARAD coverage and mapped detections/non-detections of LDA basal reflectors. (c) Bulk dielectric constant ε′ determined from depth-conversion to nearest plains elevation; the upper plains mantle (Baker and Head, 2015) is also mapped to show correlation with high ε′ values in north-central Deuteronilus Mensae. (d) Loss tangent tanδ derived from measured reflection powers ($\varepsilon'_{srf} = 5$). Selected radargrams shown in Figures 2-3 are mapped in (a).

debris and we used a range of 3-8 consistent with compositions from high-porosity ice-rich dust (Bramson et al., 2015; Heggy et al., 2006; Stuurman et al., 2016) to low-porosity basalt (Carter et al., 2009; Reynolds, 1997).

RESULTS

For all SHARAD observations made of lobate debris aprons in this region, 51.7% were clutter free, while the remaining 48.3% exhibiting geometries that produced off-nadir clutter preventing subsurface signal detection (examples are shown in Figure 4). For clutter-free observations, apron subsurface reflections were detected in 86.7% of all SHARAD traces across Deuteronilus Mensae (Figure 1); many of these are in the central-to-western Deuteronilus Mensae region. At most a single subsurface reflection was imaged. Confirmed non-detections of subsurface signal were less common, being observed in 13.4% of SHARAD traces. Non-detections were most abundant in eastern Deuteronilus Mensae and Protonilus Mensae.

The distribution of calculated dielectric constant values produced a median of 3.0 and a standard deviation of 2.1 (Figure 5a). Many high values (> 4) map to lobate debris aprons centered on mesas in the northern-central region of Deuteronilus Mensae (Figures 1c, 2j-k). There is no correlation (R^2 = 0.001) between basal reflection power and dielectric constant, nor is there any correlation between dielectric constant and proximity to mapped basal non-detections.

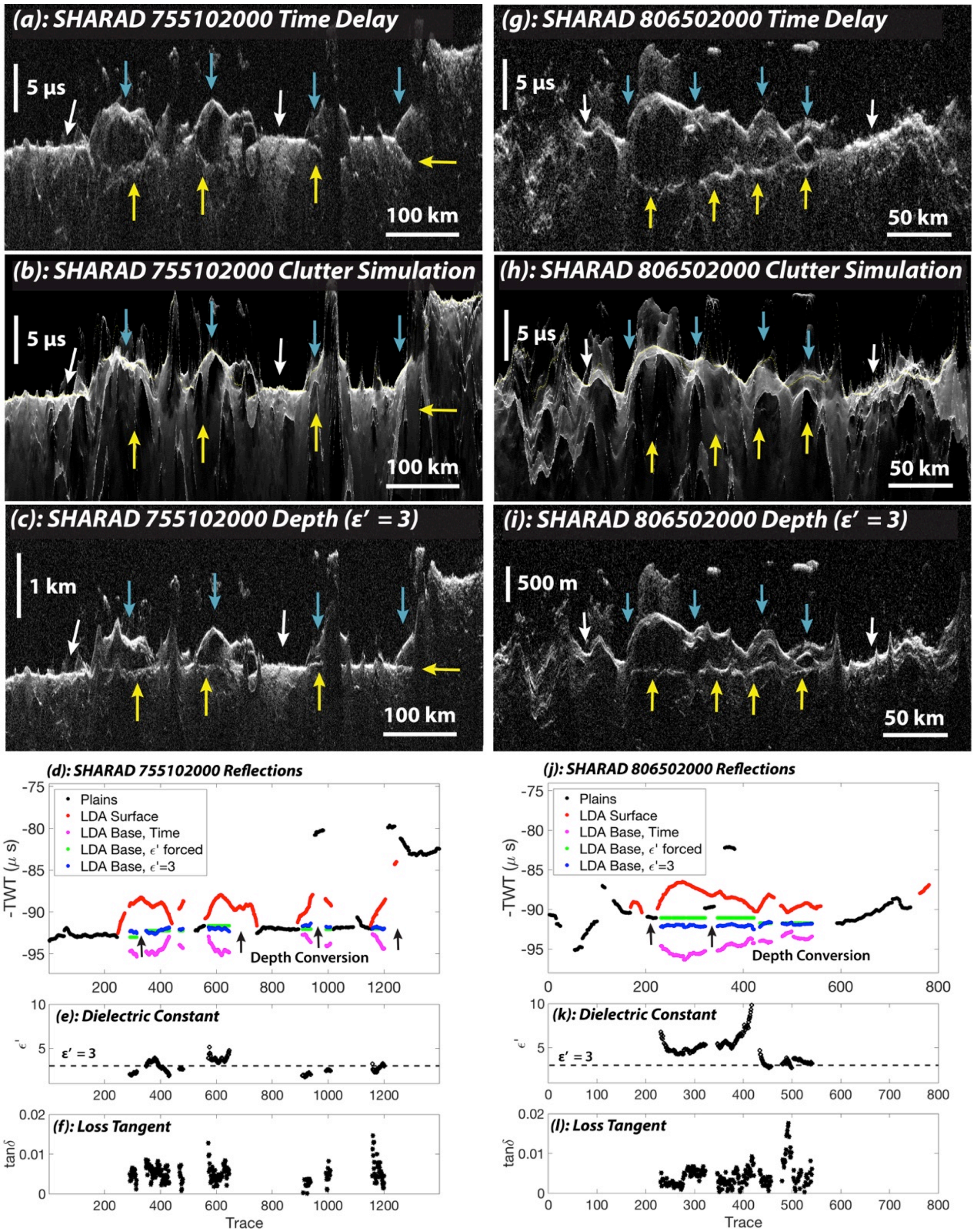

Figure 2: (Caption on following page)

Figure 2: (Previous page) Sample SHARAD Data for Lines (a-f) 755102000 and (g-k) 806502000. (a,g) SHARAD radargram in time delay. (b,h) Clutter Simulation used to distinguish subsurface signal from off-nadir surface reflections. (c,i) SHARAD radargram converted to depth assuming bulk dielectric constant $\varepsilon' = 3$. Blue arrows indicate radar reflections from the surface of lobate debris aprons, yellow arrows indicate radar reflections thought to be from the base of lobate debris aprons, and white arrows indicate radar reflections from plains surrounding lobate debris aprons. (d,j) Mapped radar reflectors comparing depth conversion using $\varepsilon' = 3$ vs. ε' forced to match the basal elevation with the nearest plains elevation. (e,k) ε' required to force the base to the nearest plains elevation. (f,l) $\tan\delta$ calculated at each trace for the lobate debris aprons. Radargram locations are mapped in Figure 1 and north is to the left.

The median and standard deviation of the calculated loss tangents range between 0.0035 ± 0.0037 for $\varepsilon'_{srf} = 8$ and 0.0054 ± 0.0039 for $\varepsilon'_{srf} = 3$ (Figure 6). There are no regional trends in $\tan\delta$; the strongest trend is for greater values near LDA toes where the deposits are thinner and lower values where lobate debris aprons are thicker (Figure 1c). There is no correlation between loss tangent and proximity to basal non-detections.

Discussion

Only a single subsurface reflector was imaged for each lobate debris apron, and each of these was found at time delays consistent with a basal reflector. Our mean calculated dielectric values include $\varepsilon' = 3 \pm 2$ and $\tan\delta = 0.004 \pm 0.004$, which are similar to values found by other studies (Holt et al., 2008; Plaut et al., 2009), but include high levels of uncertainty. The determination of ε' is highly sensitive to topographic variation, while $\tan\delta$ may be skewed high by losses incurred at the surface debris layer.

To assess if the spread in our dielectric constant values is due to topographic variability, we calculated the discrepancy between our assumed value of z_{base} and that

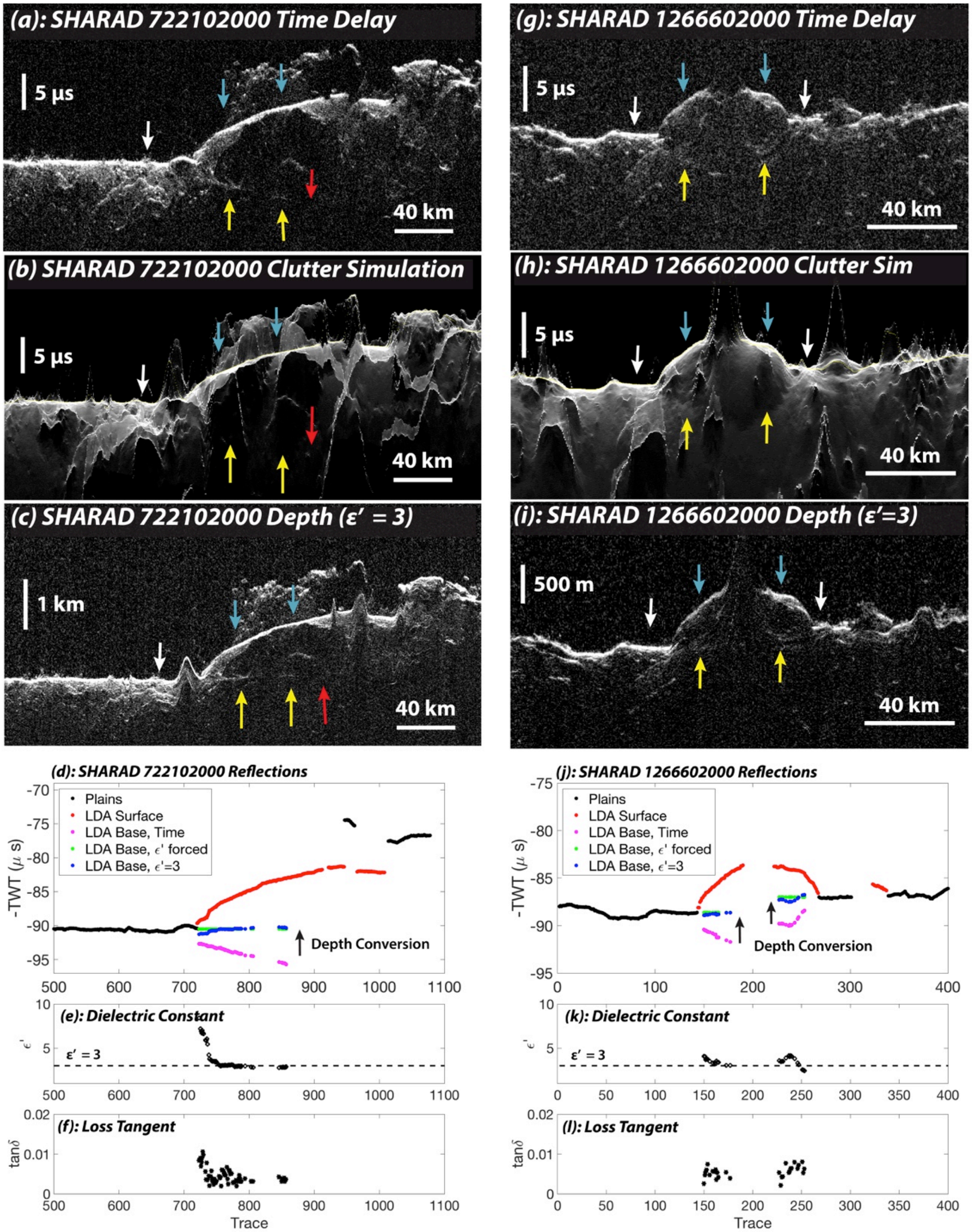

Figure 3: (Caption on following page)

Figure 3: (Previous page) Sample SHARAD Data for Lines (a-f) 722102000 and (g-k) 1266602000. (a,g) SHARAD radargram in time delay. (b,h) Clutter Simulation used to distinguish subsurface signal from off-nadir surface reflections. (c,i) SHARAD radargram converted to depth assuming bulk dielectric constant ε′ = 3. Blue arrows indicate radar reflections from the surface of lobate debris aprons, yellow arrows indicate radar reflections thought to be from the base of lobate debris aprons, and white arrows indicate radar reflections from plains surrounding lobate debris aprons. (d,j) Mapped radar reflectors comparing depth conversion using ε′ = 3 vs. ε′ forced to match the basal elevation with the nearest plains elevation; note in (j) the constant offset between the depth conversion methods. (e,k) ε′ required to force the base to the nearest plains elevation. (f,l) tanδ calculated at each trace for the lobate debris aprons. Radargram locations are mapped in Figure 1 and north is to the left.

produced from the median value of ε′ = 3. We found that this discrepancy is fit well (R^2 = 0.997) by the sum of two gaussians with standard deviations of 35 m and 140 m (Figure 5b). These are interpreted as corresponding to random small-scale fluctuations (hills, swales, scarp-proximal talus slopes) and large-scale fluctuations (misrepresented plains elevation, large valleys, regional slope), respectively, that are not captured by our assumption of flat basal topography. This topography can be observed in the radar data when it is corrected to depth using a dielectric constant of ε′ = 3; realistic topographic variations appear, including small hills/swales and very frequently a small increase in slope and elevation proximal to the headwall scarps above lobate debris aprons. Such an increase in bed topography slope can be attributed to mass wasting debris aprons ("true" debris aprons) found beneath the ice-rich aprons.

The most conspicuous feature of our dielectric constant estimation is the higher values concentrated in central-northern Deuteronilus Mensae. These are found to correlate strongly with the extent of the "upper plains unit" mapped by Baker & Head (2015) (Figure 1c), which is a young ice-rich mantle emplaced after and embaying the edges of lobate debris aprons. The unit thickness is estimated as 50-100 m, with a mean of 85 m (Baker & Carter, 2017; Baker & Head, 2015). Similarly, our plains-derived z_{base} values in this area are on average 70 m higher than the resultant z_{base} when $\varepsilon' = 3$ is used. We thus attribute the high dielectric constant values calculated here to be a feature of overestimation of z_{base} as a result of the presence of the upper plains unit; $\varepsilon' \approx 3$ is a more appropriate value in this case. The overestimation offset can be seen in Figure 3j, and an illustration of its effect is shown in Figure 7.

At 10s of MHz radio frequency similar to SHARAD, water ice exhibits a dielectric constant of $\varepsilon' = 3$ for temperatures of < 200 K (Heggy et al., 2008) and $\varepsilon' = 3.1 - 3.2$ for temperatures in the range of 200-273 K (Gough, 1972; Johari, 1976). The temperature of apron interiors should be 195-205 K based on present-day mean annual temperature at these latitudes (Mellon et al., 2004) and the temperature modeled based on orbital cycles for the past 5 Ma (Schorghofer, 2008). Our analysis produced a result ($\varepsilon' = 3$) consistent with water ice < 200 K. This result echoes the work of Holt et al. (2008) ($\varepsilon' = 3.2$) and Plaut et al. (2009) ($\varepsilon' = 3$) for lobate debris aprons and Grima et al. (2009) for the North Polar Layered Deposits ($\varepsilon' = 3.10 \pm 0.12$). These authors drew the conclusion that their targets were made up in bulk of water ice with an impurities fraction of no greater than 10-20%. We similarly find that our results indicate evidence for widespread pure water ice in the bulk interior of lobate debris aprons, with an impurities fraction of less than 20%.

Note that our calculation of the loss tangent hinges on determining the power transmitted into the subsurface from the measured surface reflection power. Following the equations in the Methods section, we assume a smooth surface and use the Fresnel reflection and transmission coefficients to do this. In the case of a roughened surface, however, the coherent power transmitted into the subsurface is reduced. Failing to take this into account, our calculated loss tangent is a maximum. An additional source of

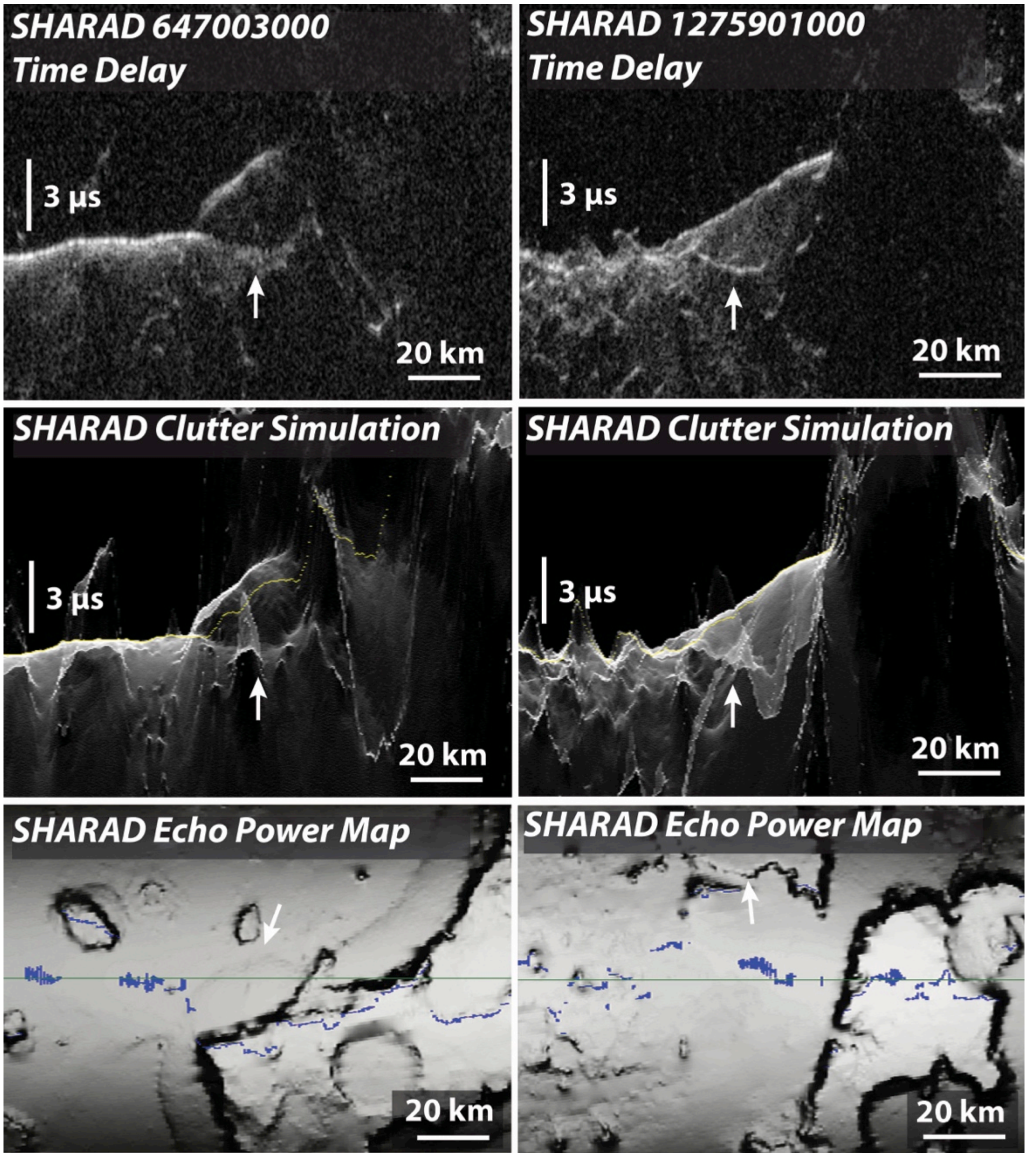

Figure 4: Example radar observation in which echoes from off-nadir sources clutter the data, obscuring and/or masquerading as subsurface signal. (Top panels) radar observations of lobate debris aprons in Deuteronilus Mensae, with candidate subsurface signal indicated by white arrows. (Middle panels) clutter simulations produced in house at UT; clutter is predicted at the same location as the candidate subsurface signal. (Bottom panels) echo power maps produced by the clutter simulation of Mars' surface in the observation area. Possible sources of clutter, including the apron toe and a distant mesa, are indicated by the white arrows.

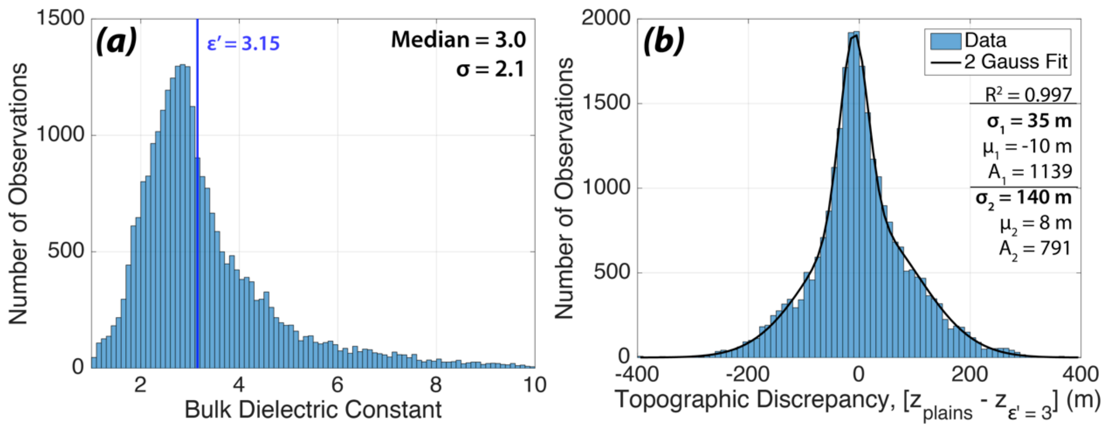

Figure 5: (a) Distribution of bulk dielectric constant values required to force the elevation of lobate debris apron basal reflections to the nearest plains elevation. (b) The discrepancy in meters between the nearest plains elevation and lobate debris apron basal elevation calculated assuming $\varepsilon' = 3$; this distributionis fit well ($R^2 = 0.997$) by the sum of two gaussians centered at -10 m and +8 m with standard deviations of 35 m and 140 m and amplitudes of 1139 and 791, respectively.

uncertainty is near-surface volume scattering and fine-scale layering that may produce resonances or otherwise unpredictable reflection and transmission coefficients.

We can explore these effects mathematically by introducing a perturbation parameter χ' to our idealized P_t to produce P_t':

$$P_t' = \chi' P_t \tag{6}$$

Where the perturbation parameter is a catch-all for losses due to surface roughness, fine-scale layering, and volume scattering in the near-subsurface (less than the radar resolution). This perturbed P_t can then be used to calculate the perturbed loss tangent $tan\delta'$ as:

$$tan\delta' = \frac{10log_{10}\left(\chi' P_t / P_b\right)}{0.091ftc} \tag{7}$$

$$tan\delta' = tan\delta + \frac{10log_{10}(\chi')}{0.091ftc} \tag{8}$$

Note that the degree to which the perturbation parameter modifies the loss tangent is depends on the inverse of two-way travel time *t*; as $t \rightarrow \infty$ (as we examine thicker aprons) the perturbed loss tangent becomes more similar to the unperturbed loss tangent.

An additional level of uncertainty arises due to the fact that our calculated tanδ is representative of the full travel time *t* through the lobate debris apron, and may be skewed due to lossy surface debris layer. We can mitigate this uncertainty by assuming a two-layer model with a surface debris layer (layer 1) of constant thickness over the bulk apron interior (layer 2). The effective *tanδ* can then be calculated from surface debris layer travel time t_1 and loss tangent $tan\delta_1$ and apron interior loss tangent $tan\delta_2$:

$$tan\delta(t) = \begin{cases} tan\delta_1 & t \leq t_1 \\ \frac{p_1 t + p_2}{t} & t \geq t_1 \end{cases} \tag{9}$$

$$p_1 = tan\delta_2 \tag{10}$$

$$p_2 = t_1(tan\delta_1 - tan\delta_2) \tag{11}$$

Note the effective *tanδ* as a function of two-way travel time *t* has the same rational form as the perturbed loss tangent *tanδ'* above. We can introduce the perturbation parameter into the two-layer model to obtain the following:

$$tan\delta'(t) = \begin{cases} tan\delta_1 + \frac{10log_{10}(\chi')}{0.091ftc} & t \le t_1 \\ \frac{p_1't+p_2'}{t} & t \ge t_1 \end{cases} \tag{12}$$

$$p_1' = tan\delta_2 \tag{13}$$

$$p_2' = t_1(tan\delta_1 - tan\delta_2) + \frac{10log_{10}(\chi')}{0.091ftc} \tag{14}$$

Note that the perturbation parameter passes entirely into the second parameter p_2', leaving $p_1' = tan\delta_2$ unchanged. We performed a rational fit of the form shown in Equations 9 & 12 above to our data in an effort to constrain the $tan\delta_2$ of the lobate debris apron interior. Note that in the case of $tan\delta_1 >> tan\delta_2$ (which is expected for lossy debris atop a more lossless ice-rich interior) and negligible χ' we have the convenient indicator $p_2 \approx t_1 tan\delta_1$; doubling p_2 can be an indication of a doubly thick or doubly lossy debris layer.

The fit produced $p_1 = tan\delta_2 = 1.85\times10^{-3}$, independent of the assumed ε'_{srf}, and $p_2 \approx t_1 tan\delta_1 = 9 - 20$ ns, dependent on ε'_{srf} (Figure 6). R^2 ranges between 0.40 for $\varepsilon'_{srf} = 3$ and 0.13 for $\varepsilon'_{srf} = 8$. In the plot of tanδ as a function of two-way travel time t (Figure 5b) we observe a much wider spread in tanδ values towards shorter travel times (thicker aprons), while tanδ values at longer time delays exhibit lower values with less spread. This supports the hypothesis that the surface debris layer produces non-trivial radar loss / variability and that the loss tangent in the lobate debris apron interior is less than that which we initially calculate.

Our results indicate a loss tangent in the bulk interior of lobate debris aprons as low as tanδ = 0.002 and certainly below tanδ = 0.005. This result is similar to the values of tanδ = 0.002 ± 0.0008 found by Campbell & Morgan (2018) for lobate debris aprons and $\tan\delta = 0.0026 \pm 0.0005$ found by Grima et al. (2009) for the North Polar Layered Deposits. Loss tangent values between 0.001 and 0.005 are taken as typical for water ice at martian conditions (Heggy et al., 2008; Plaut et al., 2007; Watters et al., 2007). This result thus provides additional support for a pure water ice composition for lobate debris apron interiors.

If we assume no losses due to surface roughness, our constrained parameter p_2 implies that a debris layer 10 m thick requires a loss tangent in the range of $tan\delta_1$ = 0.05–0.17, while a thinner debris layer requires a larger loss tangent value. This result implies either a surface debris layer composed of very lossy material, or the addition of non-negligible losses due to surface roughness and/or near-surface volume scattering. Based on research into apron surface roughness (Petersen et al., 2017) presented in the following chapter, we prefer the latter interpretation.

Where no clutter is present to obscure subsurface signals we map subsurface detections in 87% of SHARAD traces over lobate debris aprons. The cause of non-detection for the remaining 13% may be due to (1) surface roughness causing increased radar scattering and reduced nadir signal return, (2) increased attenuation within the surface debris layer, (3) increased attenuation within the lobate debris apron bulk interior, (4) roughness of the basal interface, and/or (5) reduced dielectric contrast at the basal interface. Our quantification of low loss tangents in the bulk interior of lobate debris aprons with subsurface detections implies that hypothesis (2) is unfeasible – high loss tangents are not observed within or near lobate debris aprons that also exhibit non-detections. Our treatment of the two-layer lobate debris apron model for radar loss shows that there is much variability in and high losses due to the surface debris layer, providing evidence in support of hypotheses (1) and (2).

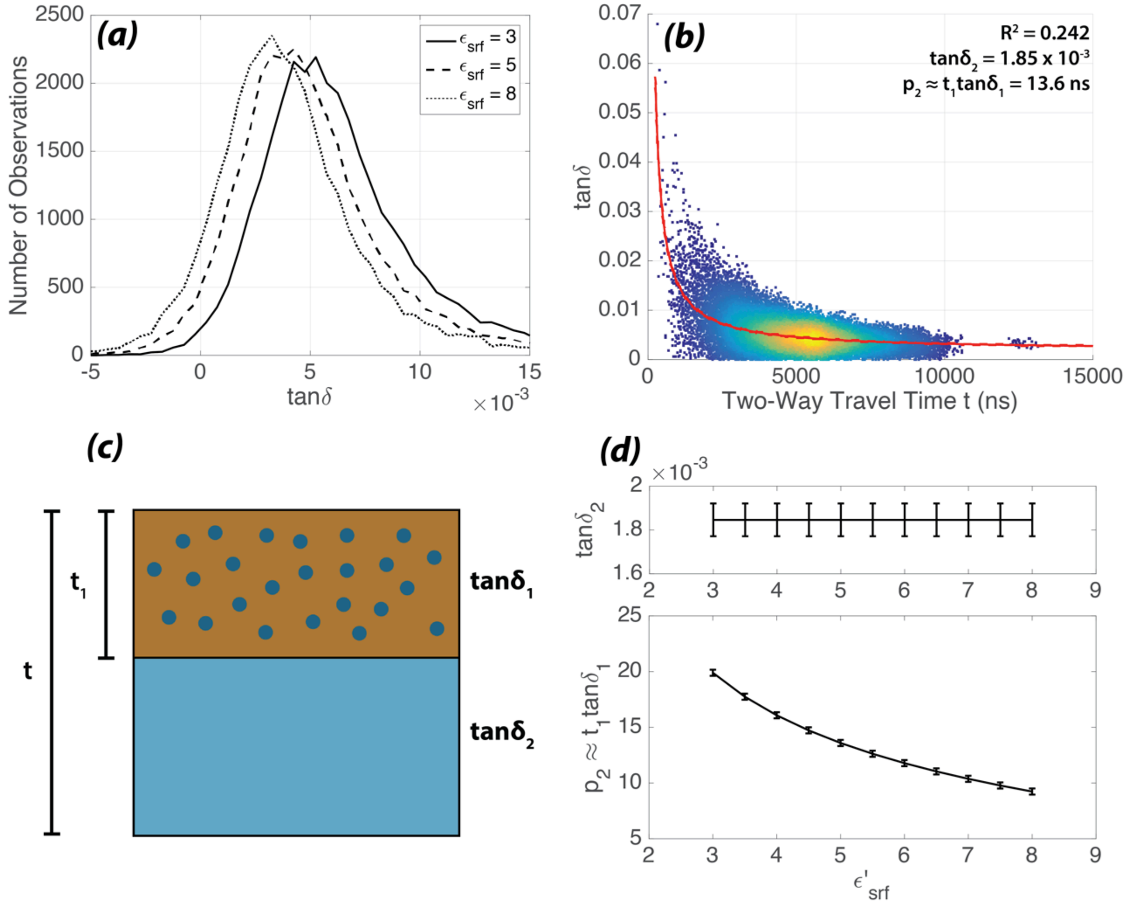

Figure 6: (a) Distributions of calculated loss tangent assuming values of ε'_{srf} = 3, 5, and 8 for the dielectric constant of the surface debris layer used in calculating Fresnel transmissivity. (b) Calculated loss tangent (for ε'_{srf} = 5) as a function of the two-way travel time t; a fit of the form shown in equation 5 has been applied, yielding the fit parameters shown. (c) Illustration of two-layer model for lobate debris aprons from which we derive equation 5; $tan\delta_1$ and $tan\delta_2$ are the loss tangent in the surface debris layer and apron interior respectively, and t_1 and t are the two-way travel time through the surface debris layer and the full thickness of the apron respectively. (d) Fit parameters as a function of assumed values of ε'_{srf}; $tan\delta_2$ remains constant.

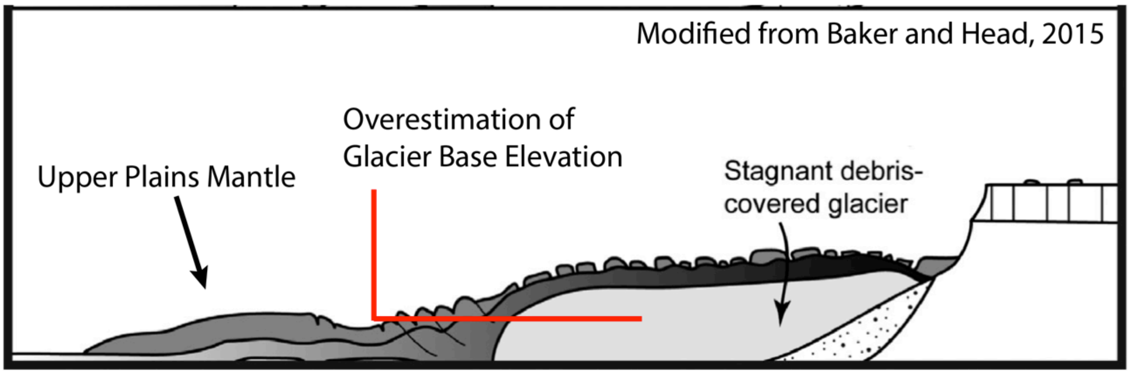

Figure 7: An illustration of the effect that the upper plains mantle has on producing an overestimation of the lobate debris apron basal elevation. Modified from a figure by (Baker & Head, 2015).

We can synthesize our ice content constraints with the mapping results of Levy et al. (2014) to produce regional volume estimates for ice in lobate debris aprons. In that study, the features were mapped in Mars Reconnaissance Orbiter Context Camera (CTX) images across the planet for the latitudinal bands of 30-50° N and S. Lobate debris aprons were mapped according to the geomorphic guidelines set by (Head et al., 2010), and their surface elevation extracted from MOLA. The volume was then calculated for each apron assuming the base is a flat plane at the elevation of the lowest point along the apron border. This is similar to our study's method of using the nearest plains elevation as the apron basal elevation. For each lobate debris apron that exhibited subsurface reflections in our study we extracted the volume estimates from Levy et al., 2014 and summed them to provide the region-wide estimate of lobate debris apron volume confirmed to be composed of pure water ice. We found ~1.1×10^5 km^3 of debris-covered glacier material in the region. This is equal to ~42% of the total lobate debris apron volume found globally, highlighting the high concentration of the features in Deuteronilus Mensae. Assuming 80-90% ice content this yields a total of $0.9–1.0\times10^5$

km^3 of water ice, the equivalent of roughly 4x the combined volume of water in the Great Lakes.

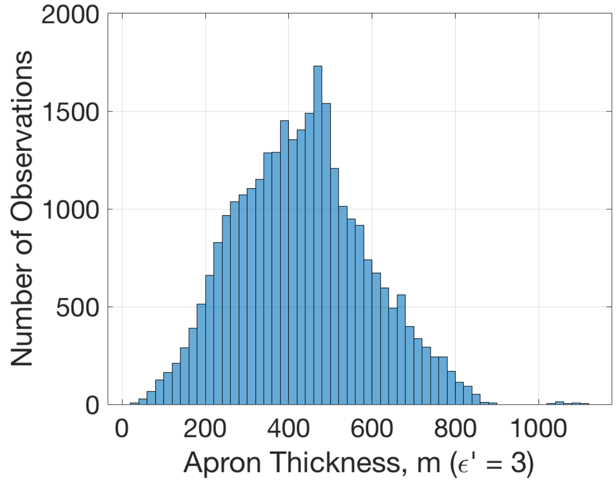

Figure 8: The distribution of lobate debris apron thicknesses found in this study, calculated from measured two-way travel time assuming a bulk dielectric constant of $\varepsilon' = 3$. The median value is 430 m and the standard deviation 160 m; maximum is 1,111 m.

Conclusions

We mapped SHARAD reflections from the surface and subsurface of lobate debris aprons in Deuteronilus Mensae. A majority of aprons exhibited detectable subsurface reflections; for these we found a bulk dielectric constant of $\varepsilon' \approx 3$ and an interior loss tangent of $\tan\delta \approx 0.002 < 0.005$. These values support the hypothesis that they are debris-covered glaciers composed of pure (> 80%) water ice beneath a surface debris layer.

Our analysis of loss tangents in the context of a two-layer model additionally shows that much of the radar losses occur at the surface debris layer while lobate debris apron interiors are consistently more lossless. This implies that aprons without detectable subsurface reflections in SHARAD have a similar internal composition of pure water ice, but may experience increased radar losses at the surface debris layer.

Our work supports the hypothesis that all aprons are debris-covered glaciers, with 80% or more of their volume composed of water ice. Synthesizing our results with the mapping work of Levy et al. (2014) we find 1.1×10^5 km^3 of debris-covered glacier material in the region, or a total of $0.9–1.0\times10^5$ km^3 of water ice. That's the equivalent of roughly 4× the combined volume of the Great Lakes, or 25× the combined volume of all glacier ice in Iceland, and accounts for nearly half the volume of all lobate debris aprons on Mars. These are nontrivial water ice reservoirs and may one day prove invaluable resources to manned exploration or colonization of Mars.

Chapter 4: Surface Roughness Prevents Radar Penetration of Some Lobate Debris Aprons

INTRODUCTION

The previous Chapter introduced a SHARAD radar survey mapping detections and non-detections of subsurface reflections associated with lobate debris aprons. Because radar provides the most direct evidence for the pure water ice composition of aprons, those without radar detections retain some level of ambiguity about their composition. It may be the case that reduced ice content may be responsible. In this chapter we address the issue of non-detections to determine their cause and thereby whether or not a differing bulk composition is required to explain the observations.

Fundamentally, the losses experienced by a SHARAD radio wave penetrating through an apron and returning from its base are many and include: (1) Fresnel transmissivity of the surface debris layer, (2) scattering due to surface roughness at the surface debris layer, (3) reduced gain due to surface slope, (4) volume attenuation in the surface debris layer, (5) volume attenuation in the lobate debris apron interior, (6) Fresnel reflectivity of the apron's basal interface, (7) scattering due to roughness of the basal interface, and (8) reduced gain due to the slope of the basal interface. If any of these losses are sufficiently increased they could reduce the power of the basal reflection to below SHARAD's noise floor and prevent detection of subsurface signals.

Mechanism 1 (debris layer transmissivity) involves the dielectric properties of the surface debris layer, including its bulk dielectric constant as well as any thin (sub-radar resolution) layering that may alter its effective reflectivity (Lalich & Holt, 2016). There is published evidence for a complex debris layer stratigraphy, including young layered mantle units deposited on top of the more ancient lobate debris aprons (Baker & Head, 2015; Mangold, 2003). However, a multilayer packet that reduces the transmissivity to below noise level would increase surface reflectivity to a large degree, an effect that is not observed in the data. Additionally, it is unlikely that debris layer stratigraphy is consistent enough in terms of thickness, smoothness, dielectric properties, and dip to orchestrate such an effect.

Mechanism 2 (surface roughness) can have a very dramatic effect on radar sounding when the horizontal scale of roughness is on the same order as the radar wavelength (Campbell, 2002), which is 15 m for SHARAD. Morphologic studies of apron surfaces have described landforms such as brain terrain with very high roughness on the tens of meters scale (Levy et al., 2009; Mangold, 2003), so there is good reason to suspect roughness may exert a strong control over subsurface returns.

Mechanism 3 (surface slope) reduces the radar signal that penetrates and reflects from an apron, dependent upon its surface slope and the radiation pattern of the SHARAD instrument. As the surface slope increases, the location at which the radar penetrates at normal incidence is farther from the direct sub-nadir point; the antenna gain for these geometries may thus decrease as the surface slope increases. Surface slopes of lobate debris aprons are typically 1-2° and can be as high as 5°; we explore later in this chapter whether there is any correlation with the detectability of subsurface returns.

Mechanism 4 (debris layer volume attenuation) can be estimated by prescribing a loss tangent to the debris based on assumptions about its composition and a range of thicknesses consistent with geophysical results. The loss tangent for basalt debris is typically on the order of 0.01 (Heggy et al., 2006), and knowing that the surface debris layer is between 1-10 m thick (Holt et al., 2008; Plaut et al., 2009) we can calculate the resultant total loss as shown in Figure 9a to between 0.05-0.8 dB. This is a very small effect, thus this mechanism is unlikely to impact detectability of subsurface returns.

Mechanism 5 (apron interior volume attenuation) can also be easily quantified, and has been done in the previous Chapter. There we found no correlation between increased loss tangent and non-detections, indicating no linkage between internal composition and signal loss. The total loss through the thickness of the apron can be calculated as in Figure 9b, showing that loss can be significant, but only for sufficiently thick aprons (i.e. > 600 m). This mechanism will thus be re-visited in this chapter for such aprons.

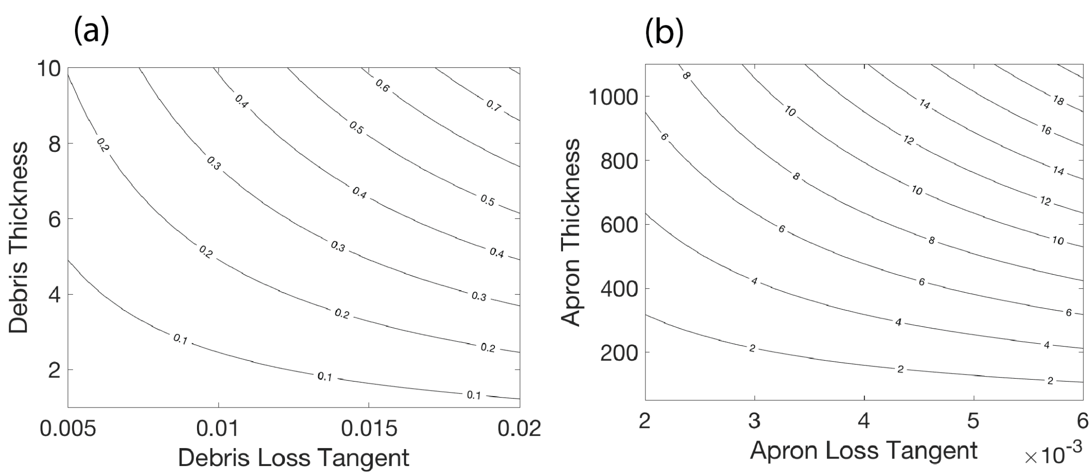

Figure 9: Parameter space for total signal loss endured by a SHARAD signal travelling through (a) the surface debris layer and (b) the lobate debris apron interior. The assumed loss tangent is shown on the x-axis and the thickness of the layer on the y-axis. The debris layer produces losses of less than 1 dB, while the interior apron produces losses > 5 dB for apron thickness > 700 m.

Mechanisms 6-8 related to basal properties are difficult to constrain because we can only infer basal properties based on our observations of the bedrock extending beyond the toe of lobate debris aprons. In general, the Hesperian-aged bedrock material is relatively smooth, flat, and composed of volcanic material and windblown dust (Chuang & Crown, 2009; Lucchitta, 1978; McGill, 2002; Tanaka et al., 2014). Therefore there is little motivation to explore these mechanisms as related to non-detection of basal signals, but we report on anomalies related to these mechanisms.

In this study we explore and quantify the effect of a number of these mechanisms on subsurface radar returns from lobate debris aprons. We tested in particular the hypothesis that surface roughness is chiefly responsible for causing non-detections. We accomplished this by creating high resolution Digital Terrain Models (DTMs) from stereo image pairs to quantify the surface roughness relevant to individual SHARAD observations.

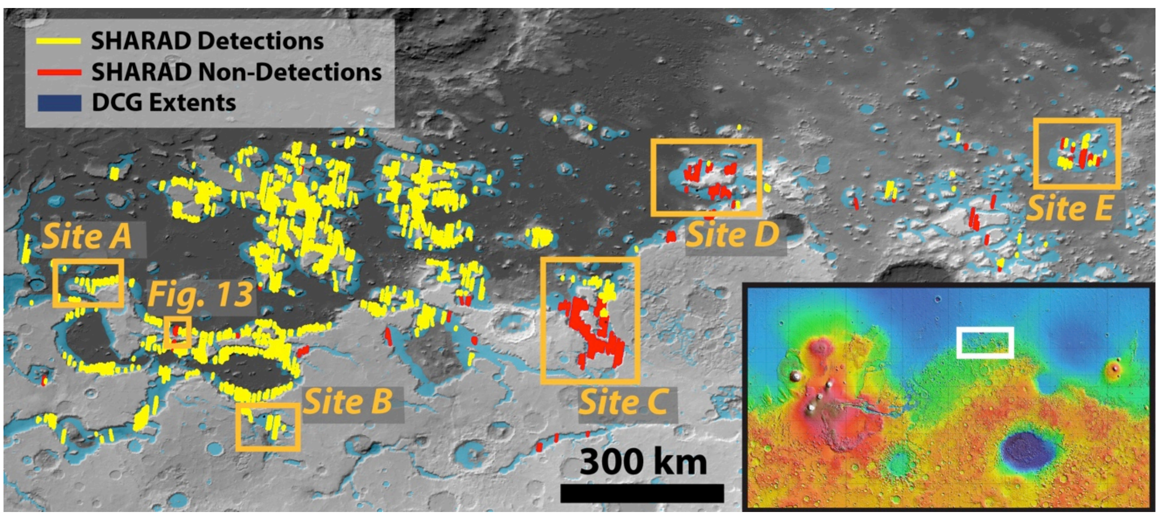

Figure 10: MOLA-derived map of Deuteronilus Mensae with confirmed detections and non-detections of lobate debris apron basal reflectors in SHARAD data. Apron extents are shaded in blue as mapped by Levy et al. (2014). Selected study sites A-E are highlighted in orange boxes. Inset: MOLA elevation map of Mars from 70° S to 70° N with the location of Deuetronilus Mensae mapped in the white box.

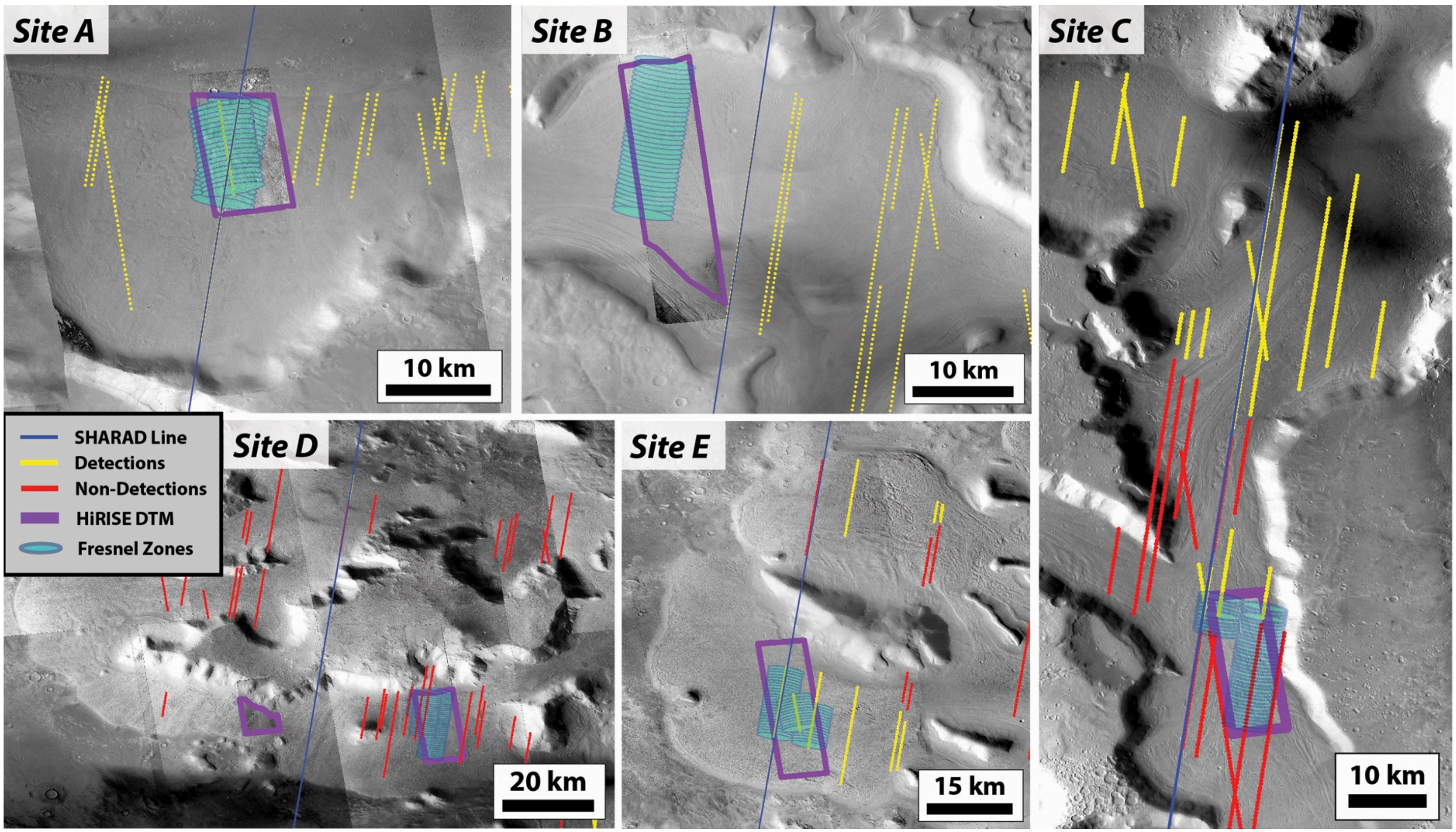

Figure 11: Context camera (CTX) images of each study site with the location of Stereo HiRISE-produced DTMs. SHARAD detections and non-detections of apron basal interfaces are also mapped along with the lines displayed in Figure 3. SHARAD Fresnel Zones (ellipses of size 6 km x 1 km) are mapped for SHARAD observations which overlap with HiRISE DTMs.

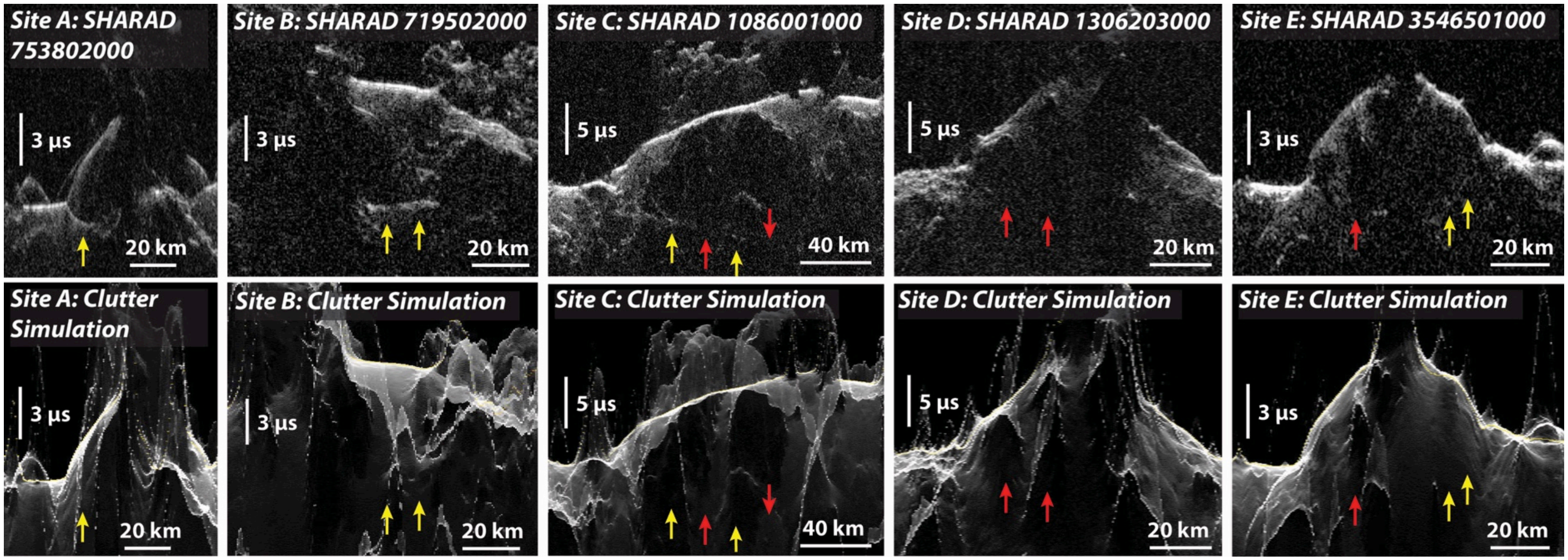

Figure 12: Example SHARAD radargrams and simulated cluttergrams for each study site. Locations of subsurface reflections are indicated by yellow arrows and locations of non-detections are indicated by red arrows.

STUDY SITES

This study focuses on the same regions of Deuteronilus and Protonilus Mensae and the same radar dataset as presented in Chapter 1 (Figure 10). For more general information on Deuteronilus and Protonilus Mensae, refer to the "Study Region" section in Chapter 1.

This study focuses primarily on five lobate debris apron sites in Deuteronilus and Protonilus Mensae (Figures 10-12); each is a contiguous set of apron lobes that has coverage in existing stereo HiRISE data (Section 3.2, Figure 1). Site A is an apron flowing north from a mesa escarpment in western Deuteronilus Mensae; radar returns from Site A were described by Plaut et al. (2009). Site B is an apron filling a large valley near Mamers Valles. Site C is a large apron (studied by Head et al., 2006; Squyres, 1978) filling a large bifurcated valley directly east of Sinton Crater. Site D is an apron flowing from a large massif in eastern Deuteronilus Mensae on the boundary between Deuteronilus and Protonilus Mensae, directly north of Ismeniae Fossae. Site D was the subject of a morphologic study by Baker et al. (2010). Site E is an apron complex surrounding a smaller massif in Protonilus Mensae.

METHODS

We used the results of the SHARAD mapping study presented in Chapter 1, including the mapped distribution and measured SHARAD reflection power for *LDA Surface Reflections*, *LDA Subsurface Reflections*, and *LDA Subsurface Non-Detections*.

The High Resolution Imaging Science Experiment (HiRISE) is a visible and near-infrared imager onboard MRO capable of resolutions up to 25 cm/px (McEwen et al., 2007). We used HiRISE in this work because its resolution allows us to accurately quantify the topography of features on the fifteen to tens of meters scale that we hypothesize has a strong effect on SHARAD radar sounding.

HiRISE is operated in a "push-broom" fashion with an image swath roughly 6-8 km wide; this is larger than SHARAD's surface footprint of 0.3-1 km by 3-6 km. HiRISE thus provides coverage relevant to the SHARAD footprint along with a resolution relevant to SHARAD's wavelength.

DTMs at each site were produced using the open source NASA Ames Stereo Pipeline, which constructs high-resolution DTMs from targeted images using stereo photogrammetry algorithms (Broxton & Edwards, 2008; Moratto et al., 2010; Shean et al., 2016). DTMs with a resolution of 1 m/px were produced from HiRISE Stereo Pairs ESP_033653_2225 and ESP_033363_2225 (Site A), ESP_024594_2180 and ESP_016168_2180 (Site B), ESP_042435_2210 and ESP_042725_2210 (Site C), ESP_016418_2255 and ESP_017130_2255 (Site D), and ESP_046496_2260 and ESP_046430_2260 (Site E).

We then produced individual crops of the DTMs in the shape of ellipses 6 km wide by 1 km long (maximum SHARAD Fresnel zone), centered on SHARAD traces that overlap the DTMs; these DTM samples thus represent the surface that an individual SHARAD observation trace is reflective of. SHARAD observations that overlap with HiRISE DTMs are listed and summarized in Table 1.

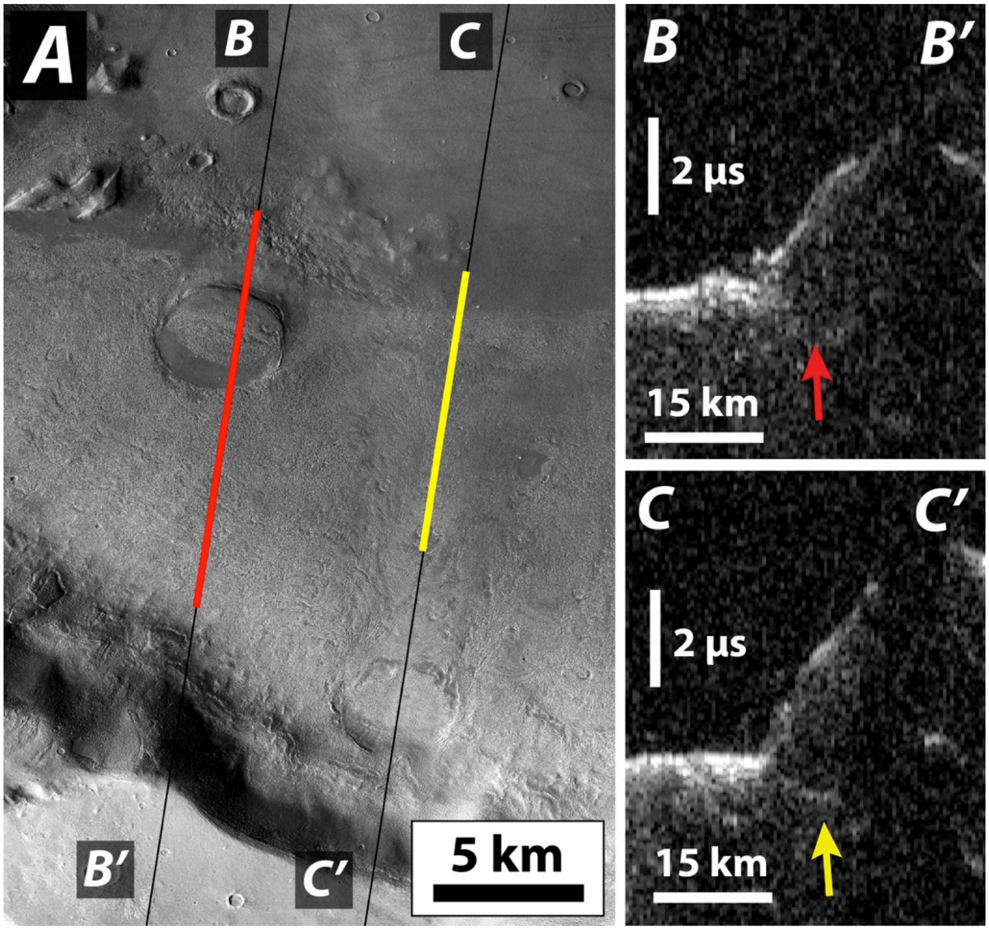

Figure 13: (A) Context camera (CTX) Image of lobate debris apron material which has flowed into the depression created by a crater; rough ejecta can be seen on the bedrock beyond the apron toe. (B) Observation in radar of a nonexistent or highly diffuse reflection between the apron and underlying bedrock (red arrow/line), possibly a result of the rough crater ejecta scattering the signal. (C) Observation in radar of strong basal reflector at sufficient distance from the subglacial crater.

For each SHARAD-trace DTM sample, we quantified surface roughness using fractal concepts, following the methods of Shepard & Campbell (1999). We used fractal methods because, as will be shown in the results, a single roughness parameter describing root-mean-square slope or height is not sufficient to describe the surface as it interacts with the radar.

Site	SHARAD Observation	# of Traces	Basal Detections	Basal Non-Detections
Site A	753802000	22	22	0
	3830801000	18	18	0
	--Site A Total--	40	40	0
Site B	3815601000	33	0	0
Site C	722102000	11	5	0
	865801000	36	3	0
	--Site C Total--	47	8	0
Site D	923802000	33	0	33
	3628301000	22	0	22
	3586101000	12	0	12
	--Site D Total--	67	0	67
Site E	2816001000	25	25	0
	3634201000	12	12	0
	1266602000	15	15	0
	--Site E Total--	52	52	0
----ALL TOTAL----		238	100	67

Table 1: List of SHARAD observations that overlapped with HiRISE DTMs at each of the sites. Also summarized is the number of traces (horizontal pixels in the radargram) and corresponding number of basal detections/non-detections that overlap with the DTMs.

There are many models that predict how surface roughness affects the reflection and transmission of an electromagnetic wave from a dielectric interface. Each of these models has their strengths and limitations. In the following text we introduce the standard method of calculating coherent signal loss and then present our chosen method of calculating coherent signal loss by employing a fractal model for rough surfaces, highlighting the differences between them.

Given a one-dimensional topographic profile for any surface, the mean elevation and slope must first be removed before surface roughness can be quantified. The most standard method of reporting surface roughness is the root-mean-square (rms) surface height h_0:

$$h_0 = \left[\frac{1}{N-1}\sum_{i=1}^{N}(z_i - \bar{z})^2\right]^{1/2} \tag{15}$$

Where N is the number of samples in the profile, z_i is the surface height at each sample, and $\bar{z}$ is the mean surface height (Campbell, 2002). The rms height h_0 is highly sensitive to the length of the profile over which it is measured. For instance, a profile several tens of centimeters long might exhibit roughness on the centimeters-scale (i.e. from sand ripples and pebbles) while a profile tens of meters long might exhibit roughness on the meters-scale (i.e. from hills and furrows) and a profile many kilometers long might exhibit roughness of up to hundreds of meters (i.e. mountains and canyons). Despite this fact, many studies assume "stationary surface," or one for which the roughness remains the same at scales relevant to the radar, and typically one value of h_0 is reported for the length scale equal to the relevant radar wavelength λ (Barrick & Peake, 1968; Campbell, 2002; Grima et al., 2012; Shepard & Campbell, 1999).

A coherent electromagnetic wave front is one in which the phases interfere constructively; as roughness increases the phases become increasingly randomized and interfere destructively in addition to being scattered in different directions. The sum of constructively interfering waves produces the coherent reflected power, while the sum of randomly scattered waves is described as the incoherent power (Campbell, 2002). The effect that a rough surface has on a reflected electromagnetic wave is therefore to reduce the ratio of coherent power to incoherent power.

The reduction in coherent reflection power for an electromagnetic wave incident on a rough stationary dielectric surface is most often often calculated as follows (Barrick & Peake, 1968; Ogilvy, 1991):

$$P_{rough} = \chi^2 P_{smooth} \tag{16}$$

$$\chi^2 = e^{-4k^2 h_{0\lambda}^2 cos^2\theta} \quad (17)$$

Where χ^2 is the roughness factor dependent on the radar wavenumber k, the rms height $h_{0\lambda}$ measured at the scale of the radar wavelength λ, and the incidence angle θ of the radio wave. This method of calculating coherent reflection power reduction may be inadequate for surfaces on which the surface roughness changes as a function of horizontal scale.

Two other less commonly used roughness parameters include the Allan variance υ^2 and root-mean-square (rms) slope s, which are calculated as a function of the difference Δx between points on the profile:

$$\upsilon^2(\Delta x) = \langle (z(x) - z(x + \Delta x))^2 \rangle \quad (18)$$

$$s(\Delta x) = \frac{\upsilon(\Delta x)}{\Delta x} = \frac{\sqrt{\langle (z(x) - z(x + \Delta x))^2 \rangle}}{\Delta x} \quad (19)$$

The Allan variance υ^2, also called the structure function, provides a measure of the distribution of squared height differences between points spaced a distance Δx along the profile. Its square root is called the Allan deviation υ, from which the rms slope $s(\Delta x)$ can be calculated. The advantage to using these roughness parameters is that they are independent of the length of the profile for which they calculated (Shepard & Campbell, 1999) and are explicit about the sensitivity of roughness to horizontal scale. Note that for a surface with Gaussian-distributed surface heights, the rms height can be found from the Allan deviation or the rms slope by the relation: $h_{0\lambda} = \frac{1}{\sqrt{2}}\upsilon_\lambda = \frac{\lambda}{\sqrt{2}}s_\lambda$ (Shepard & Campbell, 1999); this allows us to report what may be to some a more intuitive height value from the rms slope.

Fractal concepts provide a framework for quantifying the degree to which vertical roughness changes with horizontal scale (Shepard & Campbell, 1999). According to fractal theory all roughness parameters, including rms height, Allan deviation and slope scale as a function of horizontal scale in a power-law fashion dependent on the Hurst exponent H:

$$h_0(L) = h_{0\lambda}\left(\frac{L}{\lambda}\right)^H \tag{20}$$

$$\upsilon(\Delta x) = \upsilon_\lambda\left(\frac{\Delta x}{\lambda}\right)^H \tag{21}$$

$$s(\Delta x) = s_\lambda\left(\frac{\Delta x}{\lambda}\right)^{H-1} \tag{22}$$

The reference values $h_{0\lambda}$, υ_λ, and s_λ are the rms height, Allan deviation, and slope at the scale of the radar wavelength, λ = 15 m for SHARAD. H ranges between 0 and 1 and is an indicator of the degree to which roughness scales with horizontal scale. For a value of H = 0 the surface is stationary, as is assumed in Equation 17. For H = 0.5 the surface is essentially brownian noise, with increasing rms height and decreasing rms slope as scale is increased. H = 1 represents a surface for which the rms height increases in lockstep with horizontal scale while rms slope remains the same.[1]

Shepard & Campbell, 1999 show how the fractal surface model parameters can be used to calculate the reflected electric field *E* and power density *P* for the near-nadir regime by integrating over the surface using Huygens wavelet methodology:

[1]A visual example of how the Hurst exponent changes with the character of a rough surface is shown later in the results section of this chapter (Figure 16).

$$E = \frac{j\lambda}{Z} e^{-jkZ} 2\pi R E_0 \int_{\hat{r}=0}^{\infty} e^{-4\pi^2 s_\lambda^2 \hat{r}^{2H} cos^2\theta} \hat{r} J_0(4\pi\hat{r}sin\theta) d\hat{r} \quad (23)$$

$$P = \frac{\lambda^2}{2\eta Z^2} 4\pi^2 \rho E_0{}^2 \left[\int_{\hat{r}=0}^{\infty} e^{-4\pi^2 s_\lambda^2 \hat{r}^{2H} cos^2\theta} \hat{r} J_0(4\pi\hat{r}sin\theta) d\hat{r}\right]^2 \quad (24)$$

Where R is the assumed Fresnel reflection coefficient of the surface, ϱ is the resultant reflectivity, Z is the distance to the surface, $\hat{r} = r/\lambda$ is the scaled radius from the subnadir point, θ is the incidence angle, and J_0 is a zeroth-order bessel function of the first kind.

While the general case needs to be solved numerically, there are analytical solutions for the cases of a stationary surface (H = 0.0), a Brownian surface (H = 0.5) and a self-similar surface (H = 1.0). The stationary surface solution reduces to the coherent signal reduction equation shown in Equation 17.

The backscatter cross-section is a useful parameter in that it removes the need to define E_0 and Z, providing a purely theoretical value of the surface backscatter. The cross-section is defined as the ratio of the reflected power density to that of a perfect isotropic scatterer of the same area at the same distance under similar illumination. Such a scatterer exudes a power density of:

$$P_{iso} = \frac{\lambda^2 E_0^2}{(2\eta) 4\pi Z^2} \quad (25)$$

And the backscatter cross-section of a self-affine rough surface is thus as follows:

$$\sigma_0(s_\lambda, H, \theta) = 16\pi^3 \rho \left[\int_{\hat{r}=0}^{\infty} e^{-4\pi^2 s_\lambda^2 \hat{r}^{2H} cos^2\theta} \hat{r} J_0(4\pi\hat{r}sin\theta) d\hat{r}\right]^2 \quad (26)$$

From these analyses another useful parameter can be defined, which Shepard & Campbell (1999) suggest is a far more robust indicator of surface roughness than s_λ or the $h_{0\lambda}$. The effective aperture $\hat{r}_{eff}$ indicates the radius at which the coherent signal falls to 1%:

$$\hat{r}_{eff} = \left[\frac{5}{4\pi^2 s_\lambda^2 cos^2\theta}\right]^{1/2H} \tag{27}$$

The fractal surface backscattering model presented by Shepard & Campbell (1999) is only valid for the near-nadir scattering regime, and because it addresses only the coherent component of radar backscatter it is valid only for surfaces that are relatively smooth at the radar wavelength. As the roughness and thus incoherent power becomes sufficiently large, this model will more significantly underestimate the backscatter from rough surfaces.

We calculated $s(\Delta x)$ over a range of Δx = 15 - 300 m (Equation 19), representative of scales between the radar wavelength and the minimum Fresnel zone size. For each SHARAD trace DTM sample, this is done on all possible topographic profiles > 600 m in length and the results are averaged.

We fit the measured $s(\Delta x)$ to the power law shown in Equation 22 to constrain the Hurst exponent H for each DTM sample. We then calculated the backscatter cross-section and effective aperture of the surface represented by each DTM sample using Equations 26 and 27, respectively; we take the incidence angle $\theta = 0$ because this is a nadir radar sounder. Specifically, we used equation 26 to test if we can reproduce trends in measured surface reflection powers and equation 27 to test for correlation between surface roughness and the detectability of subsurface returns.

RESULTS

Non-detections of subsurface signals are in the minority in the Deuteronilus Mensae region, being observed in 13% of SHARAD traces over lobate debris aprons (where not obscured by clutter) (Figure 10). Non-detections are most abundant in eastern Deuteronilus Mensae and Protonilus Mensae, from Site C eastward. Non-detections in western Deuteronilus Mensae are few. In one case, a non-detection was mapped in correlation with a crater and ejecta blanket found partially beneath the toe of an apron (Figure 13). No similar evidence for sub-apron crater ejecta was found for any of the study sites examined in this work.

Study Sites A and B exhibited only detections of subsurface reflections. Site C exhibited subsurface reflections that faded out to the noise floor at a depth of roughly 1 km; non-detections were common where the apron thickness was inferred to be >1 km. Site C contains the only apron in this region inferred to be this thick, and the only one at which relatively bright reflectors disappear at depth. Site D is the only large apron system that exhibited no significant subsurface detections and only confirmed non-detections. Site E exhibited weak subsurface reflections on the cusp of the noise floor.

Because Site C is the only apron for which subsurface reflections fade out at depth, we scrutinized its attenuation values, both as calculated in Chapter 1 and by using methods employed by Holt et al. (2008). We extracted the loss tangents calculated in Chapter 1, assuming a surface dielectric constant of $\varepsilon'_{srf} = 3$ (yielding a maximum calculable loss tangent since this is the minimum ε'_{srf} expected) and calculated the resultant attenuation given an apron dielectric constant of $\varepsilon' = 3$ for four SHARAD observations of Site C. This resulted in a median attenuation value of 12.6 ± 4.6 dB/km, or a loss tangent of 0.0040 ± 0.0015 (Figure 14).

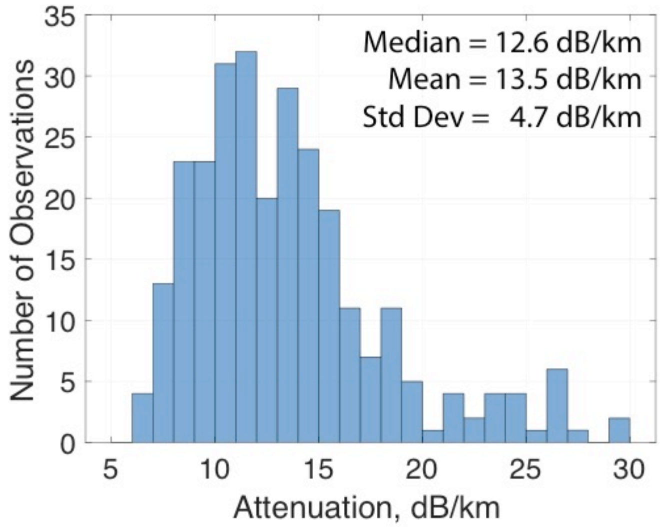

Figure 14: Histogram of attenuation values calculated using the methods described in Chapter 3 for each trace on the same SHARAD observations of Site C as shown in Figure 15. The median value is 12.6 ± 4.7 dB/km; 91% of values are < 20 dB/km. These values are also in agreement with those found by Holt et al. (2008).

We also calculated attenuation values using the method of Holt et al. (2008), by applying a linear regression of surface-normalized subsurface reflection power as a function of apron thickness (calculated from the measured delay time assuming a dielectric constant of ε' = 3) for each SHARAD track over the lobate debris apron in Site C. The slope returns the two-way attenuation in units of dB/km. Holt et al. (2008) reported attenuations of less than 20 dB/km, consistent with pure water ice. Using this method we calculated attenuation on the order of 4 to 16 dB/km (Figure 15), similar to the numbers found by Holt et al. (2008), and equivalent to loss tangents of 0.001 to 0.005.

Both these methods of estimating the attenuation in the lobate debris apron interior show that Site C is similar to all other aprons described in Chapter 1, and to other aprons previously described in the literature (Holt et al., 2008). We are unable to image the basal reflector at depth not because of increased attenuation but simply because of the great (> 1 km) thickness of the lobate debris apron, at which the total attenuation due to the travel time in ice reduces the reflected signal to below the noise floor of the radar. Because of this, we exclude the Site C non-detections from the surface roughness analysis.

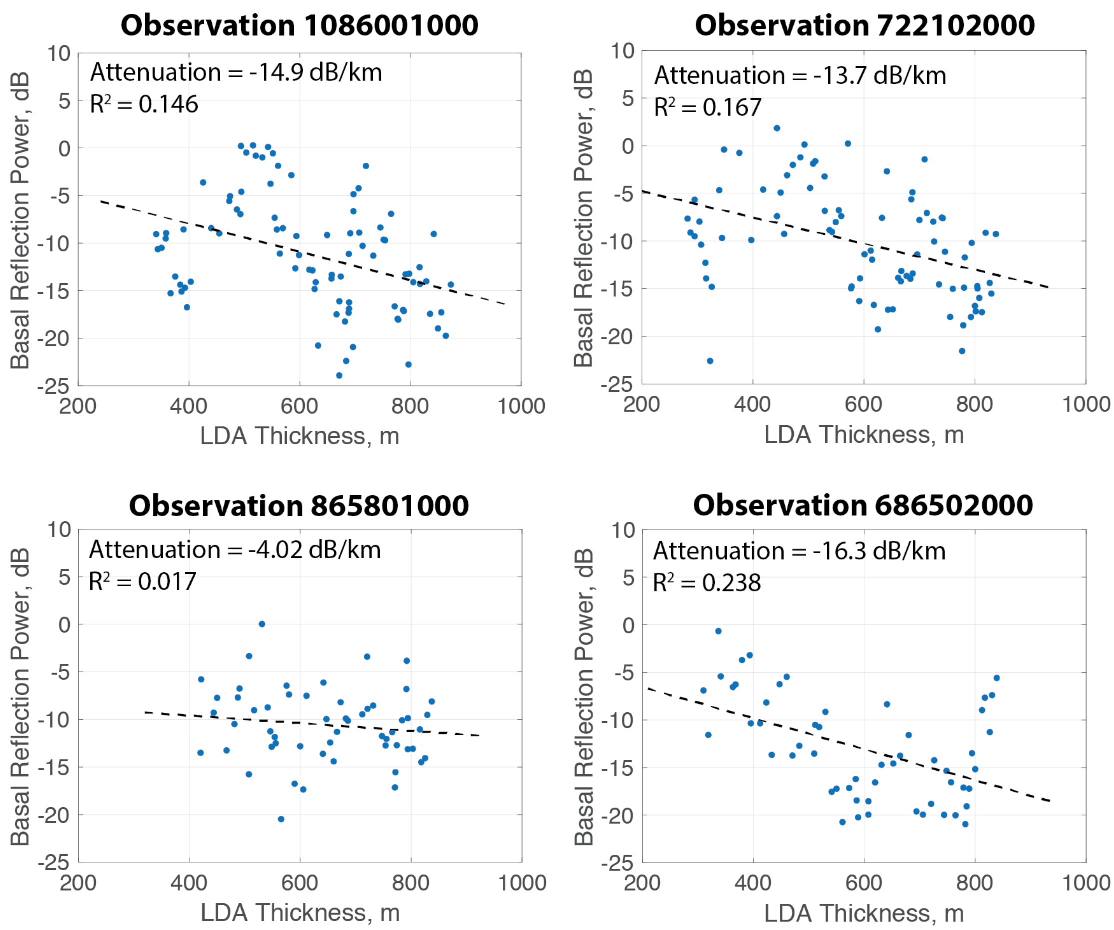

Figure 15: Linear regressions of basal reflection power as a function of lobate debris apron thickness for four SHARAD observations on Site C. All have low R^2 coefficients of determination and attenuation of less than 17 dB/km. These are similar to the values found in Holt et al. (2008).

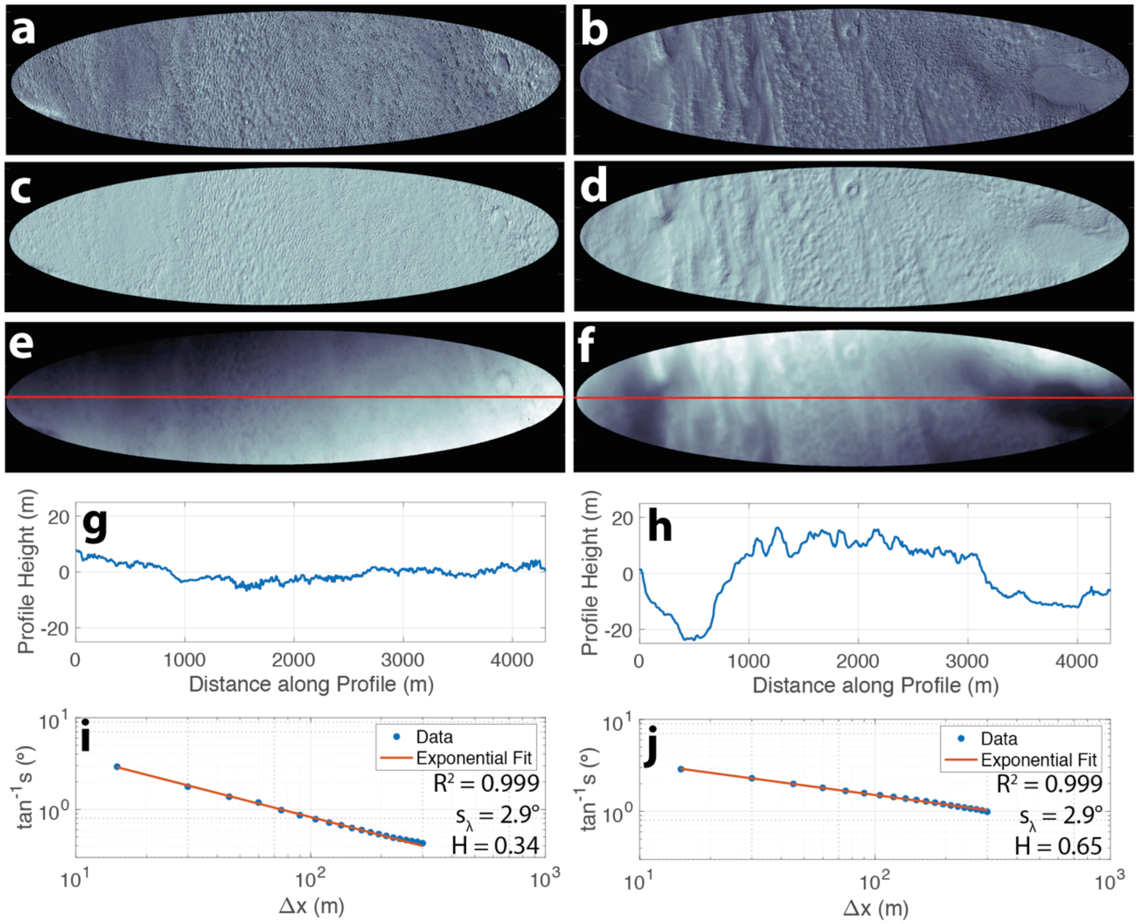

Figure 16: Representative SHARAD Trace DTM Samples for Site A (left column), associated with a basal detection, and Site D (right column), associated with a basal non-detection. (a,b) HiRISE image and (c,d) synthetic hillshade made from DTMs showing reproduction of morphology. (e,f) DTM elevation with example profile mapped in red. (g,h) Example detrended height profiles. (i,j) RMS Slope Fractal analysis. Note that while both profiles exhibit the same s_λ, the second one has a higher H value, leading to higher roughness at longer horizontal scales.

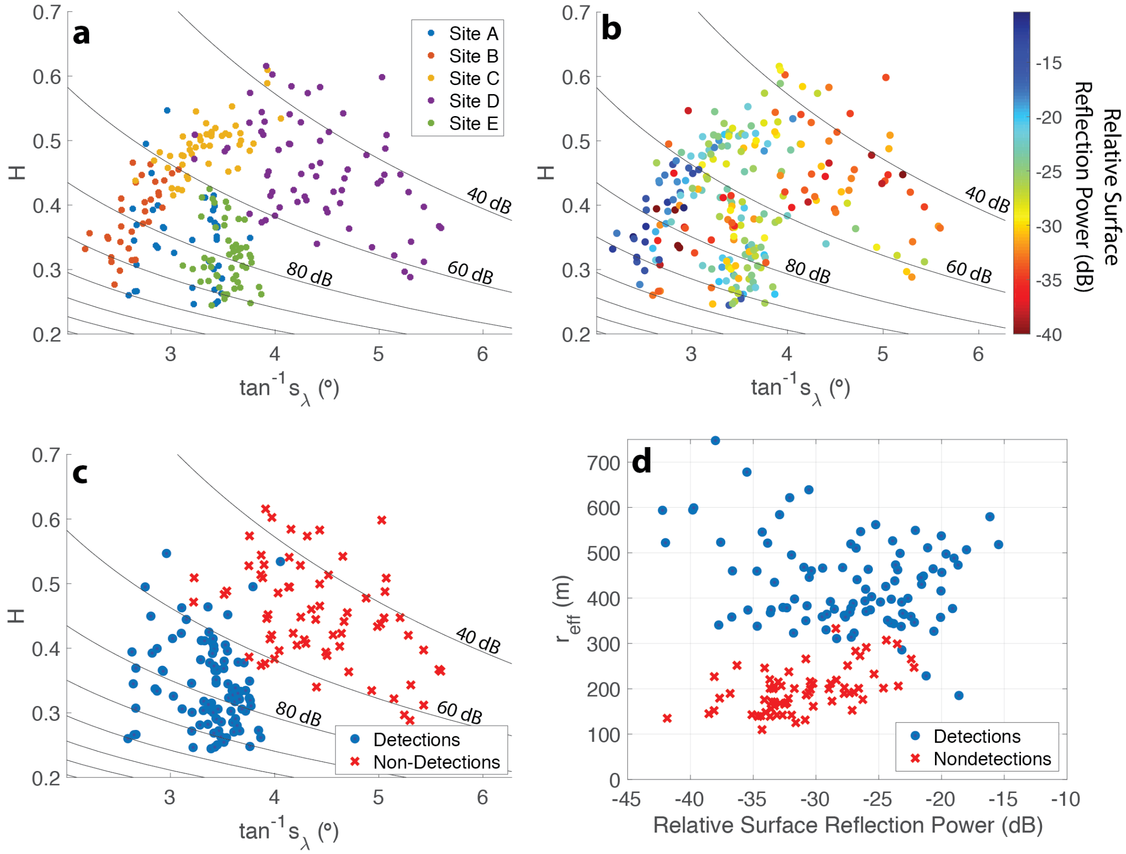

Figure 17: (a) H plotted against s_λ for each SHARAD trace; observations are colored by site. 20 dB contours indicate the theoretical backscattering cross-section σ_0, assuming incidence angle $\theta = 0°$ and reflectivity $\varrho = 0.15$ (corresponding to a surface of $\varepsilon' = 5$). (b) Same as (a), with observations color-coded by their observed relative reflection power; note the stronger reflection powers for smoother surfaces and weaker reflection powers generally at rougher surfaces. (c) Same as (a), with observations marked as basal detection or non-detection; note that non-detections are generally rougher in either s_λ or H than detections. (d) Effective radius $\hat{r}_{eff}$ plotted vs. reflection power for each SHARAD trace marked as detection or non-detection. Note the split at $\hat{r}_{eff}$ = 300m; only 2 non-detections are above $\hat{r}_{eff}$ = 300m and only 3 detections are below.

The HiRISE DTMs successfully reproduced surface morphology inferred from HiRISE images, including pitted terrains and surface lineations (Figure 16). The calculated $s(\Delta x)$ for each DTM sample was fit well by the power law in Equation 22, with all featuring coefficients of determination of $R^2 > 0.91$. Examples of fractal analysis of HiRISE DTM topography are shown in Figure 16. These examples show the physical effect of increased H when s_λ is held constant; the surface with a lower H value may reasonably be approximated as a stationary surface but the surface with a higher H value undulates more dramatically at longer wavelengths.

The results of those fits are plotted in Figure 17, along with a theoretical treatment for the backscatter coefficient σ_0 plotted as contours in the same parameter space, assuming $\varrho = 0.15$, consistent with the reflectivity from a surface of $\varepsilon' = 5$ (this value is unconstrained, but in any case can only change σ_0 by a constant value independent of H or s_λ - see equation 26).

There is a fair amount of variability in roughness values within each site, particularly for the Hurst exponent H. However, each site tends to occupy distinct yet overlapping regions in H vs s_λ parameter space (Figure 17a), with site B exhibiting the smoothest values and site D exhibiting the roughest values. We find that although generally there are higher surface reflection powers for the smoothest surfaces and lower surface reflection powers for the roughest surfaces, roughness alone does not determine surface reflection power; smooth surfaces at site A for example have low surface reflection power (Figures 17b, 18a). There is little correlation ($R^2 = 0.10$) between measured surface reflection power and the nadir backscatter coefficient associated with these surfaces (Figure 18a).

In contrast, roughness parameters correlate very well with the detectability of subsurface returns; while mapped detections are generally smoother, we found that non-detections typically have higher values of s_λ and/or H, which decreases σ_0 (Figure 17c). The effective aperture $\hat{r}_{eff}$, which takes into account both s_λ and H, tends to be < 300 m for non-detections and > 300 m for detections (Figure 17d). Similarly, the backscatter cross-section for surfaces associated with non-detections tends to be < 60 dB (Figure 18b).

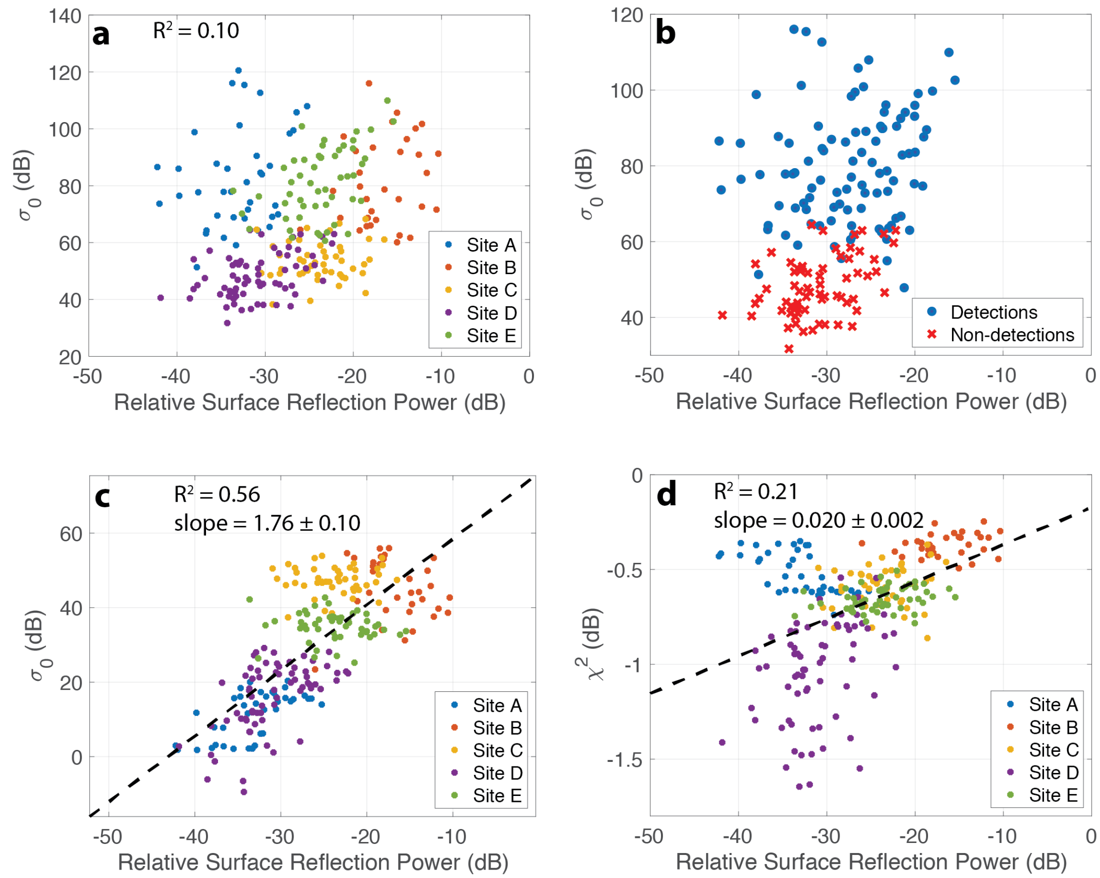

Figure 18: (a) Theoretical backscatter coefficient σ_0 plotted against measured relative surface reflection power for all observations at each site; they are poorly correlated with $R^2 = 0.10$. (b) Same as (a), with observations labeled as detection or non-detection; non-detections exhibit weaker back-scatter, generally < 60 dB. (c) Backscatter calculated with the radar incidence angle θ set to the MOLA slope for each observation; correlation is increased to $R^2 = 0.56$ and backscatter over-predicts reflection power by a factor of ~1.8. (d) Reduction in coherent reflection power predicted by model of a stationary surface; $R^2 = 0.21$ and the model under-predicts losses by a factor of 0.02.

Surface reflection power appears to be less dependent on surface roughness (Figures 17b, 18a) and correlates better with surface slope as constrained by MOLA (R^2 = 0.476, Figure 19a). Surface slope doesn't correlate with the detectability of subsurface returns; detections at site A typically have similar slopes to non-detections at site D (Figure 19). Interestingly, when the radar incidence angle θ is taken as the MOLA slope at each location, surface reflection power is more strongly correlated with the backscatter coefficient (R^2 = 0.56, Figure 18c) but over-predicts losses by a factor of ~1.8.

We also calculated the coherent reflection power loss predicted by a stationary surface roughness model and found poor correlation (R^2 = 0.21) and very small losses (< -2 dB) that can't account for the tens of dB variability in measured reflection powers (Figure 18d).

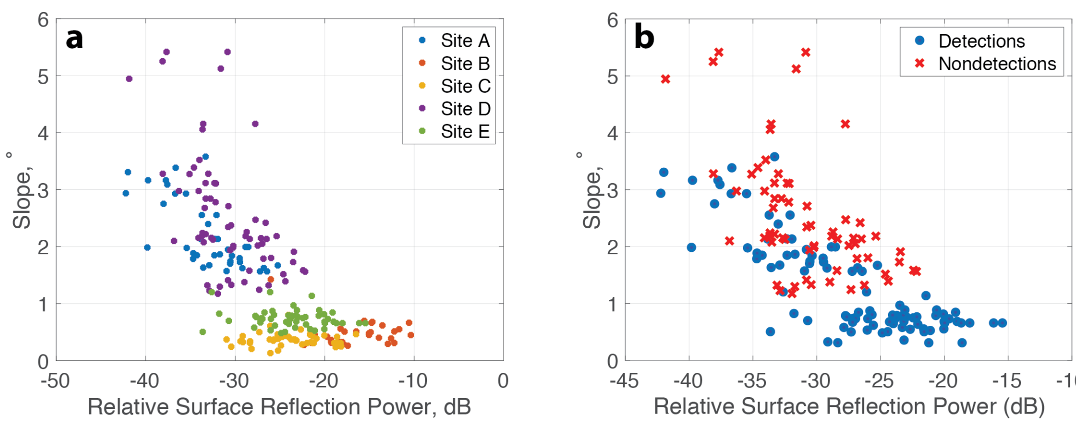

Figure 19: (a) Slope plotted against relative surface reflection power for each SHARAD trace used in the surface roughness analysis. They are correlated with R^2 = 0.476; higher slopes are associated with reduced surface reflection power. (b) Same as (a), with observations labeled as detections or non-detections. There is no correlation between detectability of subsurface returns and surface slope.

DISCUSSION

We find evidence that a number of factors affect the detectability of subsurface returns. In one isolated case, the presence of sub-apron crater ejecta appears to reduce subsurface signal return due to basal interface roughness (Figure 13). For one valley-filling apron in site C we find evidence that the > 1 km thickness of the apron reduces the basal reflection power to below the noise floor due to attenuation associated with pure water ice (Figures 3a-f, 12c, 14-15). We interpret this as roughly the maximum depth to which SHARAD can sound through lobate debris aprons that we interpret as debris-covered glaciers.

Aside from these cases, our analysis shows strong evidence for surface roughness as a major factor in modulating the detectability of subsurface returns. Surfaces associated with non-detection of subsurface signal are consistently rougher than surfaces associated with detections, having effective apertures of $\hat{r}_{eff}$ < 300 m (Figure 17d) and backscatter coefficients of σ_0 < 60 dB (Figure 18b). We interpret these values as indicating a cutoff at which point the coherent signal transmitted through the apron surface and returned to the spacecraft is below the effective noise floor of the SHARAD instrument, rendering detection of subsurface echoes impossible. We also acknowledge, however, that there will be an incoherent signal component not addressed by our model that will increase with surface roughness. The effect that this would have is to increase the total signal strength for rougher surfaces, widening the spacing between contours in Figure 17a-c. However, it would not change the general trend of total signal strength reduction for rougher surfaces, up to the complete extinction of the coherent component. Additionally, the incoherent component of a basal reflection may be too weak to be measured by SHARAD.

The model does poorly at predicting variance in surface reflection power (Figure 18a), which is correlated more strongly with long-wavelength surface slope (Figure 19). When MOLA surface slope is used as the radar incidence angle θ in equation 26, the model better predicts surface reflection power (Figure 18b). This would assume the primary signal return is from directly nadir. The model in this case over-predicts variance in reflection power by a factor of 1.76, which is likely a result of the fact that the method we employed only addresses the coherent component of the radar reflection. Thus our calculated backscattering coefficient is a minimum, especially for lower values.

This usage of the model as shown in Figure 18b is not particularly physical however, as the majority of the power returned to the radar sounder is from normal incidence at some distance from the direct sub-nadir point. As the surface slope increases this deviation from the sub-nadir also increases, reducing the radar gain dependent on the antenna radiation pattern. This effect is complicated by along-track Doppler focusing and the fact that the radar sounder may be more sensitive to across-track slopes. Due to the favorable geometry of these SHARAD observations over lobate debris aprons, across-track slopes are significantly lower than along-track slopes.

Overall, we find that surface reflection power is most dependent on surface slope and modulated to some degree by surface roughness, while the detectability of basal reflections is most dependent on surface roughness with no dependence on surface slope. We find two reasons for this effect. First, the effect of surface roughness scattering on the returned basal reflection is doubly important than it is for a surface reflection, due to the fact that the basal reflection travels through the surface twice. Second, because the basal interface is essentially flat the strongest contribution to its measured reflection may be from much closer to the sub-nadir point than it is for the surface reflection. The gain available for the basal reflection is not as dependent on surface slope and thus is not reduced to the same degree as it is for the surface reflection.

The treatment of lobate debris apron surface roughness as a fractal process was key to understanding its effect on radar sounding. Figure 16 illustrates how one surface roughness parameter, such as σ_h or s_λ, is insufficient to describe a natural surface such as our lobate debris aprons. Furthermore, if we were to treat our apron surfaces as stationary and used Equation 17 to calculate coherent signal loss, the result would have been losses of up to 1.65 dB, far less than the range of ~30 dB found in the data and the 60+ dB predicted by fractal analysis.

The higher roughness values and hurst exponents associated with Site D can be qualitatively linked to deeper sublimation pits/taller buttes, and prominent flow lineations observed in HiRISE. These morphologies are connected with a glacial origin, supporting the hypothesis that lobate debris aprons such as that represented by Site D are composed of pure water ice similar to their brethren. We are unable to confirm SHARAD imaging of their base because of signal reduction by surface roughness.

CONCLUSIONS

We find that within singular lobate debris aprons the detectability of subsurface returns can be locally controlled by basal interface roughness and apron thickness. On a regional scale however, we find that the roughness of the surface debris layer is sufficient to explain variability in SHARAD detectability of subsurface signals for entire lobate debris aprons. This work highlights the importance of surface roughness to radar sounding of geologic targets and the validity of fractal concepts in describing natural surfaces such as those of lobate debris aprons. It also illustrates that there is no need to invoke an ice-poor composition for lobate debris aprons that SHARAD can't penetrate, and that the simplest model is that they are all ice-rich debris-covered glaciers. The water ice volume estimate presented at the end of the previous chapter is thus a lower limit for the total budget available in Deuteronilus and Protonilus Mensae.

A RADAR SURVEY OF A TERRESTRIAL ROCK GLACIER

Chapter 5: New Insights Into Ice Accumulation at Galena Creek Rock Glacier from Radar Imaging of its Internal Structure

INTRODUCTION

Galena Creek Rock Glacier is a site of great importance to the rock glacier scientific literature, being a touchstone in the historical debate around rock glacier origins (Potter Jr et al., 1998). Rock glaciers are found in alpine and polar environments and are defined by a surface of talus debris that exhibits morphologic evidence for viscous flow. This can include an over-steepened toe (often at the angle of repose of the debris), flow-parallel lineations/boulder trains similar to medial moraines, and transverse ridges (Capps, 1910; Wahrhaftig & Cox, 1959).

Models of rock glacier formation generally fell into two camps: those which maintained many rock glaciers to be cored with snowfall-derived glacial ice (Potter, 1972) and those which maintained rock glaciers to be exclusively periglacial features with interstitial ice sourced from refreezing of meteoric water and snow/ice melt (Barsch, 1987). To date there is ample evidence for glacial ice-cored rock glaciers while periglacial processes may still play some role (Clark et al., 1998).

An example is the seminal study of Galena Creek Rock Glacier by Potter (1972), who used exposure observations and seismic profiling to show that the glacier in the upper two-thirds of the valley is cored by 88-90% purity sedimentary ice under a surface debris layer 1-1.5 m thick.

Because rock glaciers can preserve large quantities of ice they are of interest as elements in alpine and polar hydrological systems (Rangecroft et al., 2015) and as unique records of climate history (Steig, Clark, et al., 1998). Rock glaciers also receive attention from the planetary science community as analogs to martian landforms with similar with similar morphology (Holt et al., 2008; Mahaney et al., 2007; Squyres, 1978).

Potter (1972) used observations of snowfield depth and debris fall at Galena Creek Rock Glacier to hypothesize that ice is formed by accumulation of wind-blown snow in a narrow accumulation zone at the base of cirque headwalls. The ice is then preserved by debris fall coming to rest on the snow surface at the end of the accumulation zone, leaving little debris to be entrained in the glacier ice.

The steady-state model presented by Potter (1972) stands in contrast to a debris-covered glacier model developed by Mackay et al. (2014). In MacKay's model the bulk of the ice is deposited during periods of net positive ice accumulation while the glacier-wide surface debris lag is formed during periods of net ablation. This model leads to the possibility of buried debris layers that may reflect ice accumulation cycles and thus climate history.

Motivated by constraining ice and debris accumulation history at Galena Creek Rock Glacier we present a ground-penetrating radar survey at the site to image the rock glacier's internal structure. Specifically, we tested for the validity of Potter's accumulation model and searched for possible structural climate signals.

SITE

Galena Creek Rock Glacier is located in a north-facing valley in the Absaroka Mountains of northern Wyoming. It is 240-300 m wide and stretches 1.6 km from the cirque at an elevation of 3100 m to its toe at an elevation of 2700 m. The rock glacier is

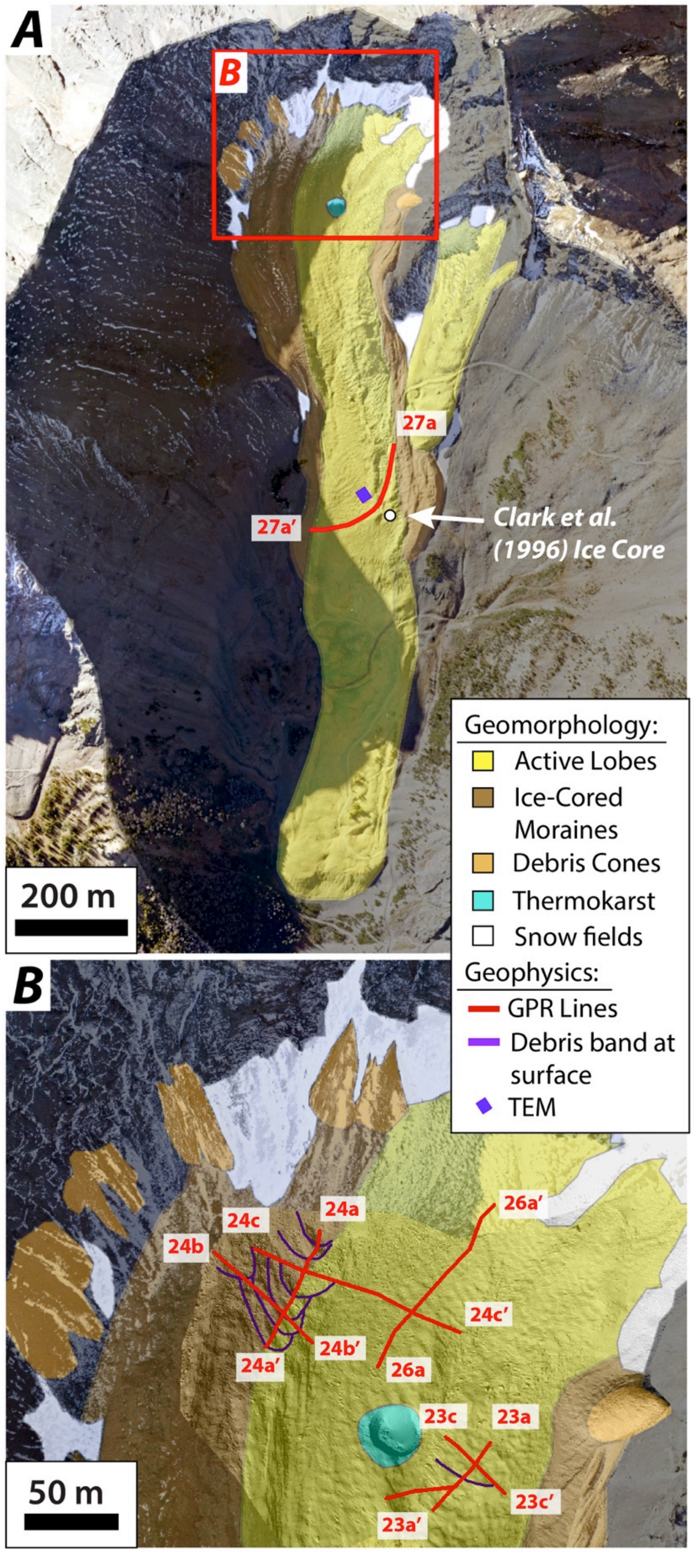

Figure 20: (Caption on following page)

Figure 20: (Previous page) (A) Orthorectified airborne image of Galena Creek Rock Glacier overlain by geomorphic mapping based on the work of Ackert, Jr. (1998); the location of the ice core of Clark et al. (1996) and the radargram in Figure 27 are also mapped. (B) Zoom on the cirque showing the location of the thermokarst pond and the radargrams shown in Figures 23-26. Mapped in purple is an interpretation of where strong dipping reflectors in GPR data intersect the surface. North is to the bottom of the page.

composed of a core of pure glacial ice in the upper two-thirds of the valley, while the lower third contains only an ice-rock mixture (Potter Jr et al., 1998; Potter, 1972). The surface debris layer has been measured at 1-1.5 m for the upper section and 2-3 m for the lower section (Potter, 1972). Ice has successfully been cored down to 9.5 m depth in the upper section (Clark et al., 1996).

Potter Jr et al. (1998) measured surface velocities by surveying surface boulder displacement over a period of 28-32 years and found that typical velocities range between 16-45 cm/yr, with a maximum of 80 cm/yr observed on the steep slope below the cirque. Seismic refraction surveys by Potter Jr et al. (1998) inferred the basal contact between glacier ice and bedrock to be at depths of up to 20-25 m. Based on a comparison between this glacial thickness and glen's flow law (Nye, 1957), Potter Jr et al. (1998) inferred that up to half of the glacier velocity may be attributable to basal sliding.

The bedrock geology in the locale of Galena Creek Rock Glacier is defined by the Wapiti Formation, which is composed of dark andesitic volcaniclastic rocks consisting entirely of vent facies (Smedes & Prostka, 1972). There are also numerous lighter-colored dikes and intrusions. The debris cover of Galena Creek Rock Glacier is composed of andesitic boulders eroded from bedrock in the headwall.

METHODS

We surveyed with ground-penetrating radar (GPR) at 50 MHz and 100 MHz using a Sensors and Software PulseEKKO Pro system. Over two field seasons in August

2015 and August 2016 we collected 12 reflection surveys and 1 common-midpoint survey. Radar profiles are numbered by the year and order of acquisition, i.e. #2016-1. The common-midpoint survey and 8 reflection surveys were obtained in the cirque, while the 3 remaining reflection surveys were obtained in the middle section of the glacier. GPR surveys are mapped across the surface of the rock glacier in Figure 20. Diffraction hyperbolae were fit to each of the reflectors observed in the common-midpoint survey to determine the radio wave velocity as a function of depth. Each of the reflection surveys were then migrated and corrected to depth using the determined radio wave velocity. Topographic data with a resolution of 27 cm/px was produced by airborne photogrammetry and applied to GPR data.

We additionally acquired 28 Transient Electromagnetic (TEM) Soundings in August 2015 to constrain the thickness of Galena Creek Rock Glacier. TEM is a method that takes advantage of the principle of electromagnetic induction. A wire loop, in our case 20 m x 20 m square, is laid upon the surface and a current is run through it to produce a magnetic field. The current is then stopped, removing the magnetic field and inducing decaying eddy currents in the subsurface, the strength of which are directly correlated with the conductivity of the subsurface. These eddy currents induce a voltage in the wire loop, which is recorded by the TEM equipment. That voltage decay curve can then be used to infer the conductivity structure of the subsurface. Iterative forward modeling is initiated based upon a prior model of the subsurface, in our case a three layer model of surface debris, resistive rock glacier ice, and bedrock, and allowed to converge on a solution that predicts the voltage decay curve observed by the instrument. We used a TerraTEM system.

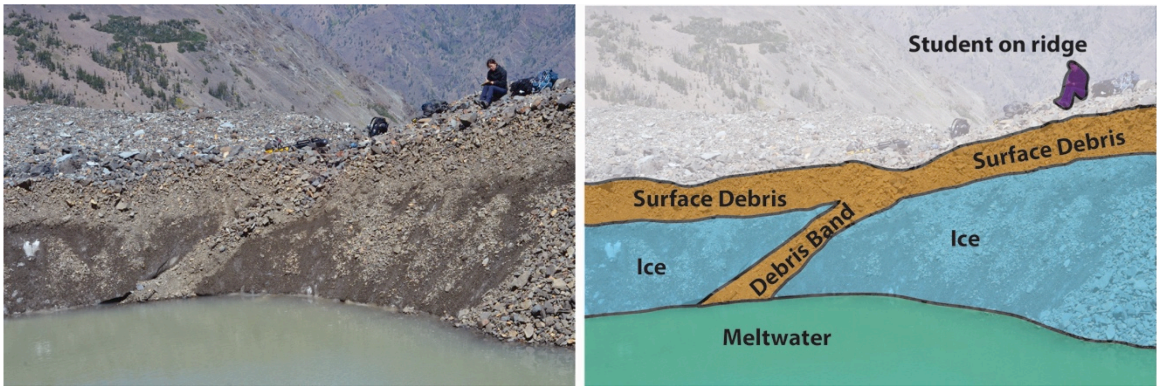

Figure 21: Image and interpretation of the thermokarst exposure displaying the surface debris layer and an englacial debris band.

RESULTS

Observations were made in August 2015 of a 40 m wide thermokarst pond exposing the upper 4-5 m of rock glacier stratigraphy in the cirque (Figure 21). A dry surface debris layer 1-1.5 m thick was observed overlying glacial ice. As the ice melted throughout the day, surface debris wasted down the ice surface to soil it. We observed in the thermokarst exposure a debris band extending from the surface debris layer into the subsurface, approximately 50 cm thick and dipping towards the cirque headwall at an apparent dip of 30°. The debris band also intersected the surface debris layer near a subtle ridge resolved in the photogrammetric DTM.

The common midpoint GPR survey (Figure 22, profile #2016-8) imaged numerous reflectors at time delays of up to 650 ns, of which we fit diffraction hyperbolae to 15 to solve for the radio wave speed. The shallowest reflector yielded a velocity of 0.116 m/ns (dielectric constant of $\varepsilon' = 6.69$); the remainder of the reflectors produced a range of velocities between 0.15 and 0.17 m/ns, with a mean value of 0.156 ± 0.014 m/ns ($\varepsilon' = 3.70 \pm 0.33$). We used this value for migrating and depth-converting reflection survey radargrams.

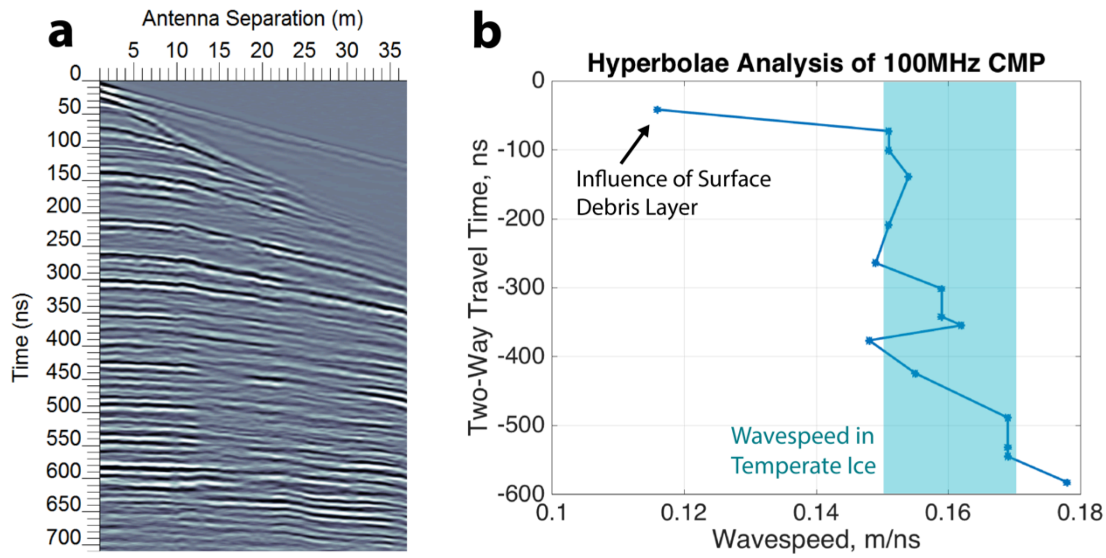

Figure 22: Common midpoint survey (profile #2016-8) to determine radio wave speed in the subsurface. (a) Common midpoint radargram. (b) Common mid-point velocities resulting from hyperbolae analysis. Mean velocity = 0.156 m/ns, a value typical for temperate glacial ice.

Radar data obtained near the thermokarst pond is shown in Figure 23 (Profiles #2016-6 and #2016-7). At 100 MHz we resolved at least four reflectors of moderate reflection strength that dip up-glacier at 20-25° and extend semi-continuously up to 30 m into the subsurface. In the flow-transverse direction they appear to be broadly concave-up. The 50 MHz antennas were for the most part unable to detect the reflectors. A flat, strong reflector was also imaged at ~40 m depth.

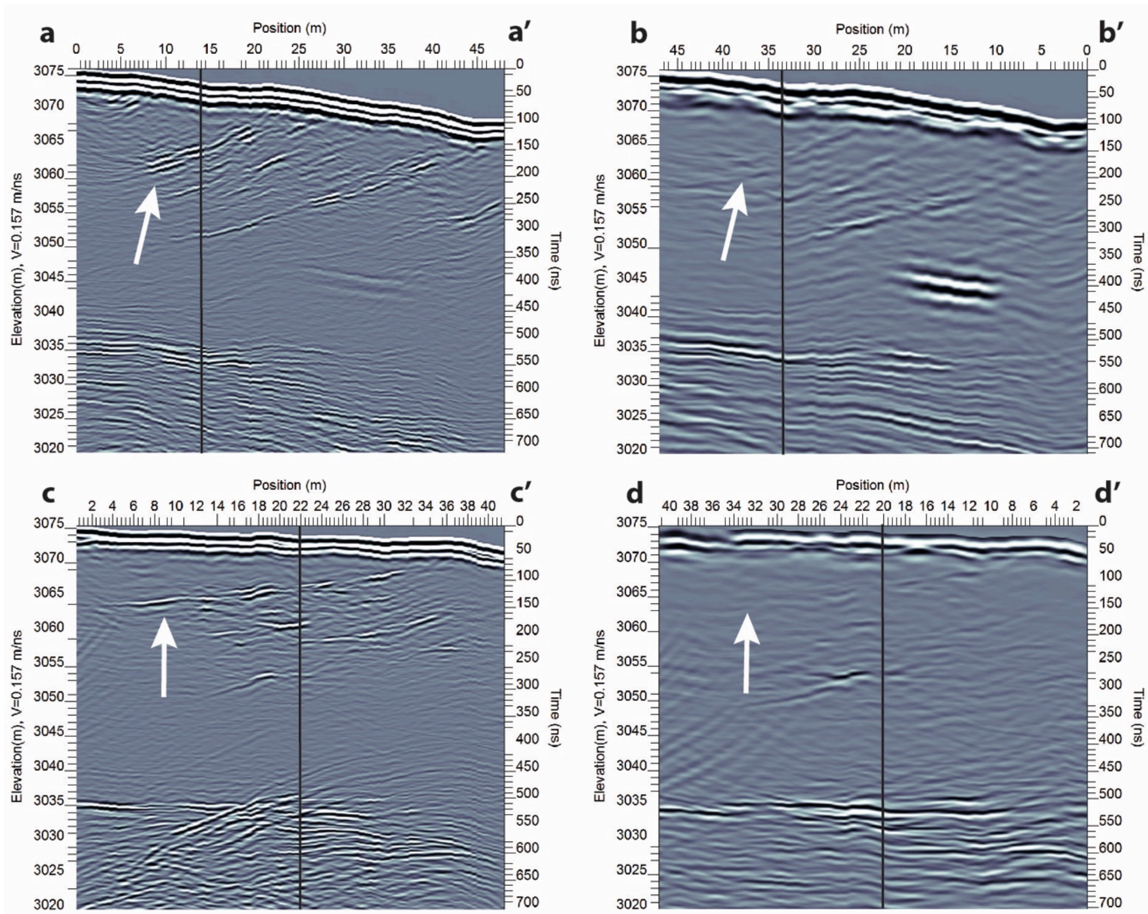

Figure 23: Radargrams near the thermokarst pond. (a-a') Profile #2016-6 acquired at 100 MHz in the along-flow direction displaying several dipping reflectors (white arrow). (b-b') 50 MHz data also along profile #2016-6; note that many of the dipping reflectors effectively disappear in the 50 MHz data. (c-c') Profile #2016-7 acquired at 100 MHz in the flow-transverse direction with several reflectors imaged; one indicated by arrow has a partial concave-up shape. (d-d') 50 MHz data also along profile #2016-7; again, many of the reflectors disappear. The black lines in each panel indicate the point where the longitudinal and transverse profiles intersect. The possible base of the glacier is imaged in both 50 MHz radargrams at ~40 m depth, or 3035 m elevation.

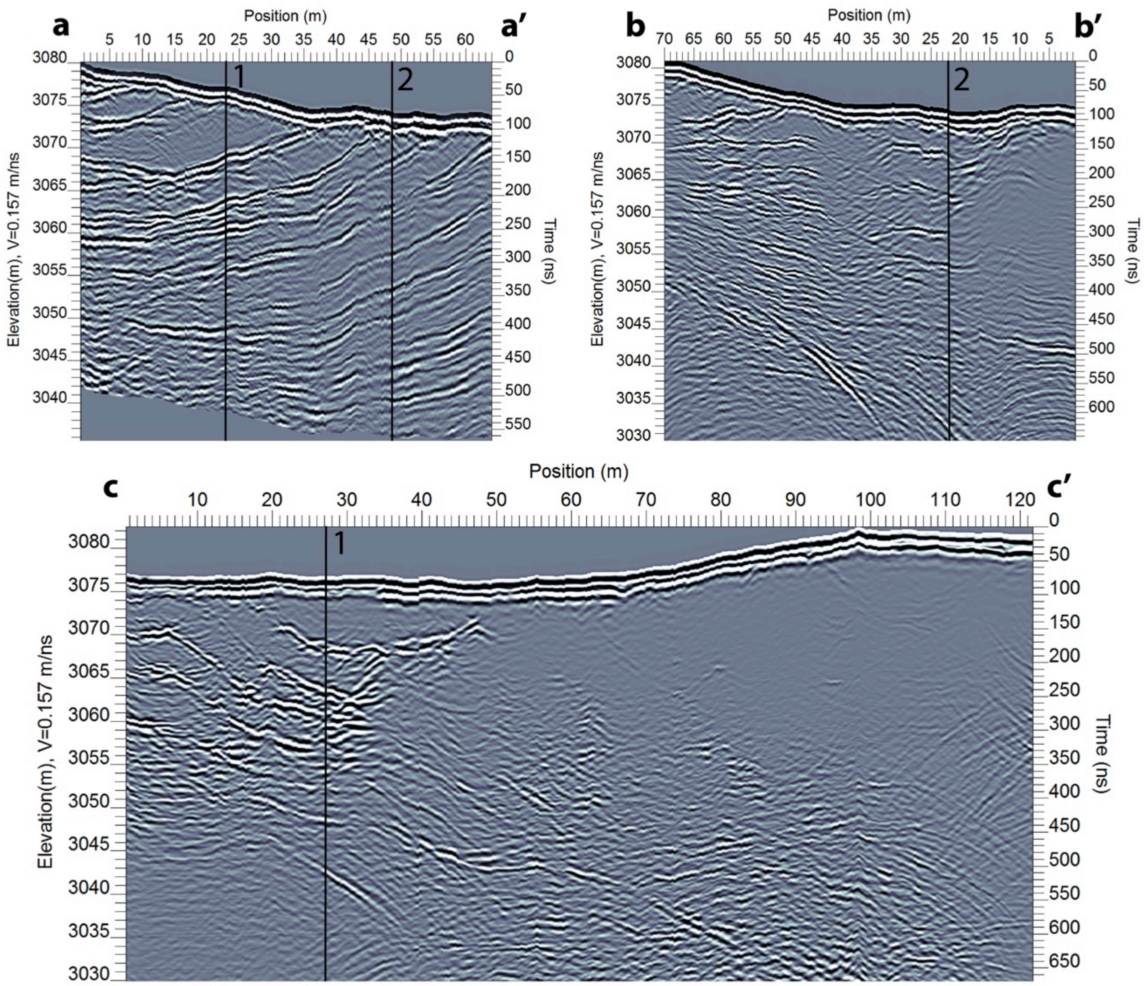

Figure 24: 100 MHz radargrams acquired on the east side of the cirque. (a-a') Flow-parallel profile #2015-3 displaying numerous (>6) strong up-glacier dipping reflectors. (b-b') Flow-transverse profile #2016-5 displaying complex, broken geometry of reflectors. (c-c') Flow-transverse profile #2016-4 that extends into the center glacier, illustrating how localized the reflector set is; the main glacier body is for the most part reflection-free. In this view we see the reflectors are concave-up, forming a tight nested-spoons geometry. Numbered black lines in each panel indicate the point of intersection between transects.

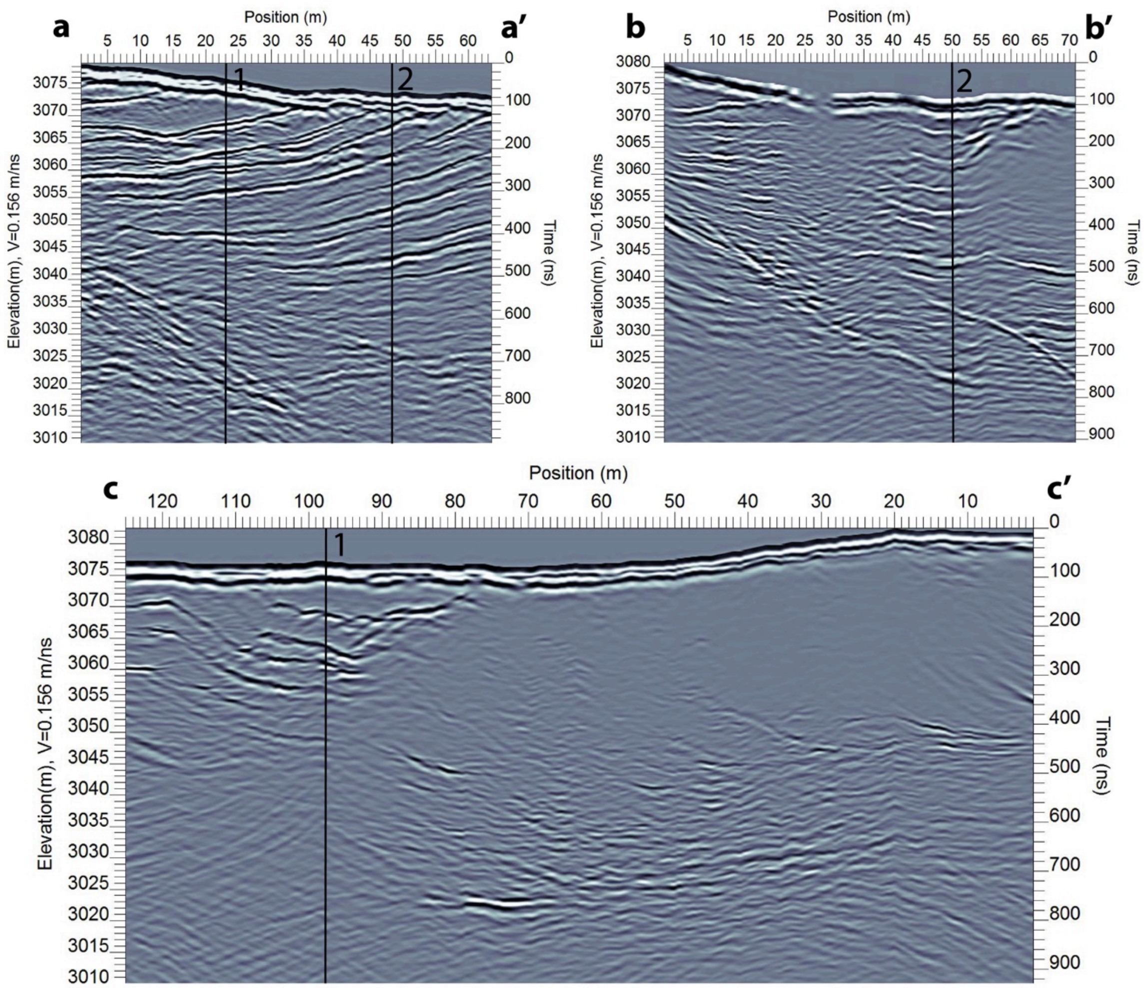

Figure 25: 50 MHz radargrams acquired on the east side of the cirque, showing that the same reflections are seen at both frequencies. (a-a') Flow-parallel profile #2015-3 displaying numerous (>6) strong up-glacier dipping reflectors. (b-b') Flow-transverse profile #2016-5 displaying complex, broken geometry of reflectors. (c-c') Flow-transverse profile #2016-4 that extends into the center glacier, illustrating how localized the reflector set is; the main glacier body is for the most part reflection-free. In this view we see the reflectors are concave-up, forming a tight nested-spoons geometry. Numbered black lines in each panel indicate the point of intersection between transects.

Radar data obtained in the eastern portion of cirque displayed strong, continuous reflectors at depth that resemble a network of nested spoons (Figure 24, profiles #2015-3, #2016-4, and #2016-5). Similar to the reflectors at the other end of the cirque, these intersect the surface at up-glacier dips of 25-35°. However, these are more numerous (11+ reflectors), continuous, intersect the surface near flow-transverse topographic ridges, fully enclose the ice into stratigraphic units, and are strong in 50 MHz data as well as 100 MHz (Figure 25). The ice units enclosed by the reflectors are typically 2-4 m in thickness, with the largest being up to 6-7 m thick. While the architecture of the reflectors appears similar to nested spoons, there is some complexity including bifurcating reflectors, ice units not in contact with the surface debris layer, and overlapping or disconnected ice units.

The contrast between the complex of reflectors in the east cirque vs. the relatively featureless center glacier body can be seen in Figure 24c and 25c. A 110 m long flow-parallel radar profile taken down the center of the glacier in the cirque is shown in Figure 26, profile #2016-3. Shallow weak dipping reflectors are observed in 100 MHz but are barely visible in 50 MHz. A strong reflector extends from depths of ~28 m at the up-glacier extreme of the profile to depths of ~55 m where it fades to the noise floor.

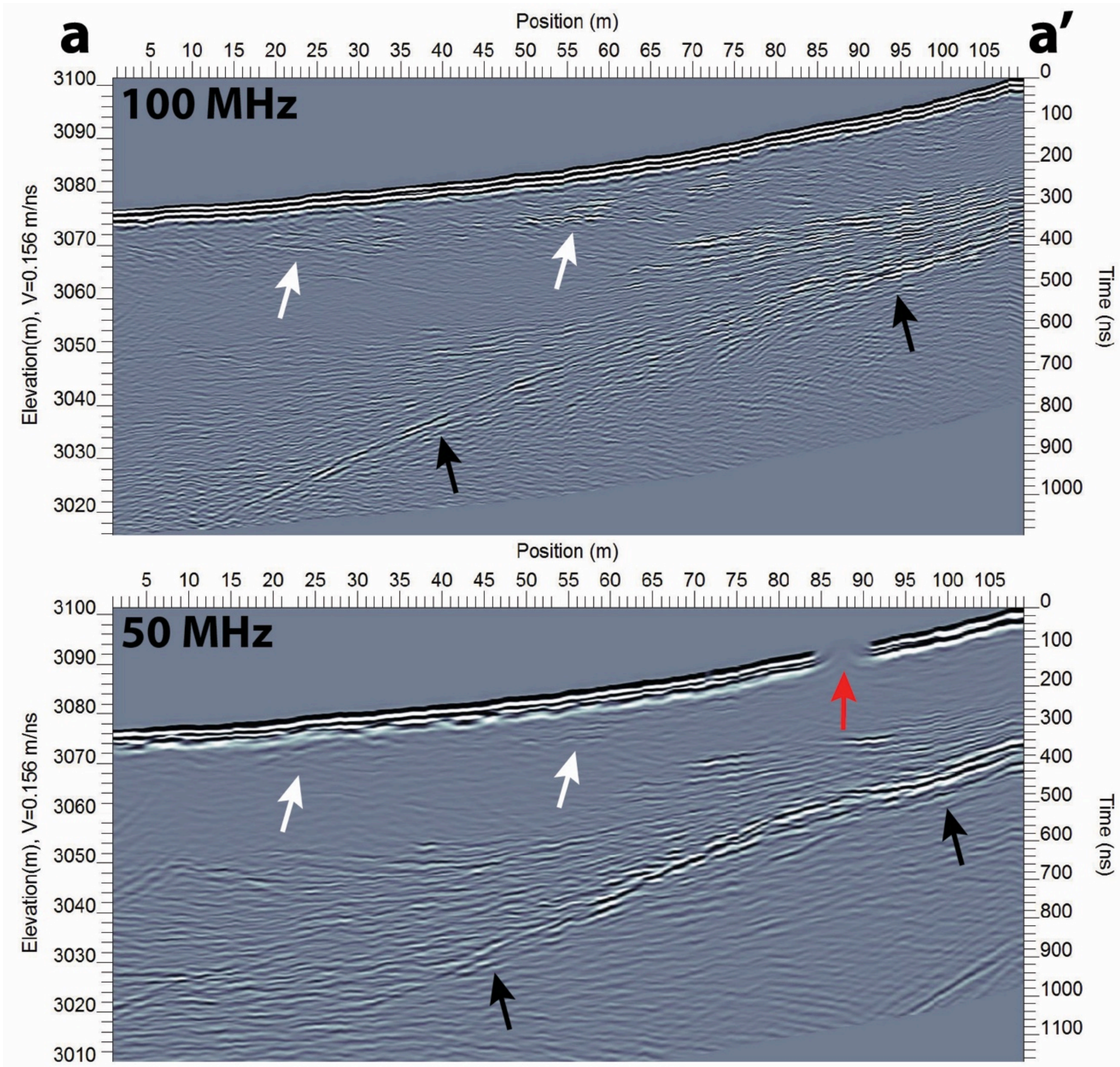

Figure 26: Flow-parallel profile #2016-3 acquired at 100 MHz and 50 MHz in the center of Galena Creek Rock Glacier, high in the cirque (location mapped in Figure 20). White arrows indicate faint dipping reflectors similar to those seen in Figure 23 that are imaged well in 100 MHz and poorly at 50 MHz. Black arrows indicate a reflector at depth interpreted as the base of Galena Creek Rock Glacier. Red arrow indicates missing data in the 50 MHz profile, a result of radar transmitter power loss while acquiring data.

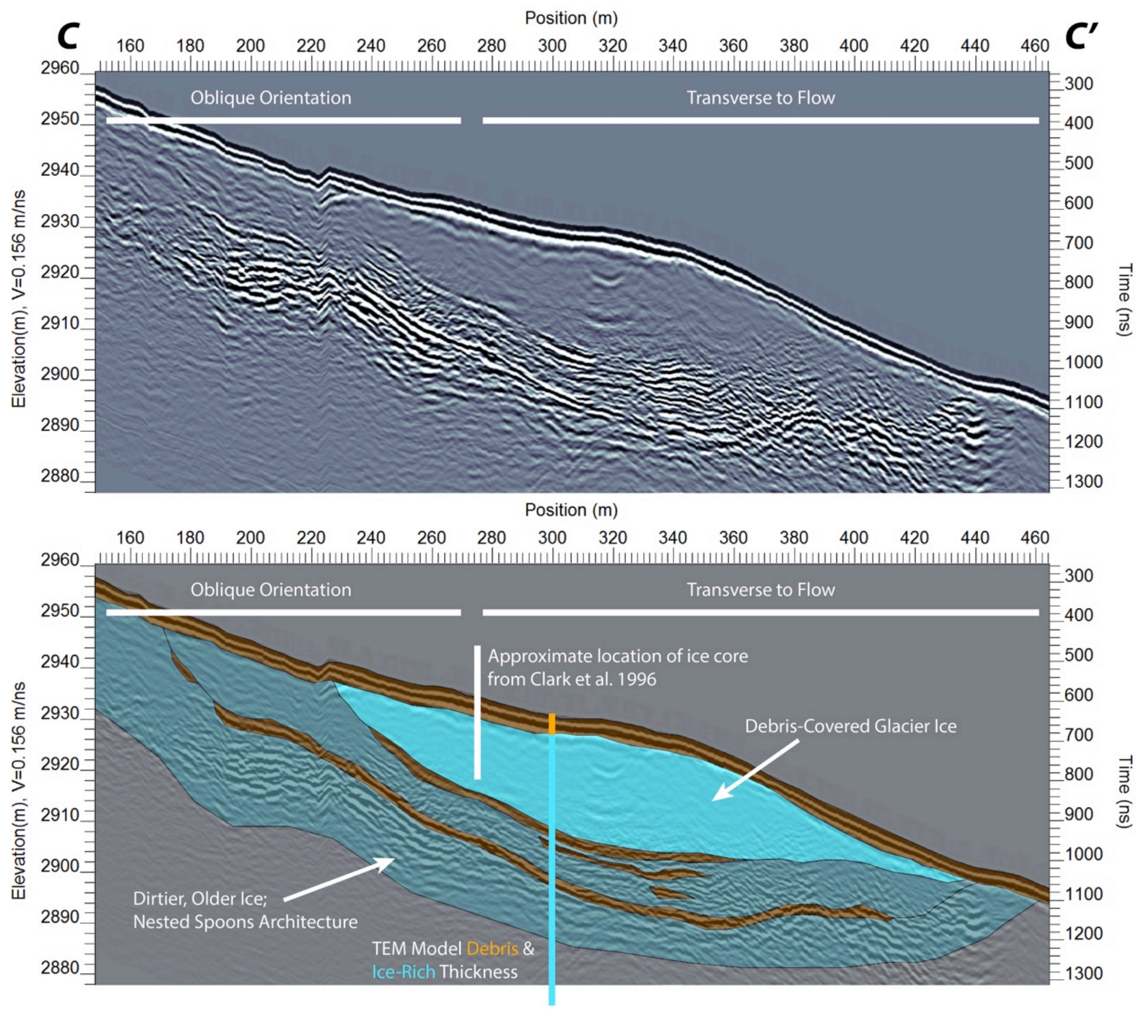

Figure 27: Mid-glacier radargram (profile #2015-1) with overplotted interpretation. The reflection-free zone down to about 20-25 m depth is interpreted as the clean ice core. The deeper zone which extends 25-35 m in depth we interpret as a dirty ice-debris mixture. The reflector at 35 m depth may or may not be the bedrock contact. A nearby TEM sounding (Figure 28a) additionally provided an estimate of the glacier thickness at 55 m.

We made use of the road crossing the middle section of Galena Creek Rock Glacier to obtain a radargram across the full width of the glacier (Figure 27). We observed a zone with very little scattering or reflectors down to a depth of 20-25 m, where there is a strong concave-up reflector. Beneath that there is a zone with increased scattering and another strong concave-up reflector at 35 m depth, beneath which the scattering continues until it fades to noise at about 45 m depth.

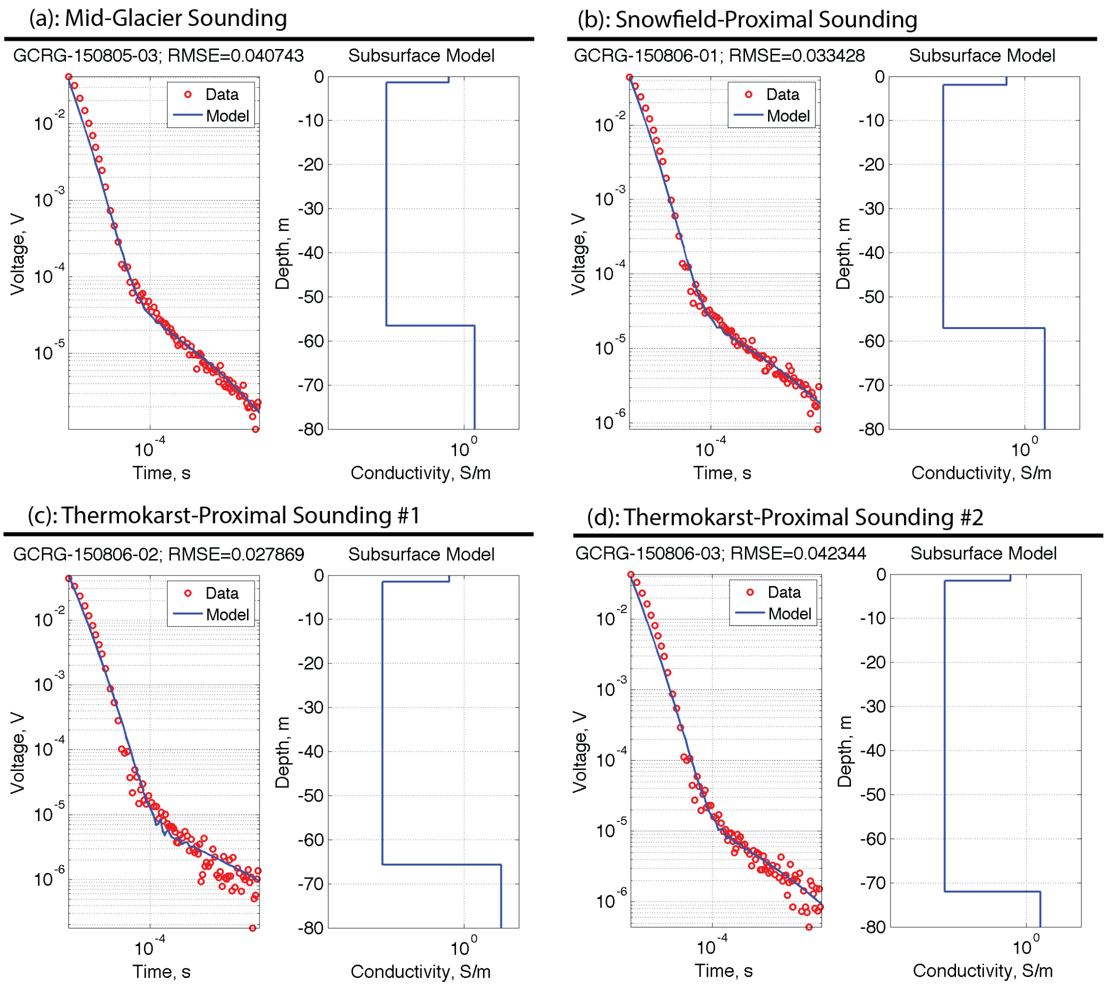

Figure 28: Examples of Transient Electromagnetic (TEM) sounding data and inverted conductivity models of the subsurface. For each sounding, the left panel is the voltage decay curve as a function of time. The right panel is a 3-layer subsurface conductivity model. The 1-2 m thick top layer with moderate conductivity is interpreted as the surface debris layer, the highly resistive ~55-70 m thick middle layer is interpreted as the total rock glacier thickness, and the highly conductive basement layer as the bedrock contact.

Examples of TEM sounding decay curves and conductivity models are shown in Figure 28. All soundings were fit well by a three-layer model, typically with a surface layer of 3.7 ± 0.2 Ωm, a middle layer of 970 ± 60 Ωm, and a basement of 0.18 ± 0.15 Ωm. TEM soundings locally constrained the bulk total thickness of Galena Creek Rock Glacier to 26 - 75 m. The mean thickness was revealed as 60 ± 14 m. A TEM sounding obtained near the mid-glacier GPR transect #2015-1 constrained the glacier thickness to be ~55 m thick, greater than the maximum depth that the GPR was able to image.

DISCUSSION

The velocities found by the common midpoint at depth are consistent with high purity glacier ice. Ice in the near-freezing temperature regime has a dielectric constant of 3.1-3.2 (Evans, 1965; Gough, 1972; Johari, 1976). If we assume the andesitic debris has a dielectric constant of ε' = 8 similar to basalt or granite (Reynolds, 1997) and use the Maxwell-Garnett Mixing Formula (Sihvola, 1999) we find based on our measured velocities an ice purity of 80-95%, consistent with Potter (1972)'s observed value of 88-90%. The low velocity/high dielectric constant of ε' = 6.7 found for the first reflector is consistent with higher debris content associated with the surface debris layer.

We interpret the dipping GPR reflectors found at depth in the cirque to be englacial debris bands by analogy to the debris band observed in the thermokarst exposure. The reflectors dip up-glacier at similar angles to that of the debris band, and their radar properties are consistent with a similar layer thickness. The fact the reflectors near the pond are imaged well in 100 MHz and poorly at 50 MHz indicates that they are of a thickness range below the resolution of the 50 MHz and within the resolution range of the 100 MHz. At our prescribed velocity of v = 0.156 ± 0.014 m/ns the theoretical radar resolution λ/4 is 39 ± 2 cm for 100 MHz and 78 ± 3 cm for 50 MHz. The reflectors are thus 37-75 cm in thickness, similar to the 50 cm thickness of the debris band exposed by thermokarst. The reflectors forming a complex in the eastern side are, by the same reasoning, likely at least 75 cm thick as they are seen clearly in both 50 and 100 MHz data.

Our observations of the relatively clean ice core with intermittent discontinuous debris bands are broadly consistent with Potter (1972)'s model of ice accumulation in the narrow snowfield below the northeast-facing walls of the cirque, with the majority of small-scale debris fall coming to rest on the rock glacier surface at the end of the accumulation zone to form the surface debris layer. We hypothesize that the englacial debris bands were produced by large debris fall events that cover the snowfield and are then subsequently buried by snow/ice accumulation. This is supported by observations by Potter (1972) of a large debris fall that occurred in early spring 1966 and covered 11,000 m^2 of the snowfield and glacier surface with an average 20 cm thickness of debris - this happened to account for two-thirds of the total debris fall observed that year. Areas of the glacier that experience much higher net ice accumulation than debris fall appear relatively clean (center glacier, Figure 26) or with small, discontinuous debris bands (cirque near thermokarst, Figure 23), while areas with more significant debris fall develop extensive buried debris bands.

A situation with relatively high debris fall and low ice accumulation may lead to an interesting effect, particularly when large debris falls occur early in the spring season. We present a new model for debris and ice accumulation in rock glaciers that we term "debris-facilitated ice accumulation" (Figure 29). The cirque snowfield accumulates each winter season from precipitation and wind-packing and has been measured in May 1966 to be up to 6.37 m deep (~3.59 m w.e.) (Potter, 1972). However, by the end of summer nearly all of the snowpack is melted and the little that is left is generally located in the

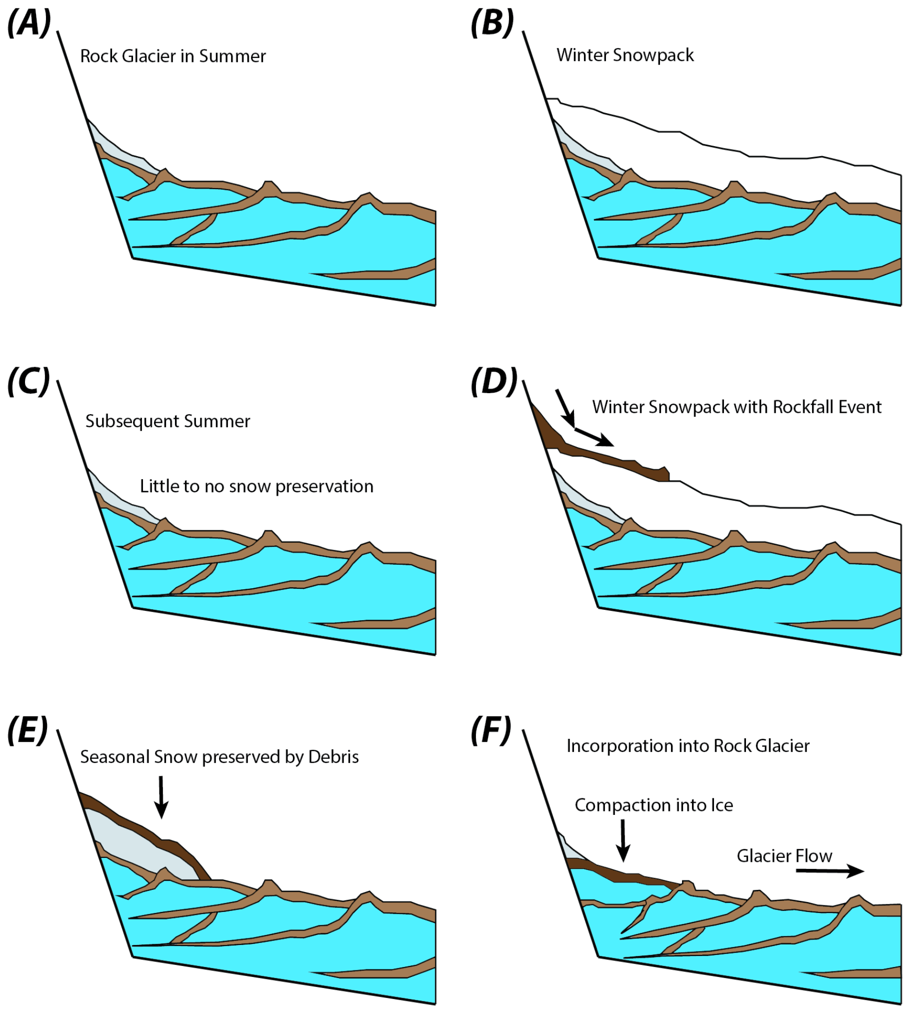

Figure 29: Cartoon illustrating the model of debris-facilitated ice accumulation. (A-C) In a typical year there is a deep winter snowpack that is mostly ablated by the end of the summer. (D-E) A large debris fall in early spring may bury a part of the snowpack and protect it against summer ablation. (F) Over time the buried snow is incorporated into the rock glacier body as a new ice unit.

southwest corner (northeast-facing slope) of the cirque. Should a large debris fall occur in the early spring however, it could bury a section of the winter snow pack and insulate it against summer melt. Potter (1972) observed reduced snowpack melt wherever the 1966 debris fall was >7-8 cm in thickness. Over time the buried snow can be incorporated into the rock glacier body as a self-contained ice unit with up to 4 m of ice. The debris thus facilitates net ice accumulation that would not otherwise occur.

There are multiple lines of evidence in support of debris-facilitated ice accumulation as the genesis of the enclosed ice units shown in Figure 24. First, they are in the eastern part of the cirque where the snowfield generally melts out completely -- i.e. there is little to no "normal" net ice accumulation (see Figure 20b: limited snowfield upslope from ice units). Related is the fact that they are located where a morphological study defined the border between the main rock glacier body and ice-cored moraines (Ackert, Jr., 1998; Figure 20). Second, the ice units are generally of a thickness comparable to that of the available snow water equivalent in the spring snowpack. Third, the ice units are located directly downslope of large debris cones fed by funneling couloirs (Figure 20b). Fourth, a large early spring debris fall has been observed in the cirque at Galena Creek Rock Glacier. Finally, the complex structure of randomly overlapping ice units and debris layers can easily be explained by a random process of debris falls.

The strong reflector observed at depths of ~28 m to ~55 m in profile #2016-3 (Figure 26) we interpret as the base of the rock glacier, with the bed dropping away from the headwalls. We also note that a possible basal reflector is imaged at depths of ~40 m depth in profiles #2016-6 and #2016-7, Figure 23), which are closer to the western edge of the rock glacier. TEM results in the cirque infer glacial thickness of 57-70 m, far deeper than the GPR can image. We conclude that the rock glacier in the cirque is typically 30-60 m thick, and at its thickest may be up to 70 m.

The resistivity values that are inferred from the TEM inversion are quite low for geologic materials. The higher resistivity of the middle layer is somewhat consistent with ice rich material, but the resistivity of the surface debris layer matches reference values only for clay or ash, and the resistivity of the basement layer matches no geologic reference value (Reynolds, 1997). For this reason we are skeptical of the exact thickness estimates yielded by the TEM analysis, but nevertheless use them as a comparison for our GPR results.

The glacier-wide radargram of the middle section provides a unique view of the large-scale structure of the rock glacier. We interpret the upper 25 m thick zone as the core of pure glacier ice discovered by Potter (1972) and cored by Clark et al. (1996). We interpret the deeper scattering zone as a buried layer of debris-rich ice. The second reflector at 35 m depth may be the bedrock contact, but the presence of continued layering and scattering beneath it leads us to interpret it as an internal contact within the rock glacier. Thus, we interpret this as evidence that the rock glacier is at least 35 m thick in this location, corroborated by the TEM data inferring 55 m thick glacier ice in the location.

Previous seismic profiling work similarly inferred an ice core 20-25 m thick, but assumed that this was the full thickness of the rock glacier; when analysis of measured velocities via glen's flow law required ice thicknesses on the order of up to 40 m these authors invoked basal sliding (Potter, 1972). We counter that the total thickness of the glacier, including the ice-poor basal layer, is at least 35 m. We also find evidence in the cirque for thicknesses on the order of 30-55 m or greater. Thus we are skeptical that basal sliding need be invoked to explain the motion of this rock glacier.

The stratigraphy of the clean ice body overlying the dirty ice layer is indicative of an episodic history of rock glacier accumulation at the area. The dirty ice layer is a more ancient and inactive rock glacier episode, the extension of which continues into the lower third of the Galena Creek Valley. It's possible that this layer is more debris-rich due to an accumulation period dominated by debris fall and debris-facilitated ice accumulation, or merely that most of the ice had ablated from the layer before it was overrun by the clean ice layer. We interpret the clean ice layer as forming via traditional glacier ice accumulation when the accumulation zone may have been more active and extensive.

CONCLUSIONS

We described through thermokarst exposure observations and ground-penetrating radar data the presence of englacial debris layers produced by large debris falls buried in Galena Creek Rock Glacier. We proposed that these debris falls can additionally facilitate ice accumulation by burying and preserving early spring snowpack which can then be incorporated into the rock glacier as an ice unit. This "debris-facilitated ice accumulation" effect is likely to be important anywhere there are large and episodic early spring debris falls paired with low or zero net background ice accumulation.

We also show that the thickness of the rock glacier in the cirque is 28-55 m and may be greater for some areas; this is a larger value than the 20-25 m thickness estimated by Potter (1972) with seismic methods. We also constrained the internal structure for the middle section of the glacier. We confirmed the presence of a glacial ice core down to a depth of 20-25 m and additionally described a stratigraphy of reflectors we interpret as alternating layers of debris-rich ice and debris near the base of the rock glacier. We speculate that these represent different episodes of rock glacier activity and are thus a potential climate record.

Chapter 6: Discussion and Conclusions

In this dissertation we presented the results of a radar survey for lobate debris aprons and a geophysical survey of Galena Creek Rock Glacier, successfully addressing many of the research questions we set out to answer.

For lobate debris aprons we mapped radar reflectors imaged in their interior for 87% of SHARAD traces with good viewing geometry. These reflectors all were found at time delays most consistent with the base of the apron; no candidate reflectors were found for the interface between surface debris and apron interior or for layering within the apron. Thus the pre-existing upper constraint on the surface debris layer thickness of ~10 m stands for all aprons in the region. Using the basal reflections we determined the bulk interior of these aprons to be composed of a material with dielectric properties of $\varepsilon' \approx 3$ and $\tan\delta \approx 0.002 < 0.005$. There is little to no regional variability in these values, which are consistent with high purity water ice. The volume of ice contained in these lobate debris aprons adds up to $0.9–1.0\times10^5$ km^3, roughly 4x the combined volume of water contained in the Great Lakes.

We addressed a number of contributors to radar losses to assess the cause of the non-detection of subsurface signals in 13% of observations and found a number of mechanisms to be at play. In a thick valley-filling apron we observed that basal radar reflections fade away at depths > 1 km; these depths are not inferred for any other aprons in the study. Our analysis of radar loss where the reflector is present show that this apron material has a similar loss tangent to those across the region and published in previous work (Holt et al., 2008; Plaut et al., 2009); thus we interpret that non-detections in this location are due to the great thickness of the apron causing the basal reflection to reach the noise floor of SHARAD. This sets an upper limit of ~1 km on the detectability of basal interfaces for thick, debris-covered glacial ice on Mars.

More broadly, we quantified surface roughness for apron surfaces across the region using a fractal analysis of topography provided by Stereo HiRISE data and found that aprons that exhibited only non-detection of subsurface signals had the roughest surfaces. We thus interpret surface roughness as the greatest control on detectability of subsurface returns at the regional scale.

The main source for surface roughness and its variability across lobate debris apron surfaces is a pitted texture often referred to as brain terrain. This morphology is caused by differential sublimation of ice from an ice-rich mantle that was deposited on apron surfaces during more recent periods of high obliquity. The patterns in sublimation pitting often align with flow lineations associated with apron viscous flow morphology. Since the rougher surfaces correspond to deeper pitting in ice-rich mantle, it is possible that they also correspond to thicker mantle deposits which accommodate the deeper pitting.

These analyses show that non-detection of subsurface radar returns can be explained without the need to invoke differing internal composition for aprons. We thus posit that, given the lack of regional variability in composition shown in Chapter 1, aprons lacking subsurface returns are composed of the same material as those exhibiting them. This is supported by the fact that all lobate debris aprons in the study region exhibit the same gross morphology: convex up topographic profiles, flow lineations, and pitted textures associated with differential ice sublimation. We acknowledge, however, that lobate debris aprons with no subsurface radar detections are not “proven” debris-covered glaciers and as such should not be given the same credibility by potential manned missions to Mars.

In our geophysical study of Galena Creek Rock Glacier we imaged a number of englacial debris layers in the cirque using ground-penetrating radar, with ground-truth from observations of a thermokarst exposure. These debris layers are on the order of 40-100 cm thick and dip up-glacier at angles of 20-35°. Some of these at the edge of the glacier form a layered network with a geometry similar to nested spoons. We interpret the englacial debris layers as formed by large debris falls buried by subsequent snow and ice accumulation. We further propose that large debris fall may induce "debris-facilitated ice accumulation," whereby debris that falls on the early spring snowpack may preserve snow that would otherwise melt in summer, allowing it to be incorporated into the rock glacier as an ice layer. We suggest the network of ice and debris layers at the edge of the cirque may be produced by the process of debris-facilitated accumulation.

Our radar observations of the englacial debris bands at Galena Creek Rock Glacier provided a valuable lesson about imaging subsurface structure that can be applied to our radar observations of martian lobate debris aprons. A number of englacial debris layers were imaged at 100 MHz but were nearly invisible at 50 MHz, highlighting the importance of the radar resolution, dependent on frequency. Conventionally, the radar resolution for a single-frequency radar is taken as one-quarter its wavelength; in the rock glacier interior this is ~40 cm for 100 MHz and ~80 cm for 50 MHz. Layers imaged at 100 MHz and not 50 MHz must be ~40-80 cm thick, consistent with the measured ~50 cm thickness of the englacial debris layer in the thermokarst exposure. SHARAD's resolution in water ice is nominally ~9 m. It would thus be difficult for SHARAD to image any englacial reflectors on the order of 40-80 cm thick unless they exhibited a sufficiently high dielectric contrast. More importantly, SHARAD is only able to image surfaces that are relatively flat, ideally with less than ~5° slope. Thin layers dipping at

20-35° similar to the englacial debris bands observed at Galena Creek Rock Glacier are unlikely to be imaged by SHARAD.

To sum up our findings as related to the research questions presented in the introduction, we find the following:

(1) There is little to no variability in the internal composition of Martian lobate debris aprons; they are all composed of relatively pure water ice. This ice must have been sourced from atmospheric accumulation during periods of high orbital obliquity.

(2) We observed no internal structure imaged by SHARAD. Thus, we find no geophysical evidence that lobate debris aprons were deposited in multiple episodes across different high obliquity periods. The simplest model is that they were deposited in a single glaciation.

(3) There is no candidate reflector for the interface between surface debris and apron interior, meaning nowhere is the surface debris layer > 10 m thick. It is possible that there is a gradual transition between surface debris and the ice-rich interior, although based on terrestrial analogs we find this to be unlikely.

(4) We observed some aprons for which SHARAD can't image their interior and show that this is due to radar losses sustained by surface roughness scattering or high apron thickness, with no need to invoke differing internal compositions.

(5) We observed the internal structure of Galena Creek Rock Glacier and mapped englacial debris layers that record debris and ice accumulation history. These debris layers are in some cases connected to flow-transverse ridges found at the surface.

(6) We propose that the debris layers are formed by large debris falls buried by ice accumulation and that in some cases these debris falls may produce debris-facilitated ice accumulation.

(7) SHARAD would be incapable of imaging the internal structure we found at Galena Creek Rock Glacier. Thus while we do not image such internal structure for lobate debris aprons that does not preclude its existence. Transverse ridge morphology on aprons may be linked to englacial debris layers similar to those observed on terrestrial rock glaciers.

In short, our findings point towards a framework in which all Martian lobate debris aprons are genetically debris-covered glaciers, with bodies composed of ~80-90% purity water ice and a surface debris layer 1-10 m thick. While we do not image any internal structure with SHARAD, that does not preclude its existence. Our analog geophysical study of Galena Creek Rock Glacier revealed an internal structure recording ice and debris accumulation history and their interaction; we suspect that some lobate debris aprons may exhibit similar internal structure. Such internal structure could record Martian climate history on the scale of 100s Ma. These results have strong implications for the global water ice budget of Mars, as well as for our current understanding of rock glacier and debris-covered glacier structure.

Bibliography

Ackert, Jr., R. P. (1998). A rock glacier/debris-covered glacier system at Galena Creek, Absaroka Mountains, Wyoming. *Geografiska Annaler: Series A, Physical Geography*, *80*(3–4), 267–276. https://doi.org/10.1111/j.0435-3676.1998.00042.x

Baker, D. M. H., & Carter, L. M. (2017). Radar Reflectors Associated With an Ice-Rich Mantle Unit in Deuteronilus Mensae, Mars (p. 1575). Presented at the Lunar and Planetary Science Conference XLVIII.

Baker, D. M. H., & Head, J. W. (2015). Extensive Middle Amazonian Mantling of Debris Aprons and Plains in Deuteronilus Mensae, Mars: Implications for the Record of Mid-Latitude Glaciation. *Icarus*. https://doi.org/10.1016/j.icarus.2015.06.036

Baker, D. M. H., Head, J. W., & Marchant, D. R. (2010). Flow patterns of lobate debris aprons and lineated valley fill north of Ismeniae Fossae, Mars: Evidence for extensive mid-latitude glaciation in the Late Amazonian. *Icarus*, *207*(1), 186–209. https://doi.org/10.1016/j.icarus.2009.11.017

Barrick, D. E., & Peake, W. H. (1968). A Review of Scattering From Surfaces With Different Roughness Scales. *Radio Science*, *3*(8), 865–868. https://doi.org/10.1002/rds196838865

Barsch. (1987). *The Problem of the Ice-Cored Rock Glacier* (Vol. 1). Boston: Allen & Unwin.

Beaty, D. W., Hays, L. E., Davis, R., Bussey, B., Abbud-Madrid, A., Boucher, D., et al. (2016). The Possible Strategic Significance of Mid-Latitude Ice Deposits to a

Potential Future Human Mission to Mars. In *Terrestrial Analogs and Future Mission Concepts* (p. 6059). Reykjavik, Iceland.

Boynton, W. V., Feldman, W. C., Squyres, S. W., Prettyman, T. H., Brückner, J., Evans, L. G., et al. (2002). Distribution of Hydrogen in the Near Surface of Mars: Evidence for Subsurface Ice Deposits. *Science*, *297*(5578), 81–85. https://doi.org/10.1126/science.1073722

Bramson, A. M., Byrne, S., Putzig, N. E., Sutton, S., Plaut, J. J., Brothers, T. C., & Holt, J. W. (2015). Widespread Excess Ice in Arcadia Planitia, Mars. *Geophysical Research Letters*, *42*(16), 6566–6574. https://doi.org/10.1002/2015GL064844

Brown, W. H. (1925). A Probable Fossil Glacier. *The Journal of Geology*, *33*(4), 464–466.

Broxton, M. J., & Edwards, L. J. (2008). The Ames Stereo Pipeline: Automated 3D Surface Reconstuction from Orbital Imagery (p. 2419). Presented at the 39th Lunar and Planetary Science Conference. Retrieved from http://www.lpi.usra.edu/meetings/lpsc2008/pdf/2419.pdf

Bucki, A. K., Echelmeyer, K. A., & MacINNES, S. (2004). The thickness and internal structure of Fireweed rock glacier, Alaska, USA, as determined by geophysical methods. *Journal of Glaciology*, *50*(168), 67–75.

Campbell, B. A. (2002). *Radar Remote Sensing of Planetary Surfaces*. Cambridge University Press.

Campbell, B. A., & Morgan, G. A. (2018). Fine-Scale Layering of Mars Polar Deposits and Signatures of Ice Content in Nonpolar Material From Multiband SHARAD

Data Processing. *Geophysical Research Letters*, *45*(4), 1759–1766. https://doi.org/10.1002/2017GL075844

Capps, S. R. (1910). Rock glaciers in Alaska. *The Journal of Geology*, 359–375.

Carter, L. M., Campbell, B. A., Holt, J. W., Phillips, R. J., Putzig, N. E., Mattei, S., et al. (2009). Dielectric properties of lava flows west of Ascraeus Mons, Mars. *Geophysical Research Letters*, *36*(23), L23204. https://doi.org/10.1029/2009GL041234

Choudhary, P., Holt, J. W., & Kempf, S. D. (2016). Surface Clutter and Echo Location Analysis for the Interpretation of SHARAD Data From Mars. *IEEE Geoscience and Remote Sensing Letters*, *13*(9), 1285–1289. https://doi.org/10.1109/LGRS.2016.2581799

Chuang, F. C., & Crown, D. A. (2009). Geologic Map of MTM 35337, 40337, and 45337 Quadrangles, Deuteronilus Mensae Region of Mars. Geologic, United States Geological Survey, Department of the Interior.

Clark, D. H., Steig, E. J., Potter, N., Updike, A., Fitzpatrick, J., & Clark, G. M. (1996). Old ice in rock glaciers may provide long-term climate records. *Eos, Transactions American Geophysical Union*, *77*(23), 217–222. https://doi.org/10.1029/96EO00149

Clark, D. H., Steig, E. J., Potter, Jr., N., & Gillespie, A. R. (1998). Genetic variability of rock glaciers. *Geografiska Annaler: Series A, Physical Geography*, *80*(3–4), 175–182. https://doi.org/10.1111/j.0435-3676.1998.00035.x

Colaprete, A., & Jakosky, B. M. (1998). Ice flow and rock glaciers on Mars. *Journal of Geophysical Research: Planets*, *103*(E3), 5897–5909. https://doi.org/10.1029/97JE03371

Degenhardt, J. J. (2003). Subsurface investigation of a rock glacier using ground-penetrating radar: Implications for locating stored water on Mars. *Journal of Geophysical Research*, *108*(E4). https://doi.org/10.1029/2002JE001888

Evans, S. (1965). Dielectric Properties of Ice and Snow–a Review. *Journal of Glaciology*, *5*(42), 773–792. https://doi.org/10.3189/S0022143000018840

Evatt, G. W., Abrahams, I. D., Heil, M., Mayer, C., Kingslake, J., Mitchell, S. L., et al. (2015). Glacial melt under a porous debris layer. *Journal of Glaciology*, *61*(229), 825–836. https://doi.org/10.3189/2015JoG14J235

Fassett, C. I., Levy, J. S., Dickson, J. L., & Head, J. W. (2014). An extended period of episodic northern mid-latitude glaciation on Mars during the Middle to Late Amazonian: Implications for long-term obliquity history. *Geology*, *42*(9), 763–766. https://doi.org/10.1130/G35798.1

Fastook, J. L., & Head, J. W. (2008). Dichotomy Boundary Glaciation Models: Implications for Timing and Glacial Processes. *AGU Fall Meeting Abstracts*, *1*, 1354.

Feldman, W. C., Prettyman, T. H., Maurice, S., Plaut, J. J., Bish, D. L., Vaniman, D. T., et al. (2004). Global distribution of near-surface hydrogen on Mars. *Journal of Geophysical Research: Planets*, *109*(E9), n/a–n/a. https://doi.org/10.1029/2003JE002160

Florentine, C., Skidmore, M., Speece, M., Link, C., & Shaw, C. A. (2014). Geophysical analysis of transverse ridges and internal structure at Lone Peak Rock Glacier, Big Sky, Montana, USA. *Journal of Glaciology*, *60*(221), 453–462. https://doi.org/10.3189/2014JoG13J160

Forget, F., Haberle, R. M., Montmessin, F., Levrard, B., & Head, J. W. (2006). Formation of Glaciers on Mars by Atmospheric Precipitation at High Obliquity. *Science*, *311*(5759), 368–371. https://doi.org/10.1126/science.1120335

Gallegos, Z. E., & Newsom, H. E. (2015). A Human Exploration Zone in the Protonilus Mensae Region of Mars (p. 1053). Presented at the First Landing Site/Exploration Zone Workshop for Human Missions to the Surface of Mars, The Woodlands, Texas.

Goldsby, D. L., & Kohlstedt, D. L. (2001). Superplastic deformation of ice: Experimental observations. *Journal of Geophysical Research: Solid Earth*, *106*(B6), 11017–11030. https://doi.org/10.1029/2000JB900336

Gough, S. R. (1972). A Low Temperature Dielectric Cell and the Permittivity of Hexagonal Ice to 2 K. *Canadian Journal of Chemistry*, *50*(18), 3046–3051. https://doi.org/10.1139/v72-483

Grima, C., Kofman, W., Mouginot, J., Phillips, R. J., Hérique, A., Biccari, D., et al. (2009). North polar deposits of Mars: Extreme purity of the water ice. *Geophysical Research Letters*, *36*(3), L03203. https://doi.org/10.1029/2008GL036326

Grima, C., Kofman, W., Herique, A., Orosei, R., & Seu, R. (2012). Quantitative analysis of Mars surface radar reflectivity at 20MHz. *Icarus*, *220*(1), 84–99.

Haeberli, W., Hallet, B., Arenson, L., Elconin, R., Humlum, O., Kääb, A., et al. (2006). Permafrost creep and rock glacier dynamics. *Permafrost and Periglacial Processes*, *17*(3), 189–214. https://doi.org/10.1002/ppp.561

Head, James W., Nahm, A. L., Marchant, D. R., & Neukum, G. (2006). Modification of the dichotomy boundary on Mars by Amazonian mid-latitude regional glaciation. *Geophysical Research Letters*, *33*(8), n/a–n/a. https://doi.org/10.1029/2005GL024360

Head, James W., Marchant, D. R., Dickson, J. L., Kress, A. M., & Baker, D. M. (2010). Northern mid-latitude glaciation in the Late Amazonian period of Mars: Criteria for the recognition of debris-covered glacier and valley glacier landsystem deposits. *Earth and Planetary Science Letters*, *294*(3–4), 306–320. https://doi.org/10.1016/j.epsl.2009.06.041

Head, James W., Dickson, J. L., Mustard, J. F., Milliken, R. E., Scott, D., Johnson, B., et al. (2015). Mars Human Science Exploration and Resource Utilization: The Dichotomy Boundary Deuteronilus Mensae Exploration Zone (p. 1033). Presented at the First Landing Site/Exploration Zone Workshop for Human Missions to the Surface of Mars, The Woodlands, Texas.

Head, J.W., Marchant, D. R., Agnew, M. C., Fassett, C. I., & Kreslavsky, M. A. (2006). Extensive valley glacier deposits in the northern mid-latitudes of Mars: Evidence for Late Amazonian obliquity-driven climate change. *Earth and Planetary Science Letters*, *241*(3–4), 663–671. https://doi.org/10.1016/j.epsl.2005.11.016

Heggy, E., Clifford, S. M., Younsi, A., Miane, J. L., Carley, R., & Morris, R. V. (2006). On the Dielectric Properties of Dust and Ice-Dust Mixtures: Experimental Characterization of the Martian Polar Layered Deposits Analog Materials (p. 8105). Presented at the Fourth Mars Polar Science Conference.

Heggy, E., Clifford, S. M., Cosmidis, J., Humeau, A., Boisson, J., & Morris, R. V. (2008). Geoelectrical Model of the Martian North Polar Layered Deposits (p. 2471). Presented at the Lunar and Planetary Science XXXIX.

Helbert, J. (2005). Limits on the burial depth of glacial ice deposits on the flanks of Hecates Tholus, Mars. *Geophysical Research Letters*, *32*(17). https://doi.org/10.1029/2005GL023712

Holt, J. W., Safaeinili, A., Plaut, J. J., Head, J. W., Phillips, R. J., Seu, R., et al. (2008). Radar Sounding Evidence for Buried Glaciers in the Southern Mid-Latitudes of Mars. *Science*, *322*(5905), 1235–1238. https://doi.org/10.1126/science.1164246

Johari, G. P. (1976). The dielectric properties of H2O and D2O ice Ih at MHz frequencies. *The Journal of Chemical Physics*, *64*(10), 3998–4005. https://doi.org/10.1063/1.432033

Karlsson, N. B., Schmidt, L. S., & Hvidberg, C. S. (2015). Volume of Martian mid-latitude glaciers from radar observations and ice-flow modelling: Martian mid-latitude glaciers. *Geophysical Research Letters*, n/a-n/a. https://doi.org/10.1002/2015GL063219

Kress, A. M., & Head, J. W. (2008). Ring-mold craters in lineated valley fill and lobate debris aprons on Mars: Evidence for subsurface glacial ice. *Geophysical Research Letters*, *35*(23), n/a–n/a. https://doi.org/10.1029/2008GL035501

Lalich, D. E., & Holt, J. W. (2016). New Martian climate constraints from radar reflectivity within the north polar layered deposits. *Geophysical Research Letters*, 2016GL071323. https://doi.org/10.1002/2016GL071323

Laskar, J., Correia, A. C. M., Gastineau, M., Joutel, F., Levrard, B., & Robutel, P. (2004). Long term evolution and chaotic diffusion of the insolation quantities of Mars. *Icarus*, *170*(2), 343–364. https://doi.org/10.1016/j.icarus.2004.04.005

Laskar, Jacques, Levrard, B., & Mustard, J. F. (2002). Orbital forcing of the martian polar layered deposits. *Nature*, *419*(6905), 375–377. https://doi.org/10.1038/nature01066

Levy, J., Head, J. W., & Marchant, D. R. (2010). Concentric crater fill in the northern mid-latitudes of Mars: Formation processes and relationships to similar landforms of glacial origin. *Icarus*, *209*(2), 390–404. https://doi.org/10.1016/j.icarus.2010.03.036

Levy, J. S., & Holt, J. W. (2015). A Human Landing Site on the Hellas Rim: Ancient Craters, Flowing Water, and Abundant Ice (p. 1037). Presented at the First Landing Site/Exploration Zone Workshop for Human Missions to the Surface of Mars, The Woodlands, Texas.

Levy, J. S., Head, J. W., & Marchant, D. R. (2009). Concentric crater fill in Utopia Planitia: History and interaction between glacial "brain terrain" and periglacial mantle processes. *Icarus*, *202*(2), 462–476. https://doi.org/10.1016/j.icarus.2009.02.018

Levy, J. S., Fassett, C. I., Head, J. W., Schwartz, C., & Watters, J. L. (2014). Sequestered glacial ice contribution to the global Martian water budget: Geometric constraints on the volume of remnant, midlatitude debris-covered glaciers. *Journal of Geophysical Research: Planets*, *119*(10), 2014JE004685. https://doi.org/10.1002/2014JE004685

Levy, J. S., Fassett, C. I., & Head, J. W. (2016). Enhanced erosion rates on Mars during Amazonian glaciation. *Icarus*, *264*, 213–219. https://doi.org/10.1016/j.icarus.2015.09.037

Li, H., Robinson, M. S., & Jurdy, D. M. (2005). Origin of martian northern hemisphere mid-latitude lobate debris aprons. *Icarus*, *176*(2), 382–394. https://doi.org/10.1016/j.icarus.2005.02.011

Lucchitta, B. K. (1978). Geologic Map of the Ismenius Lacus Quadrangle of Mars. I-1065 (MC-5): United States Geological Survey, Department of the Interior.

Lucchitta, Baerbel K. (1984). Ice and debris in the Fretted Terrain, Mars. *Journal of Geophysical Research: Solid Earth*, *89*(S02), B409–B418. https://doi.org/10.1029/JB089iS02p0B409

Mackay, S. L., & Marchant, D. R. (2017). Obliquity-paced climate change recorded in Antarctic debris-covered glaciers. *Nature Communications*, *8*, 14194. https://doi.org/10.1038/ncomms14194

Mackay, S. L., Marchant, D. R., Lamp, J. L., & Head, J. W. (2014). Cold-based debris-covered glaciers: Evaluating their potential as climate archives through studies of ground-penetrating radar and surface morphology: Cold-based debris-covered glaciers. *Journal of Geophysical Research: Earth Surface*, *119*(11), 2505–2540. https://doi.org/10.1002/2014JF003178

Madeleine, J.-B., Forget, F., Head, J. W., Levrard, B., Montmessin, F., & Millour, E. (2009). Amazonian northern mid-latitude glaciation on Mars: A proposed climate scenario. *Icarus*, *203*(2), 390–405. https://doi.org/10.1016/j.icarus.2009.04.037

Mahaney, W. C., Miyamoto, H., Dohm, J. M., Baker, V. R., Cabrol, N. A., Grin, E. A., & Berman, D. C. (2007). Rock glaciers on Mars: Earth-based clues to Mars' recent paleoclimatic history. *Planetary and Space Science*, *55*(1–2), 181–192. https://doi.org/10.1016/j.pss.2006.04.016

Mangold, N. (2003). Geomorphic analysis of lobate debris aprons on Mars at Mars Orbiter Camera scale: Evidence for ice sublimation initiated by fractures. *Journal of Geophysical Research: Planets*, *108*(E4), n/a–n/a. https://doi.org/10.1029/2002JE001885

Mangold, N., Dehouck, E., Poulet, F., Ansan, V., & Le Mouélic, S. (2015). Ismenius Cavus: Ancient Lake Deposits and Clay Minerals Surrounded by Amazonian Glaciers (p. 1027). Presented at the First Landing Site/Exploration Zone Workshop for Human Missions to the Surface of Mars, The Woodlands, Texas.

McEwen, A. S., Eliason, E. M., Bergstrom, J. W., Bridges, N. T., Hansen, C. J., Delamere, W. A., et al. (2007). Mars Reconnaissance Orbiter's High Resolution

Imaging Science Experiment (HiRISE). *Journal of Geophysical Research*, *112*(E5). https://doi.org/10.1029/2005JE002605

McGill, G. E. (2002). Geologic Map Transecting the Highland/Lowland Boundary Zone, Arabia Terra, Mars: Quandrangles 3033, 35332, 40332, and 45332. Geologic, Atlas of Mars: United States Geological Survey, Department of the Interior.

Mellon, M. T., & Jakosky, B. M. (1993). Geographic variations in the thermal and diffusive stability of ground ice on Mars. *Journal of Geophysical Research: Planets*, *98*(E2), 3345–3364. https://doi.org/10.1029/92JE02355

Mellon, M. T., & Jakosky, B. M. (1995). The distribution and behavior of Martian ground ice during past and present epochs. *Journal of Geophysical Research: Planets*, *100*(E6), 11781–11799. https://doi.org/10.1029/95JE01027

Mellon, M. T., Feldman, W. C., & Prettyman, T. H. (2004). The presence and stability of ground ice in the southern hemisphere of Mars. *Icarus*, *169*(2), 324–340. https://doi.org/10.1016/j.icarus.2003.10.022

Monnier, S., & Kinnard, C. (2015). Internal Structure and Composition of a Rock Glacier in the Dry Andes, Inferred from Ground-penetrating Radar Data and its Artefacts. *Permafrost and Periglacial Processes*, n/a-n/a. https://doi.org/10.1002/ppp.1846

Moore, P. L. (2014). Deformation of debris-ice mixtures. *Reviews of Geophysics*, *52*(3), 2014RG000453. https://doi.org/10.1002/2014RG000453

Moratto, Z. M., Broxton, M. J., Beyer, R. A., Lundy, M., & Husmann, K. (2010). Ames Stereo Pipeline, NASA's Open Source Automated Stereogrammetry Software (p.

2364). Presented at the 41st Lunar and Planetary Science Conference. Retrieved from http://www.lpi.usra.edu/meetings/lpsc2010/pdf/2364.pdf

Nye, J. F. (1957). The Distribution of Stress and Velocity in Glaciers and Ice-Sheets. *Proceedings of the Royal Society of London. Series A, Mathematical and Physical Sciences*, *239*(1216), 113–133.

Ogilvy, J. A. (1991). *Theory of Wave Scattering From Random Rough Surfaces,*. Taylor & Francis.

Östrem, G. (1959). Ice Melting under a Thin Layer of Moraine, and the Existence of Ice Cores in Moraine Ridges. *Geografiska Annaler*, *41*(4), 228–230.

Parsons, R. A., Nimmo, F., & Miyamoto, H. (2011). Constraints on martian lobate debris apron evolution and rheology from numerical modeling of ice flow. *Icarus*, *214*(1), 246–257. https://doi.org/10.1016/j.icarus.2011.04.014

Petersen, E. I., Holt, J. W., Levy, J. S., & Goudge, T. A. (2017). New Constraints on Surface Debris Layer Composition for Martian Mid-Latitude Glaiers From SHARAD and HiRISE (p. 2767). Presented at the 48th Lunar and Planetary Science Conference. Retrieved from https://www.hou.usra.edu/meetings/lpsc2017/pdf/2767.pdf

Plaut, J. J. (2015). A Resource-rich, Scientifically Compelling Exploration Zone for Human Missions at Deuteronilus Mensae, Mars (p. 1044). Presented at the First Landing Site/Exploration Zone Workshop for Human Missions to the Surface of Mars.

Plaut, J. J., Picardi, G., Safaeinili, A., Ivanov, A. B., Milkovich, S. M., Cicchetti, A., et al. (2007). Subsurface radar sounding of the south polar layered deposits of Mars. *Science (New York, N.Y.)*, *316*(5821), 92–95. https://doi.org/10.1126/science.1139672

Plaut, J. J., Safaeinili, A., Holt, J. W., Phillips, R. J., Head, J. W., Seu, R., et al. (2009). Radar evidence for ice in lobate debris aprons in the mid-northern latitudes of Mars. *Geophysical Research Letters*, *36*(2), n/a–n/a. https://doi.org/10.1029/2008GL036379

Potter Jr, N., Steig, E. J., Clark, D. H., Speece, M. A., Clark, G. t, & Updike, A. B. (1998). Galena Creek rock glacier revisited—New observations on an old controversy. *Geografiska Annaler: Series A, Physical Geography*, *80*(3–4), 251–265.

Potter, N. (1972). Ice-Cored Rock Glacier, Galena Creek, Northern Absaroka Mountains, Wyoming. *Geological Society of America Bulletin*, *83*(10), 3025–3058. https://doi.org/10.1130/0016-7606(1972)83[3025:IRGGCN]2.0.CO;2

Rangecroft, S., Harrison, S., & Anderson, K. (2015). Rock Glaciers as Water Stores in the Bolivian Andes: An Assessment of Their Hydrological Importance. *Arctic, Antarctic, and Alpine Research*, *47*(1), 89–98. https://doi.org/10.1657/AAAR0014-029

Reynolds, J. M. (1997). *An Introduction to Applied and Environmental Geophysics*. Wiley.

Schorghofer, N. (2008). Temperature response of Mars to Milankovitch cycles. *Geophysical Research Letters*, *35*(18). https://doi.org/10.1029/2008GL034954

Seu, R., Phillips, R. J., Biccari, D., Orosei, R., Masdea, A., Picardi, G., et al. (2007). SHARAD sounding radar on the Mars Reconnaissance Orbiter. *Journal of Geophysical Research: Planets*, *112*(E5), n/a–n/a. https://doi.org/10.1029/2006JE002745

Sharp, R. P. (1973). Mars: Fretted and chaotic terrains. *Journal of Geophysical Research*, *78*(20), 4073–4083. https://doi.org/10.1029/JB078i020p04073

Shean, D. E., Alexandrov, O., Moratto, Z. M., Smith, B. E., Joughin, I. R., Porter, C., & Morin, P. (2016). An automated, open-source pipeline for mass production of digital elevation models (DEMs) from very-high-resolution commercial stereo satellite imagery. *ISPRS Journal of Photogrammetry and Remote Sensing*, *116*, 101–117. https://doi.org/10.1016/j.isprsjprs.2016.03.012

Shepard, M. K., & Campbell, B. A. (1999). Radar Scattering from a Self-Affine Fractal Surface: Near-Nadir Regime. *Icarus*, *141*(1), 156–171. https://doi.org/10.1006/icar.1999.6141

Sihvola, A. H. (1999). *Electromagnetic Mixing Formulas and Applications*. IET.

Smedes, H. W., & Prostka, H. J. (1972). *Stratigraphic framework of the Absaroka Volcanic Supergroup in the Yellowstone National Park region* (USGS Numbered Series No. 729– C). Retrieved from http://pubs.er.usgs.gov/publication/pp729C

Smith, D. E., Zuber, M. T., Frey, H. V., Garvin, J. B., Head, J. W., Muhleman, D. O., et al. (2001). Mars Orbiter Laser Altimeter: Experiment summary after the first year of global mapping of Mars. *Journal of Geophysical Research: Planets*, *106*(E10), 23689–23722. https://doi.org/10.1029/2000JE001364

Squyres, S. W. (1978). Martian fretted terrain: Flow of erosional debris. *Icarus*, *34*(3), 600–613. https://doi.org/10.1016/0019-1035(78)90048-9

Squyres, S. W. (1979). The distribution of lobate debris aprons and similar flows on Mars. *Journal of Geophysical Research: Solid Earth*, *84*(B14), 8087–8096. https://doi.org/10.1029/JB084iB14p08087

Steig, E. J., Fitzpatrick, J. J., Potter Jr, N., & Clark, D. H. (1998). The geochemical record in rock glaciers. *Geografiska Annaler: Series A, Physical Geography*, *80*(3–4), 277–286.

Steig, E. J., Clark, D. H., Potter, Jr., N., & Gillespie, A. R. (1998). The geomorphic and climatic significance of rock glaciers. *Geografiska Annaler: Series A, Physical Geography*, *80*(3–4), 173–174. https://doi.org/10.1111/j.0435-3676.1998.00034.x

Stuurman, C. M., Osinski, G. R., Holt, J. W., Levy, J. S., Brothers, T. C., Kerrigan, M., & Campbell, B. A. (2016). SHARAD detection and characterization of subsurface water ice deposits in Utopia Planitia, Mars. *Geophysical Research Letters*, 2016GL070138. https://doi.org/10.1002/2016GL070138

Swinzow, G. K. (1962). Investigation of shear zones in the ice sheet margin, Thule area, Greenland. *Journal of Glaciology*, *04*(032), 215–229.

Tanaka, K. L., Skinner, J. A., Jr., Dohm, J. M., Irwin, R. P., III, Kolb, E. J., Fortezzo, C. M., et al. (2014). Geologic Map of Mars: U.S. Geologic Survey Scientific Investigations Map 3292. Retrieved from https://dx.doi.org/10.3133/sim3292

Wahrhaftig, C., & Cox, A. (1959). ROCK GLACIERS IN THE ALASKA RANGE. *Geological Society of America Bulletin*, *70*(4), 383. https://doi.org/10.1130/0016-7606(1959)70[383:RGITAR]2.0.CO;2

Watters, T. R., Campbell, B., Carter, L., Leuschen, C. J., Plaut, J. J., Picardi, G., et al. (2007). Radar Sounding of the Medusae Fossae Formation Mars: Equatorial Ice or Dry, Low-Density Deposits? *Science*, *318*(5853), 1125–1128. https://doi.org/10.1126/science.1148112